# Particle Astrophysics with Cosmic Neutrinos

By

Ali Kheirandish

A dissertation submitted in partial fulfillment of
the requirements for the degree of

Doctor of Philosophy
(Physics)

at the
UNIVERSITY OF WISCONSIN–MADISON
2017

Date of final oral examination: December 19, 2016

The dissertation is approved by the following members of the Final Oral Committee:

Francis Halzen, Professor, Physics

Albrecht Karle, Professor, Physics

Justin Vandenbroucke, Assistant Professor, Physics

Vernon Barger, Professor, Physics

Paolo Desiati, Scientist (Wisconsin IceCube Particle Astrophysics Center)

**DISCARD THIS PAGE**

# TABLE OF CONTENTS

Page

Page

**DISCARD THIS PAGE**

# LIST OF TABLES

**DISCARD THIS PAGE**

# LIST OF FIGURES

Figure Page

Figure Page

Figure Page

Figure Page

# Chapter 1

# Introduction

In 1933, when Pauli suggested the neutrino as the particle responsible for the missing energy in the beta decay puzzle, he was afraid that he had introduced a particle that could not be detected. However, development of the weak interaction theory showed the neutrino to be a weakly interacting particle which led to discovery of the neutrino in 1956 [1].

Soon after the discovery, the idea emerged that neutrinos represented ideal astronomical messengers. They reach us directly from the edges of the Universe. In contrast to cosmic rays, which are deflected by magnetic fields, neutrinos point back to their cosmic accelerators. Their feeble interaction with matter also makes them immune to absorption. Therefore, high-energy neutrinos may reach us unscathed from cosmic distances-from the neighborhood of black holes and from nuclear furnaces where cosmic rays are born.

Although their weak interaction makes neutrinos the perfect astronomical messengers, it also makes cosmic neutrinos very difficult to detect. Immense particle detectors are required to collect cosmic neutrinos in statistically significant numbers [2]. It was clear in the 1970s that cubic-kilometer-size detectors were required in order to detect cosmic neutrinos produced in the interaction of cosmic rays with Cosmic Microwave Background (CMB) photons [3]. Subsequent estimates for observing potential cosmic accelerators such as Galactic supernova remnants and gamma-ray bursts unfortunately pointed to the same exigent requirement [4, 5, 6].

The spectacular success of neutrino astronomy in observing the Sun and the supernova in the Large Magellanic Cloud in 1987 showed its vitality. Both observations had tremendous importance; the former showed that neutrinos have mass, opening the first crack in the Standard Model of particle physics, and the latter confirmed the basic nuclear physics of the death of stars.

The thirty-year-long effort to build a large volume detector to detect neutrinos of extraterrestrial origin led to construction of the Antarctic Muon And Neutrino Detector Array (AMANDA), which paved the way for construction of the IceCube Neutrino Observatory. After the first year of full deployment, IceCube succeeded in discovering the flux of cosmic neutrinos, rejecting the atmospheric background explanation of the observed high-energy neutrinos. This discovery marked a new era of neutrino astrophysics and challenged our understanding of the Universe.

The most surprising property of the observed cosmic neutrinos was their large flux. An immediate inference made about this large flux observed by IceCube, which is predominantly extragalactic in origin, is that the total energy density of neutrinos in the high-energy Universe is similar to that of gamma rays. The matching energy densities of the extragalactic gamma ray flux detected by *Fermi* and the high-energy neutrino flux measured by IceCube suggests that they originated in common sources. Rather than detecting some exotic sources, it looks more likely that IceCube observes the same universe as astronomers do. The finding implies that a large fraction of the energy in the non-thermal universe originates in hadronic processes, indicating a larger level than previously thought.

The focus of this dissertation is on identifying the sources of high-energy cosmic neutrinos observed in IceCube. Moreover, with the lack of confirmation to date of any source (type of sources) as the dominant contributor to the observed neutrino flux, we have studied prospects for observing different sources in IceCube by considering both transient and steady sources in the sky. Finally, we introduce new techniques to study the strength of neutrino dark matter interactions with the properties of high-energy cosmic neutrinos.

# Chapter 2

# Neutrino astronomy

## 2.1 The birth of neutrino astronomy

In the early years of the 20th century, Victor Hess's discovery of Cosmic Rays [7] brought a new messenger to study the sky. With the development of science and improvement of techniques, our knowledge of the sky had extremely broadened by the observation in X-ray, radio, and gamma ray telescopes. Moreover, thanks to the large air shower arrays cosmic rays have been observed in a very wide range of energies. These, alongside with the success of cosmology in describing the early stages of the Universe, gave us a novel understanding of high-energy sky, and non-thermal component of the Universe. However, despite all of that, cosmic rays and gamma rays fail to describe the high-energy Universe due to their intrinsic nature.

High-energy gamma rays and cosmic rays are produced in or at the vicinity of some the most energetic objects in the cosmos and carry information about their origin and mechanism of acceleration. However, gamma rays are either absorbed in the galactic matter or are attenuated by their interaction with the cosmic background radiation. The pair production interaction length of PeV gamma rays in the CMB is of the order of 10 kpc, which makes it impossible to observe this emission over extragalactic distances. Fig. 2.1 shows the interaction length of gamma rays for pair production and inverse-Compton of photons with the CMB and extra background light (EBL) [9]. For extragalactic sources such as Centaurus A at 4 Mpc, gamma rays emissions are suppressed below 100 TeV. The diffuse flux of gamma rays from cosmic sources is only visible below 10 TeV due to EBL absorption.

On the other hand, cosmic ray deflection in the magnetic fields makes it impossible to trace them back to their sources. Cosmic ray spectrum spans over more than 10 orders of magnitude. The energies of interest are shown in Fig. 2.2. At these energies, the cosmic ray spectrum follows a sequence of three power laws. The first two are separated by "knee", the second and third by the "ankle". It is known that cosmic rays

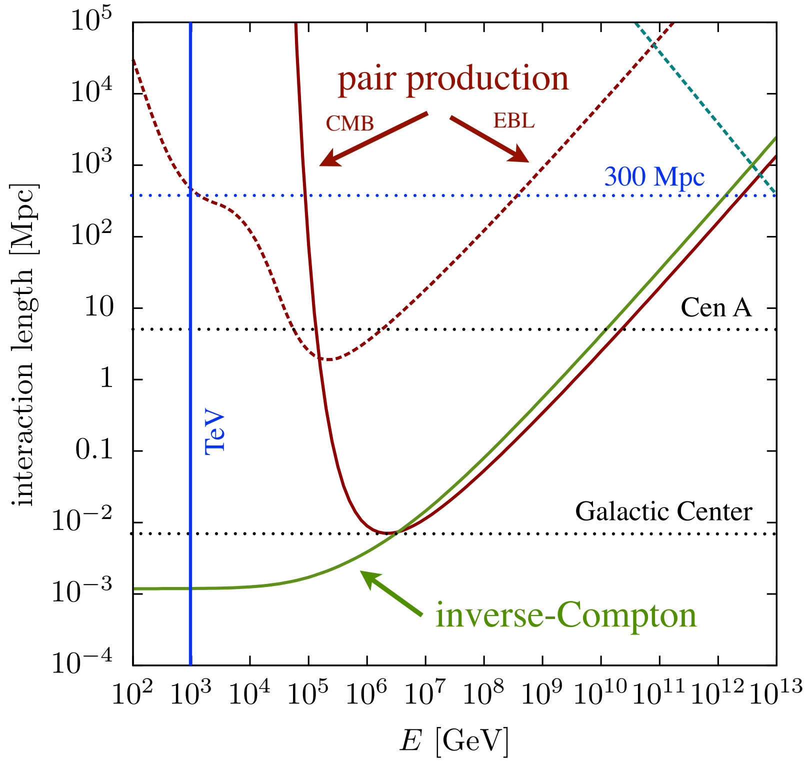


**Figure 2.1:** The interaction length of pair production and inverse-Compton (green) scattering of gamma rays with the CMB (solid red) and EBL (dashed red) . Galactic Center and the close-by radio galaxy Cen A distances are indicated [8].

above the knee could not originate in the galaxy since their gyro-radii would exceed the size of the galaxy. However, where the transition between galactic and extragalactic cosmic rays happen is still unanswered. Moreover, the observation of cosmic rays at $10^{20}$ eV demonstrated the existence of extreme accelerators outside the Galaxy. These questions origin together with other questions about the composition of the ultra high-energy cosmic rays, and the mechanism of acceleration could not be answered by sole observation of cosmic-rays. Finally, cosmic rays originating from distances further than 75 Mpc would not reach the Earth due to their attenuation in CMB (This effect will be discussed in more details). Observable distance for photons and protons are shown in Fig. 2.3.

The idea that neutrinos represent ideal cosmic messengers emerged few years after their discovery. Having essentially no mass and no electric charge, the neutrino is similar to photons, except for one important attribute: its interaction with matter is extremely feeble. Therefore, high-energy neutrinos my reach us

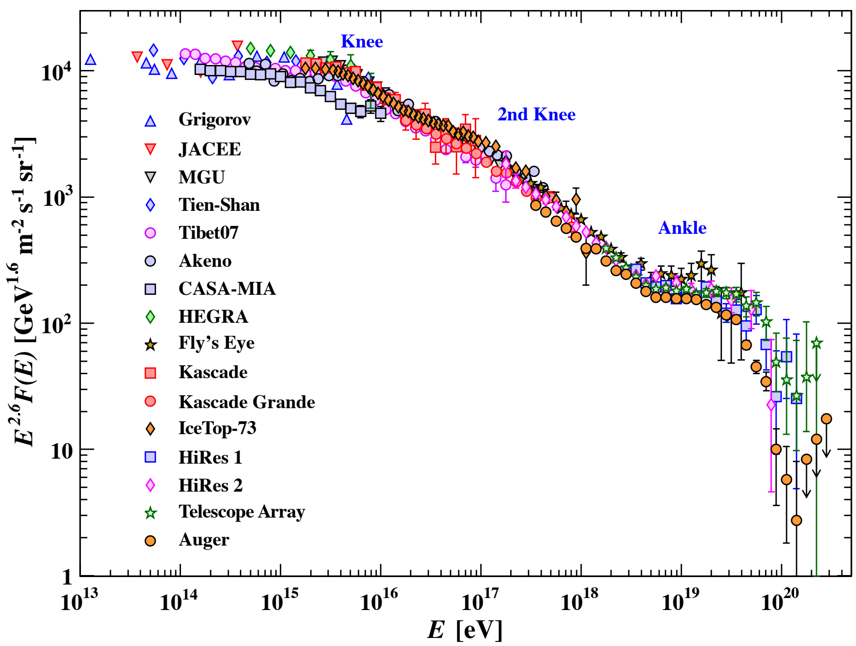


**Figure 2.2:** Cosmic ray spectrum and its features (Data compiled by Particle Data Group [10])

unscathed from the edges of Universe. They neither get absorbed by the matter, nor deflected by magnetic field. Therefore, they point back to their sources, and emerge as the ideal astronomical messenger.

Astronomical neutrinos will reveal the information required to understand the nature of ultra high-energy accelerators in the sky. Together with the gamma rays and cosmic rays, high-energy neutrinos build the 3 components of the multi-messenger paradigm.

Fig. 2.4 illustrates the neutrino energy spectrum covering an enormous range, from microwave energies ($10^{-12}$ eV) to $10^{20}$ eV [14]. The figure is a mixture of observations and theoretical predictions. At the lowest energies, the neutrino sky is dominated by neutrinos produced in the Big Bang, i.e. Cosmic Neutrino Background (C$\nu$B). At MeV energy, neutrinos are produced by supernova explosions; the flux from the SN1987 is shown. At yet higher energies, the figure displays the measured atmospheric neutrino flux, up to energies of 100 TeV by the AMANDA experiment [13]. Atmospheric neutrinos are the results of high-energy cosmic ray interactions in the atmosphere, and are a main player in searching for cosmic neutrinos, because they are the dominant background. The flux of atmospheric neutrinos falls dramatically with increasing energy; events above 100 TeV are rare, leaving a clear field of view for extraterrestrial sources.

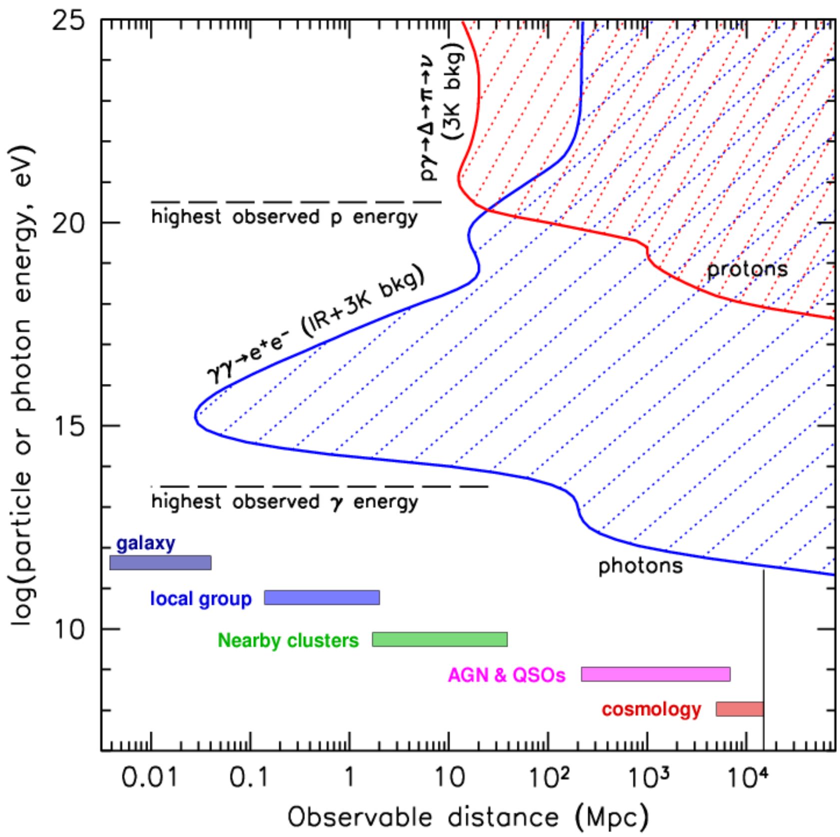


**Figure 2.3:** Observable distance for photons and protons, from P. Gorham [11]

At energies above 100 TeV, neutrinos from Active Galactic Nuclei (AGN) and Gamma Ray Burst would dominate the spectrum. The highest energy neutrinos in Fig. 2.4 are the decay products of pions produced by the interactions of cosmic rays with microwave photons [15]. Above a threshold of $\sim 4 \times 10^{19}$ eV, cosmic rays interact with the CMB introducing an absorption feature in the cosmic ray flux, the Greisen-Zatsepin-Kuzmin (GZK) cutoff. As a consequence, the mean free path of extragalactic cosmic rays propagating in the microwave background is limited to roughly 75 Mpc, and, therefore, the secondary neutrinos are the only probe of the still enigmatic sources at longer distances.

Although neutrinos weak interaction made them suitable for astrophysics, it also makes them very difficult to detect. In order to collect cosmic neutrinos in statistically significant numbers, immense particle detectors are required to enhance the chance of particle's interaction. Estimates for the potential neutrino production

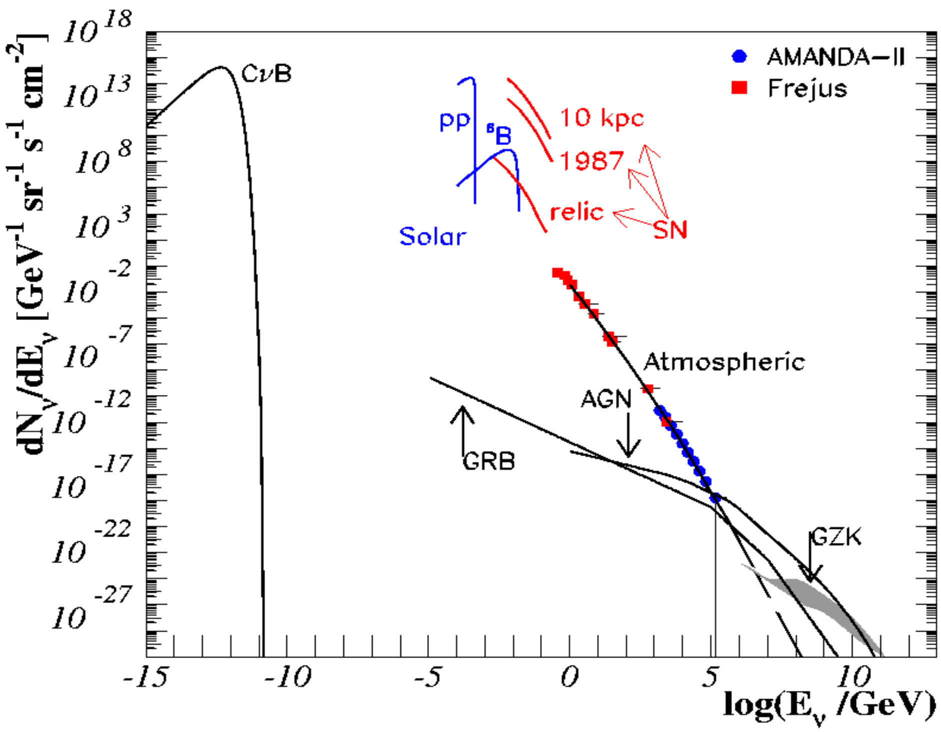


**Figure 2.4:** The cosmic-neutrino spectrum. Sources are the Big Bang (C$\nu$B), the Sun, supernovae (SN), atmospheric neutrinos, active galactic nuclei (AGN) galaxies, and GZK neutrinos. The data points are from detectors at the Frejus underground laboratory [12] (red) and from AMANDA [13] (blue).

at Galactic SN remnants and GRBs, and the flux of GZK neutrinos made it clear that a cubic-kilometer detector was required to observe cosmic neutrinos [2, 3, 4].

Early efforts to build such detector concentrated on transforming large volume of natural water into Cherenekov detector to detect the light produced when neutrinos interact with nuclei in or near the detector [16]. Deep Under Water Muon and Neutrino Detector (DUMAND) in Hawaii was the first attempt [17]. Although DUMAND did not succeed, it paved the way for later efforts to build the smaller detector in Lake Baikal [18] and the neutrino telescope in the Mediterranean [19, 20, 21]. Operation of Antarctic Muon and Neutrino Detector Array (AMANDA) represented the proof of concept for kilometer-scale neutrino observatory, IceCube [22].

One of the primary motivations for construction of a kilometer-scale neutrino detector was to detect neutrinos associated with the sources of high-energy cosmic rays. As mentioned earlier, cosmic accelerators produce particles with energies in excess of 100 EeV; we still do not know where and how the acceleration happens [23], see Fig. 2.2. The bulk of the cosmic rays are Galactic in origin. Any association with our

Galaxy presumably disappears at EeV energy when the gyro-radius of a proton in the Galactic magnetic field exceeds its size. The cosmic rays spectrum exhibits a rich structure above an energy of $\sim 0.1$EeV, but where exactly the transition to extragalactic cosmic rays occurs is a matter of debate.

Cosmic ray accelerators must meet two challenges: first, the highest-energy particles in the beam must reach energies beyond $10^3$ TeV ($10^8$ TeV) for Galactic (extragalactic) sources, and secondly, their luminosities must accommodate the observed flux. Acceleration of protons (or nuclei) to TeV energy and above requires massive bulk flows of relativistic charged particles. Such environments are proposed to exist at supernova remnants to produce galactic cosmic rays, and in GRBs and AGNs for extragalactic cosmic rays.

Neutrinos associated with cosmic rays will unravel where and how these particles are produced and accelerated. Neutrinos will be produced at some level in association with the cosmic ray beam. cosmic rays accelerated in regions of high magnetic fields near black holes or neutron stars inevitably interact with matter or radiation surrounding them. Thus, cosmic ray accelerators are also "beam dumps" producing neutrino beams. The method is what is used for the production of neutrino beams at accelerator laboratories: the beam is dumped in a dense target where it produces pions and kaons that decay into neutrinos.

Cosmic rays accelerated in supernova shocks interact with gas in the Galactic disk, producing equal numbers of pions of all three charges that decay into pionic photons and neutrinos. A larger source of secondaries is likely to be gas near the sources, for example cosmic rays interacting with high-density molecular clouds that are ubiquitous in the star-forming regions where supernovae are more likely to explode. For extragalactic sources, the neutrino producing target may be electromagnetic, for instance photons radiated by the accretion disk of an AGN, or synchrotron photons that coexist with protons in the expanding fireball producing a GRB.

The number of neutrinos, and inevitably, gamma rays that are produced in association with cosmic ray beam depends on the nature of the beam dump. Generically, a cosmic ray source should also be a beam dump: cosmic rays accelerated in regions of high magnetic fields interact with surrounding radiation field such as UV photons. These photo-hadronic interactions result in production of charged and neutral pions by the processes

$$p + \gamma \to \Delta^+ \to \pi^0 + p \quad \text{and} \quad p + \gamma \to \Delta^+ \to \pi^+ + n. \tag{2.1}$$

In a hadronic beam dump, CR mostly interact with the matter field such as the hydrogen in the galactic disk, producing equal numbers of pions of all three charges in hadronic collisions

$$p + p \to n[\pi^0 + \pi^+ + \pi^-] + X, \tag{2.2}$$

where $n$ is the pion multiplicity.

While both gamma-ray and neutrino fluxes can be calculated knowing the density of the accelerated protons and the density of the target material, their relative flux is independent of the details of the production mechanism. The spectral production rates $dN/dEdt$ of neutrinos and gamma rays (at the source) are related by

$$\frac{1}{3}\sum_{\nu_i} E_{\nu_i}^2 \frac{\mathrm{d}N_{\nu_i}}{\mathrm{d}E_{\nu_i}\,\mathrm{d}t} \simeq \frac{K_\pi}{4} E_\gamma^2 \frac{\mathrm{d}N_\gamma}{\mathrm{d}E_\gamma \mathrm{d}t} \tag{2.3}$$

Here, $N$ and $E$ denote the number and energy of neutrinos and gamma rays and $i$ stands for the neutrino flavor. Note that this relation is solid and depends only on the charged-to-neutral secondary pion ratio, with $K_\pi = 1(2)$ for $\gamma(pp)$ neutrino-producing interactions. In deriving the relative number of neutrinos and gamma rays, one must be aware of the fact that the neutrino flux represents the sum of the neutrinos and antineutrinos, which cannot be separated by current experiments.

The production rate of gamma rays described by Eq. 2.3 is not necessarily the emission rate observed. For instance, in cosmic accelerators that efficiently produce neutrinos via $p\gamma$ interactions, the target photon field can also efficiently reduce the pionic gamma rays via pair production. This is a calorimetric process that will, however, conserve the total energy of hadronic gamma rays. The production of photons in association with cosmic neutrinos is inevitable. The relation is however calorimetric; unlike neutrinos, photons reach Earth after propagation in the cosmic microwave and infrared photon backgrounds to reach our telescopes with TeV energy, or below. Also, one must be aware of the fact that inverse-Compton scattering and synchrotron emission by accelerated electrons in magnetic fields in the source have the potential to produce gamma rays; not every high-energy gamma ray is pionic.

## 2.2 IceCube neutrino observatory

IceCube is the first kilometer-scale neutrino detector that is sensitive enough to observe neutrinos of cosmic origin, at a level of high statistical significance. IceCube consists of 80 strings, each instrumented

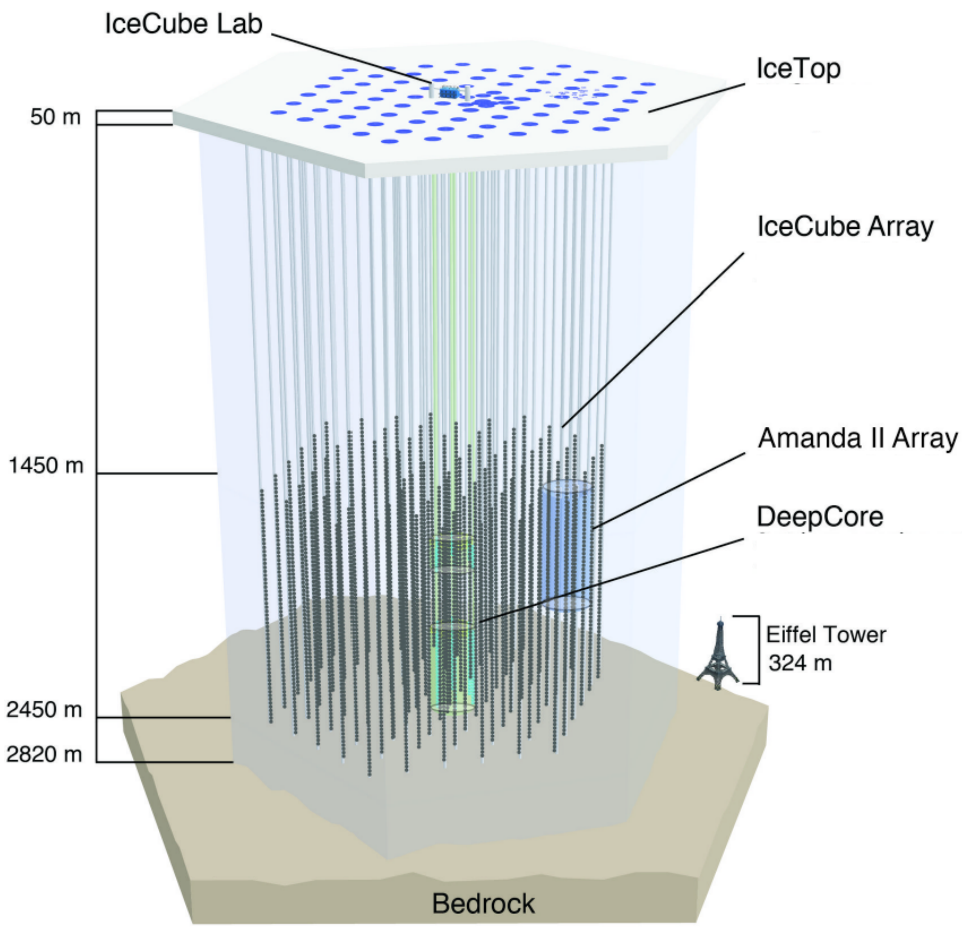


**Figure 2.5:** Schematic of IceCube detector, illustrating the strings (vertical lines) and the detector modules (small spheres) at depths between 1500 and 2500 m. DeepCore subdetector and AMANDA-II are marked as cylinders. The blue circle on the ice surface show the IceTop tanks.

with 60 10-inch photomultipliers spaced by 17 m over a total length of 1 kilometer. The deepest module is located at a depth of 2.450 km so that the instrument is shielded from the large background of cosmic rays at the surface by approximately 1.5 km of ice. Strings are arranged at apexes of equilateral triangles that are 125 m on a side. The instrumented detector volume is a cubic kilometer of dark, highly transparent and sterile Antarctic ice. Radioactive background is dominated by the instrumentation deployed into this natural ice, see Fig. 2.5.

Each optical sensor consists of a glass sphere containing the photomultiplier and the electronics board that digitizes the signals locally using an on-board computer. The digitized signals are given a global time stamp with residuals accurate to less than 3ns and are subsequently transmitted to the surface. Processors at the surface continuously collect these time-stamped signals from the optical modules, each of which functions independently. The digital messages are sent to a string processor and a global event trigger. They are subsequently sorted into the Cherenkov patterns emitted by secondary muon tracks, or electron and tau showers, that reveal the direction of the parent neutrino [24].

IceCube detects neutrinos by observing the Cherenkov radiation from the charged particles produced by neutrino interactions inside or in the vicinity of the detector. Charge current interactions produce a lepton that carries, on average, 50% of the neutrino energy for E $\leq$ 10 GeV, to 80% at high energies. The remainder of the energy is released in the hadronic shower produced by the target nucleus Both the secondary lepton and the hadronic shower produce Cherenkov radiation. In neutral current interactions, the neutrino transfers a fraction of its energy to a nuclear target, producing a hadronic shower. IceCube can differentiate neutrino flavors on the basis of their topology in the detector, as illustrated in Fig. 2.6. There are two basic topologies: tracks from charge current interaction of $\nu_\mu$ and cascades from charged current $\nu_e$, $\nu_\tau$ , and the neutral current interactions from all flavors. Cascades are produced by the radiation of particle showers, whose dimensions are in the tens of meters, i.e., an approximate point source of light with respect to the dimensions of the detector.

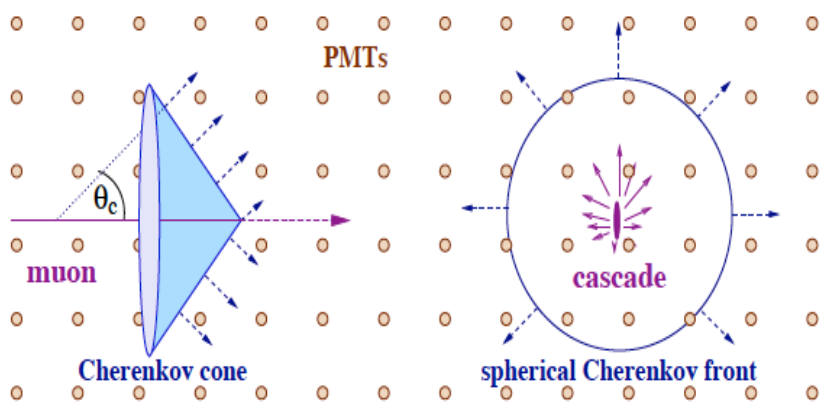


**Figure 2.6:** Cherenkov light patterns produced by muons (left) and by showers initiated by electron and tau neutrinos and by neutral current interactions (right) . The patterns are referred to as tracks and cascades (showers), respectively.

The different topologies each have advantages and disadvantages. For $\nu_\mu$ interactions, the long lever arm of muon tracks, up to tens of kilometers at very high energies, allows the muon direction (and the neutrino direction) to be determined accurately with an angular resolution measured online that is better than 0.4°.

Superior angular resolution can be reached for selected events. Sensitivity to point source studies is therefore better as well. The disadvantages are a large background, of atmospheric neutrinos below 100 TeV and CR muons at all energies, and the indirect determination of the neutrino energy that must be inferred from sampling the energy loss of the muon when it transits the detector. The signal probability for an individual event is shown in Fig. 2.7.

Observation of $\nu_e$ and $\nu_\tau$ flavors also represents significant advantages. They are detected for both Northern and Southern Hemispheres. (This is also true for $\nu_\mu$ with energy in excess of 1 PeV, where the background from the steeply falling atmospheric spectrum becomes negligible.) At TeV energies and above, the background of atmospheric $\nu_e$ is lower by over an order of magnitude, and there are essentially no atmospheric $\nu_\tau$ produced. At higher energies, long-lived pions, the source of atmospheric $\nu_e$, no longer decay, and relatively rare K-decays become the dominant source of background $\nu_e$. Furthermore, because the neutrino events are totally, or at least partially, contained inside the instrumented detector volume, the neutrino energy is determined by total-absorption calorimetry. One can establish the cosmic origin of a single event by demonstrating that the energy cannot be reached by muons and neutrinos of atmospheric origin. Finally, $\nu_\tau$ are not absorbed by the Earth [26]: $\nu_\tau$ interacting in the Earth produce secondary $\nu_\tau$ of lower energy, either directly in a neutral current interaction or via the decay of a secondary tau lepton produced in

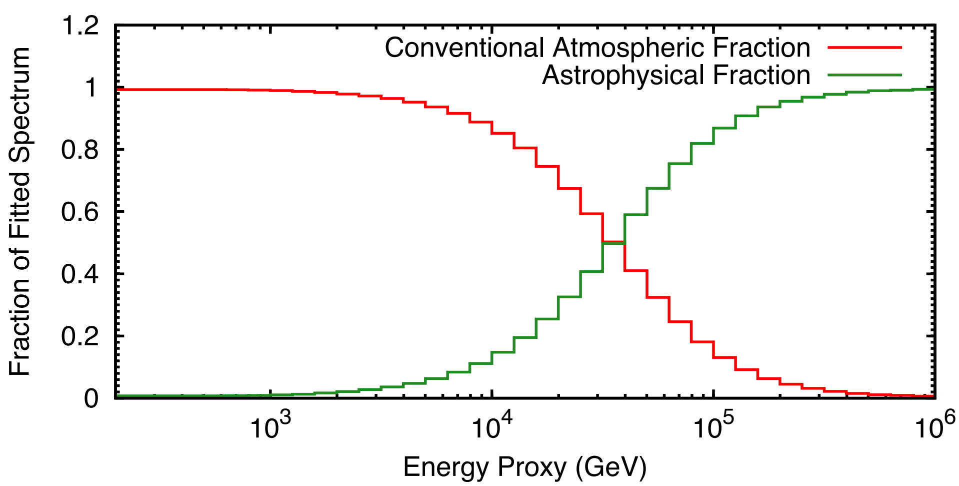


**Figure 2.7:** The fraction of the total flux as a function of the event energy proxy for atmospheric and astrophysical components [25]. The astrophysical purity of the sample is obtained at energies above 100 TeV.

a charged-current interaction. High-energy $\nu_\tau$ will thus cascade down to energies of hundred of TeV where the Earth becomes transparent. In other words, they are detected with a reduced energy but not absorbed.

Although cascades are nearly point-like and, in practice, spatially isotropic, the pattern of arrival times of the photons at individual optical modules reveals the direction of the secondary leptons with $3^\circ$. While a fraction of cascade events can be reconstructed accurately to within a degree the precision is inferior to that reached for $\nu_\mu$ events and typically not better than $10^\circ$ using the present techniques

## 2.3 Discovery of cosmic neutrinos

After a year of completion, IceCube successfully observed a flux of cosmic neutrinos rejecting the atmospheric explanation of observed neutrinos. Primarily, there were two methods used to identify cosmic neutrinos. Neutrino searches have historically focused on the observation of muon neutrinos that interact primarily outside the detector, producing kilometer-long muon tracks that pass through the detection volume. Although this allows observation of neutrinos that interact outside the detector, it is then necessary to use the Earth as a filter in order to remove the huge background of cosmic-ray muons. This method limits the neutrino view to a single flavor and half the sky. An alternative method exclusively identifies neutrinos interacting inside the detector. The latter was the first search to see the evidence of cosmic neutrinos in IceCube in 2013 [27]. Today, both methods have observed neutrinos with astrophysical origin by a significance larger than $5\sigma$ [28, 29, 30]. The main results of both analysis is discussed in the following.

### 2.3.1 High-energy starting events

As mentioned earlier, the first evidence for cosmic neutrinos was found in an analysis that exclusively considered neutrinos interacting inside the detector. This method, divides the instrumented volume of ice into an outer veto shield and a roughly 500 megaton inner fiducial volume. The advantage of focusing on neutrinos interacting inside the instrumented volume of ice is that the detector then functions as a total absorption calorimeter, measuring energy with a 10-15 % resolution. Also, neutrinos from all directions in the sky can be identified, including both muon tracks, produced in muon-neutrino charged-current interactions, and secondary showers, produced by electron and tau neutrinos as well as in neutral-current interactions of neutrinos of all flavors.

Using the veto technique to find high-energy Starting Events (HESE) in IC79 and first year of IC86 revealed 28 events passing the veto cuts, representing an excess over atmospheric neutrino background, and

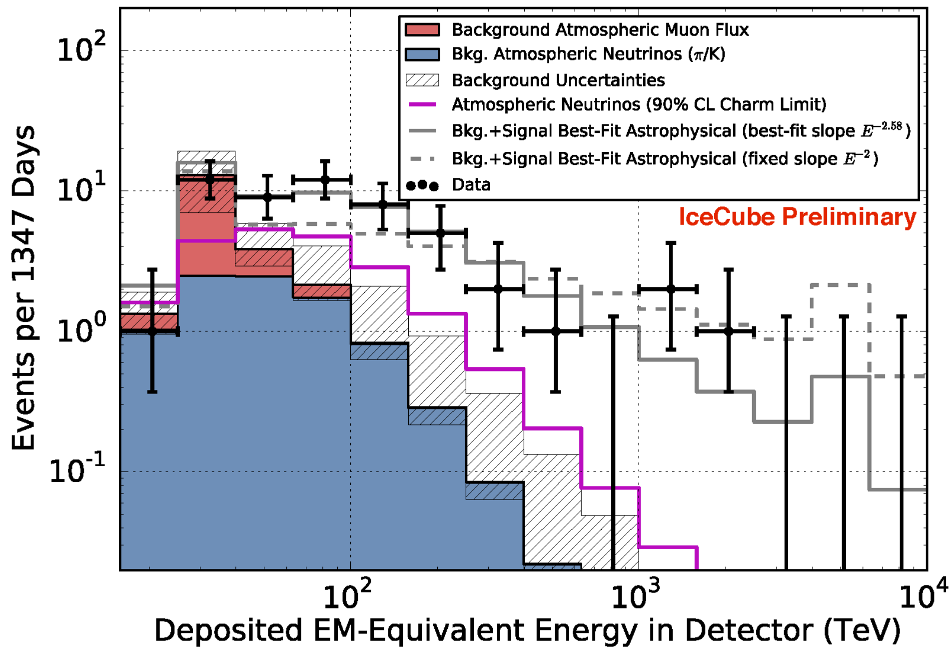


**Figure 2.8:** Deposited energies, by neutrinos interacting inside IceCube, observed in four years of data. The hashed region shows uncertainties on the sum of all backgrounds. The atmospheric muon flux (red) and its uncertainty is computed from simulation to overcome statistical limitations in our background measurement and scaled to match the total measured background rate. The atmospheric neutrino flux is derived from previous measurements of both the pion and Kaon, and charm components of the atmospheric spectrum. Two power-law fits to the spectrum are also illustrated (gray).

rejecting the background hypothesis [27]. Inclusion of second and third year of IC86 [28, 29] enhanced the observed number of events up to 54 events with energies above 30 TeV, see Fig. 2.8. This sample consists of 14 tracks and 40 cascades. The spectral analysis of these events resulted in a best fit power law flux of

$$E^2\phi(E) = 2.2 \pm 0.7 \times 10^{-8}(E/100\,\mathrm{TeV})^{-0.58}\,\mathrm{GeV}^{-1}\mathrm{cm}^{-2}\mathrm{s}^{-1}\mathrm{sr}^{-1} \tag{2.4}$$

### 2.3.2 Through going muons

Analysis of the same years of data used in HESE analysis for through going tracks from northern sky resulted in observation of cosmic neutrinos with an evidence of $3.4\sigma$ [31]. $5\sigma$ significance in this analysis was achieved in the analysis of further years. Using 6 years of data from IC59 to forth year of IC86, the sample of

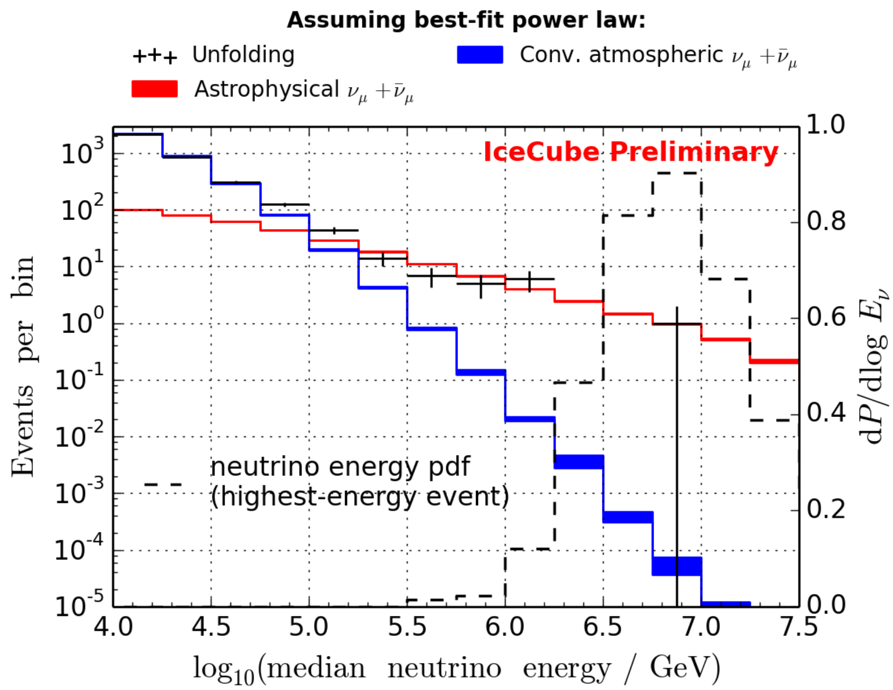


**Figure 2.9:** Spectrum of secondary muons initiated by muon neutrinos that have traversed the Earth, i.e., with zenith angle less than 5° above the horizon, as a function of the energy they deposit inside the detector. For each reconstructed muon energy, the median neutrino energy is calculated assuming the best-fit spectrum. The colored bands (blue/red) show the expectation for the conventional and astrophysical contributions. The black crosses show the measured data. Additionally, the neutrino energy probability density function for the highest energy event assuming the best-fit spectrum is shown (dashed line)

through going muons yields $5.6\sigma$ significance at energies above 100 TeV [30]. The event energy distribution and flux information is shown in Fig 2.9 and 2.10, respectively.

The data are well described by an unbroken power law flux with a normalization at 100 TeV neutrino energy of $0.90 \times 10^{-18}\mathrm{GeV}^{-1}\mathrm{cm}^{-2}\mathrm{s}^{-1}\mathrm{sr}^{-1}$ and a spectral index of $\gamma = 2.13$. The neutrino energy contributing to the flux measured from through going muons covers the range of 200 TeV to $\sim 9$ PeV.

The measured flux shows a harder spectral behavior in comparison with the starting event analysis, that presented the soft spectral index of $-2.58$. This tension is discussed more in section 2.4.

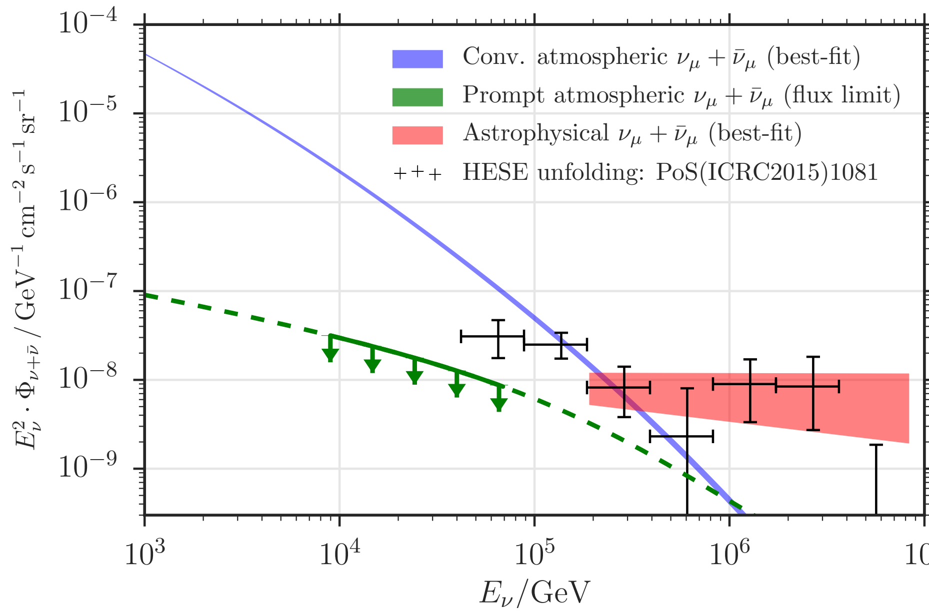


**Figure 2.10:** Best-fit neutrino spectra for unbroken power-law model, The line widths (blue, red) represent the one sigma error on the measured spectrum where the green line represents the upper limit on the prompt model [32]. The horizontal width of the red band denotes the energy range of neutrino energies which contribute 90% to the total likelihood ratio between the best-fit and the conventional atmospheric-only hypothesis. The black crosses show the unfolded spectrum from HESE-4 sample [29].

## 2.4 Understanding cosmic neutrinos

In summary, both methods for selecting cosmic neutrinos harvest about 10 events per year, more if one tolerates a modest background. The observed flux is consistent with the isotropic arrival direction and equal contribution of all flavors of neutrinos [33]. Although no correlation has been yet found to the galactic plane, a subdominant galactic contribution cannot be excluded. Interestingly, measurement of the flux with events with energies above 1 TeV [34] suggests that at the cosmic neutrino flux dominates the atmospheric background above an energy that may be as low as 30 TeV, with an energy spectrum that cannot be described as a single power as was the case for the muon neutrino flux through the Earth for energies exceeding 220 TeV. This observation is reinforced by the fact that fitting the cosmic neutrino flux in different ranges of energy yields values for the power-law exponent that are statistically inconsistent. This inconsistency is shown in Fig. 2.11. The conclusion to be drawn is that the astrophysical flux measured by IceCube is not featureless.

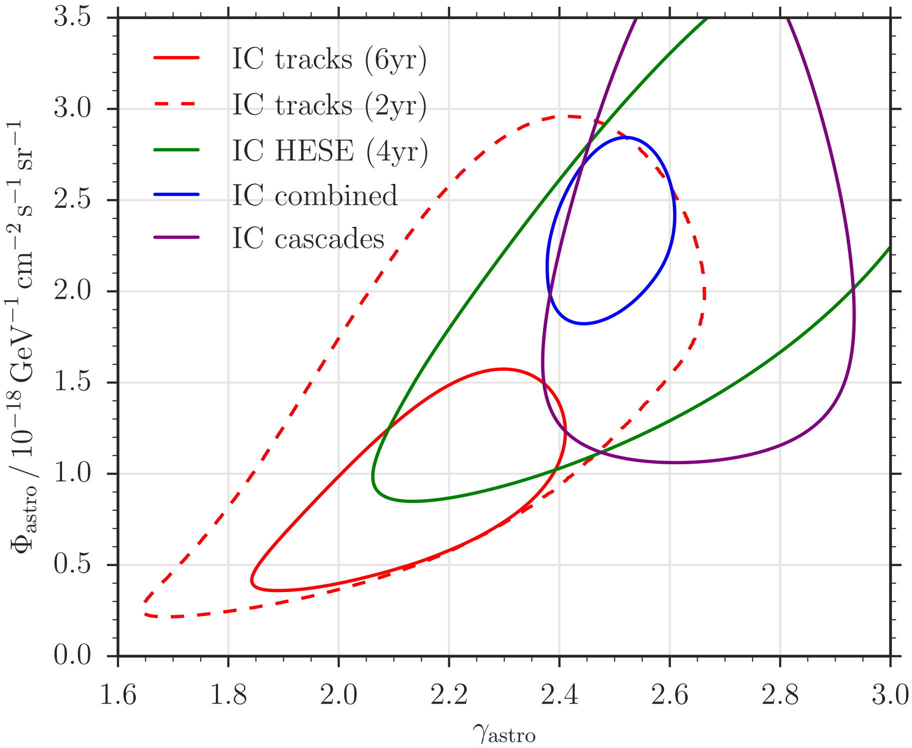


**Figure 2.11:** Results of different IceCube analyses measuring the astrophysical flux parameters. The contour lines show the 90% confidence level [29].

Neutrinos are produced in association with cosmic rays beams. It is straight forward to apply the multi-messenger connection discussed in Sec. 2.1 to the flux observed by IceCube. Fig. 2.12 shows the gamma ray flux accompanying the observed neutrino flux for the case of *pp* interaction at the cosmic beam dump. The black and red lines show the neutrino and gamma ray spectra after accounting for the cascading of the PeV photons in cosmic radiation backgrounds between source and observation. The black line shows an $E^{-2.15}$ neutrino spectrum with an exponential cutoff around PeV. This scenario actually matches the extragalactic isotropic diffuse gamma-ray background measured by *Fermi* [35]. This indicates that the contribution of gamma rays accompanying IceCube neutrinos to *Fermi's* extragalactic flux is significant, suggesting a common origin of some of the sources at some level.

The arrival direction of high-energy neutrinos and its uncertainty is shown in Fig. 2.13. No statistically significance clustering of the events has been found, and the arrival directions are compatible with the isotropic distribution [33]. Also searches for association with the Galactic plane has not shown any correlation.

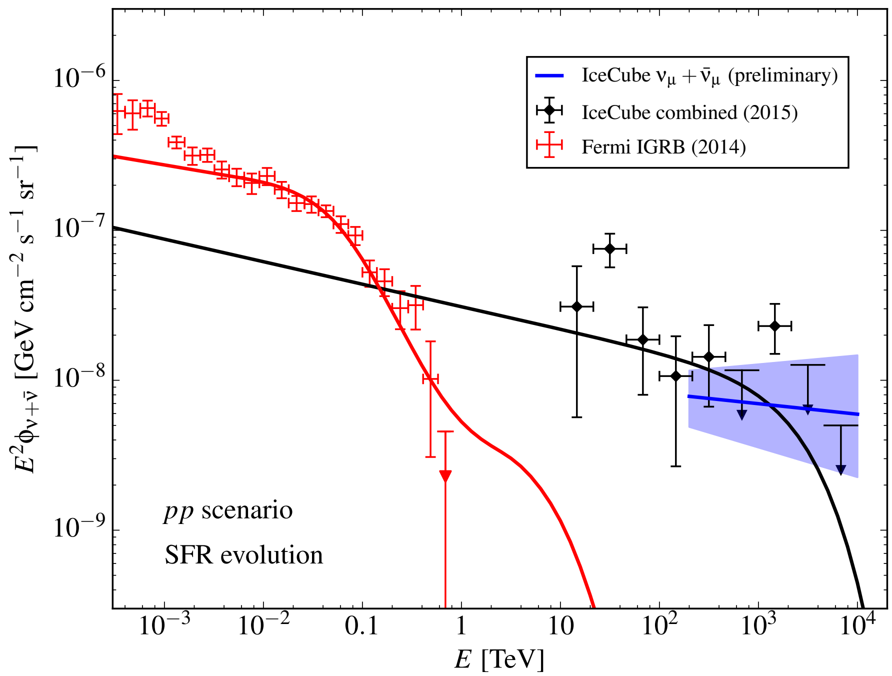


**Figure 2.12:** The figure shows that the astrophysical neutrino flux (black line) observed by IceCube matches the corresponding cascaded gamma ray flux (red line) observed by *Fermi*. It is assumed that the decay products of neutral and charged pions from *pp* interactions are responsible for the non-thermal emission in the Universe [36]. The black data points are combined IceCube results, including the three-year HESE analysis and a subsequent analysis lowering the energy threshold for events starting in the detector even further [34]. Also shown is the best fit to the flux of high-energy muon neutrinos penetrating the Earth [29]

The more delicate search for the point sources in IceCube has been performed by using through going tracks. These searches has not yet found any evidence for a hotspot in the sky. For the latest results on the point source studies in IceCube, see [37].

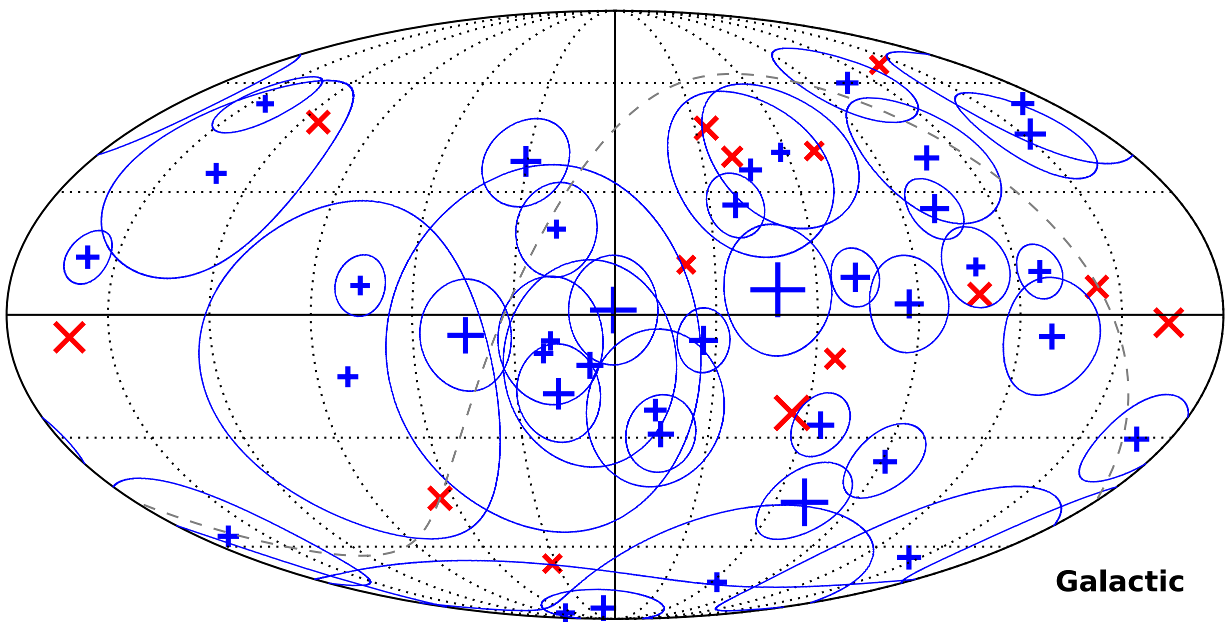


**Figure 2.13:** Arrival direction of neutrinos in four years HESE [33] in Galactic coordinates. The red x's are muon tracks, and the blue crosses represent cascades. The blue circle around cascades shows median angular uncertainty of the events. The dashed line (gray) is the horizon for IceCube at the geographic south pole. The size of the x's and crosses is scaled by events energies.

# Chapter 3

## Searching for the sources of cosmic neutrinos

In this chapter, we investigate the correlation of high-energy cosmic neutrinos with catalogs of gamma rays and cosmic rays. The catalogs here are chosen based on the expected association of neutrinos with cosmic ray accelerators and simultaneous production of gamma rays and neutrinos. The strategy of searching for neutrino point sources is to look for spatial clustering in the arrival direction of neutrinos; to find any excess over the expected isotropic distribution of background. The technique used by IceCube to search for point sources is described in [38, 39]. In this method, an un-binned maximum likelihood is used to look for spatial clustering of the events. Significances are estimated by repeating each hypothesis test on data sets randomized in right ascension, which provides robust p-values that are largely independent of detector systematic uncertainties.

So far, IceCube searches for sources of astrophysical neutrinos have not led to any evidence of a hot spot in the sky. For recent results of IceCube point source searches, see [37]. These searches use through going tracks from both hemispheres because of their finer angular resolution and higher statistics compared to starting events sample.

Here, we use the events from four years of HESE to search for any possible correlation with cosmic rays and gamma rays. For this purpose, instead of looking for the possible association of individual sources in the catalog with high-energy neutrinos we do a stacking search of the events to find the level of any possible correlation.

## 3.1 Point source study

Stacking multiple sources in neutrino astronomy has been an effective way to enhance discovery potential and further constrain astrophysical models [40, 41]. The stacking likelihood is defined as

$$\mathcal{L}(n_s) = \prod_{i}^{events} \Big( \sum_{j}^{M} \frac{n_s}{N} \frac{w_j}{M} \mathcal{S}_i^j + \frac{N - n_s}{N} \mathcal{B}_i \Big) \tag{3.1}$$

where $\mathcal{B}_i$ represents the isotropic background probability distribution function (PDF), and the signal PDF, $\mathcal{S}_i$, describes the directional uncertainty map for each event. $N$ is the total number of events in the data sample and $n_s$ is the number of signal events, which is a free parameter. M is the number of sources in the catalog and $w_j$ is the normalized theoretical weight for each source. This weight could correspond to properties such as flux and distance.

In general, the likelihood could also be a function of the spectral index, which we do not consider here for the sake of simplicity.

The signal PDF $\mathcal{S}_i$ incorporates directional information about each individual event and it depends on the angular uncertainty of the event, $\sigma_i$, and the angular difference between the reconstructed direction of the event and the source:

$$\mathcal{S}_i^j = \mathcal{S}_i^j(|x_i - x_j|, \sigma_i), \tag{3.2}$$

This function is modeled as a two-dimensional gaussian

$$S_i(|x_i - x_j|, \sigma_i) = \frac{1}{2\pi\sigma_i^2} \exp\Big( - \frac{|x_i - x_j|^2}{2\sigma_i^2} \Big) \tag{3.3}$$

Since we are using HESE neutrinos in this study, we consider the background PDF, $\mathcal{B}_i$ to be uniform through the whole sky i.e., $\mathcal{B}_i = 1/4\pi$, as is done for the point source studies for HESE sample, see [28].

After maximizing and determining the best fit number of signal events $\hat{n}_s$, the test statistic (TS) is defined as the log likelihood ratio between the null and alternative hypothesis. In this case, the null hypothesis is that all events are generated from the isotropic background distribution, that is $n_s = 0$. The alternative hypothesis is the neutrinos originate at set of considered sources with strength $n_s$. The TS is calculated via:

$$TS = 2 \log \big[ \frac{\mathcal{L}(\hat{n}_s)}{\mathcal{L}(n_s = 0)} \big] \tag{3.4}$$

The significance of an observation is determined by comparing the TS to the TS distribution from data sets randomized in right ascension. The TS distribution for randomized data sets represents the probability a given observation could occur by random chance with the given data. For large sample sizes, this distribution approximately follows a chi-squared distribution, where the number of degrees of freedom corresponds to the difference in the number of free parameters between the null hypothesis and the alternate hypothesis.

In the following we test the correlation between HESE neutrinos and ultra high energy cosmic rays from Pierre Auger Observatory and Telescope Array, the catalog of TeV gamma ray emitters, and the Vernon Cetty-Vernon catalog of Active Galactic Nuclei.

## 3.2 Correlation study with ultra high energy cosmic rays

Finding the sources of cosmic neutrinos was one of the primary reasons to build IceCube. Here, we used the arrival direction of ultra high energy cosmic rays observed by Pierre Auger Observatory and Telescope Array to investigate the correlation between them and observed high-energy neutrinos in four years of HESE. In this search we study the correlation of each data sets separately.

### 3.2.1 Ultra high energy neutrinos from Pierre Auger Observatory

Here, we use the arrival direction of the cosmic rays with energies higher than 55 EeV reported by Auger collaboration [42]. This data set includes 69 ultra high energy cosmic rays observed in five years of detector operation. Arrival direction of Auger cosmic rays and HESE neutrinos are shown in Fig. 3.1.

Using the likelihood and test statistics described 3.1, we find the p-value for the correlation of Auger ultra high-energy cosmic rays and IceCube HESE neutrinos to be 0.13. The distribution of test statistics is shown in Fig. 3.2. The p-value indicates the correlation is at a level of less than $2\sigma$ and the test shows compatibility of the sample with the null hypothesis: isotropic background distribution of the events.

### 3.2.2 Ultra high energy neutrinos from Telescope Array

Telescope Array collaboration reported observation of ultra high-energy cosmic rays with energies greater than 57 EeV [43]. These data set is somehow complementary to the data observed in Auger, since it covers the northern sky. The sample contains 72 events from five years of observation. It is worth mentioning that

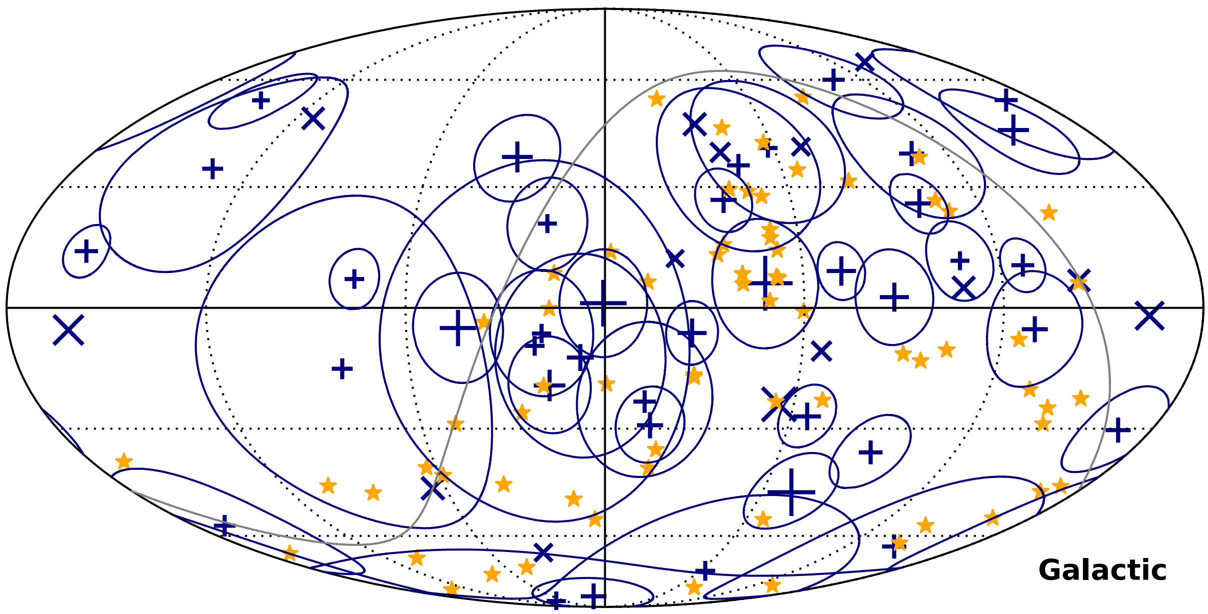


**Figure 3.1:** Arrival direction of ultra high-energy cosmic rays (orange stars) from Pierre Auger Observatory [42] and the arrival direction and median angular uncertainty of high-energy neutrinos (dark blue) in four years of HESE ('x': tracks, '+': cascades)

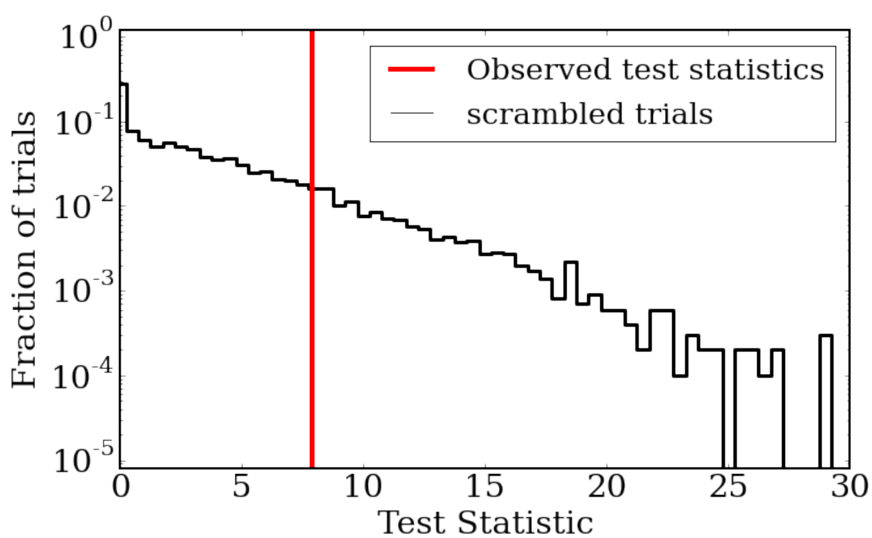


**Figure 3.2:** Distribution of test statistics results for scrambled data sets (black) for stacking likelihood test for Auger ultra high-energy cosmic rays. The red line denotes the observed test statistic.

the Telescope Array collaboration reports observation of a hotspot in these, with 20 degrees extension [43]. The arrival direction of ultra high-energy cosmic rays from Telescope Array are shown in Fig. 3.3.

The result of stacking likelihood analysis for these cosmic rays implies compatibility of the arrival direction of neutrinos with isotropic distribution and does not favor association of HESE events with Telescope Array's cosmic rays. The observed test statistic is about 0.1, which leads to p-value of 0.15. The distribution of test statistics for trials is illustrated in Fig. 3.4.

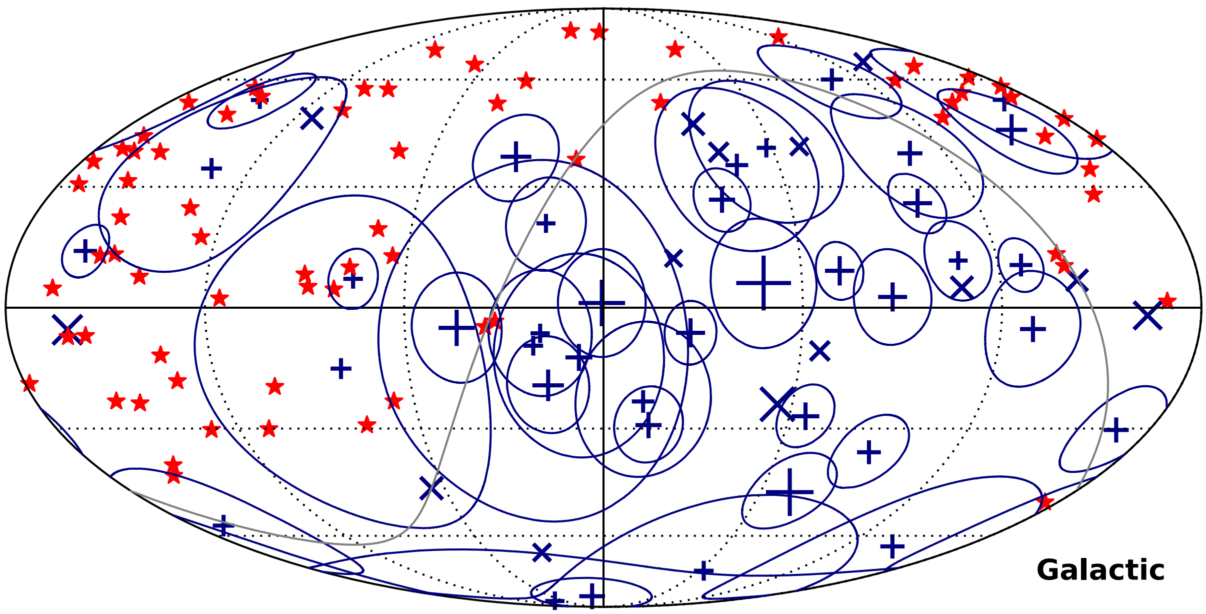


**Figure 3.3:** Arrival direction of ultra high-energy cosmic rays (red stars) from Telescope Array Observatory and the arrival direction and median angular uncertainty of high-energy neutrinos (dark blue) in four years of HESE ('x': tracks, '+': cascades)

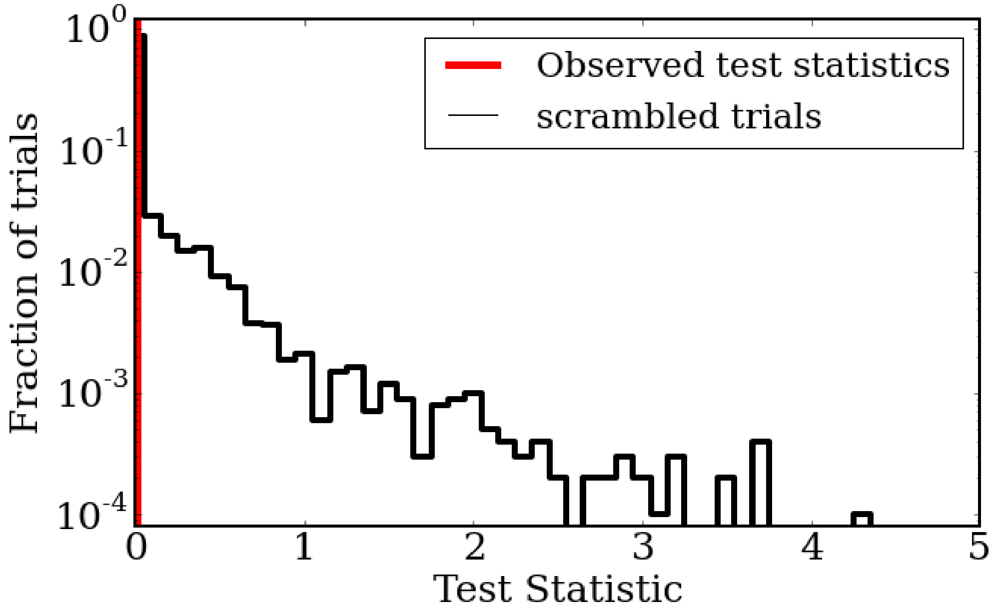


**Figure 3.4:** Distribution of test statistics results for scrambled data sets (black) for stacking likelihood test for Telescope Array ultra high-energy cosmic rays. The red line denotes the observed test statistic.

## 3.3 Correlation study with TeV gamma ray emitters (TeVCat)

The catalog of TeV gamma ray emitters (TeVCat) [44] is collected from observation of gamma ray observatories such as VERITAS, MAGIC, Whipple, HESS, Milagro, and etc. This catalog includes starburst galaxies, blazars, radio galaxies, pulsar wind nebula, molecular clouds, supernova remnants, and unidentified sources. From the view point of multi-messenger connection, it is expected that high-energy neutrinos with energies greater than tens of TeV share common origin with the TeV gamma ray emitters. Therefore, we search for any possible correlation of high-energy neutrinos with TeVCat sources. It should be noted that TeVCat is not a uniform, complete data set and most of the observations from gamma ray observatories are based on follow up observations. The location of the sources in TeVCat is shown in Fig. 3.5 with the arrival direction of HESE neutrinos.

Stacking likelihood analysis of TeVCat sources and high-energy neutrinos results in a p-value of 0.98. Implying that no association of observed neutrinos with TeV emitters identified in TeVCat has been observed. The distribution of test statistics in this search is shown in Fig. 3.6.

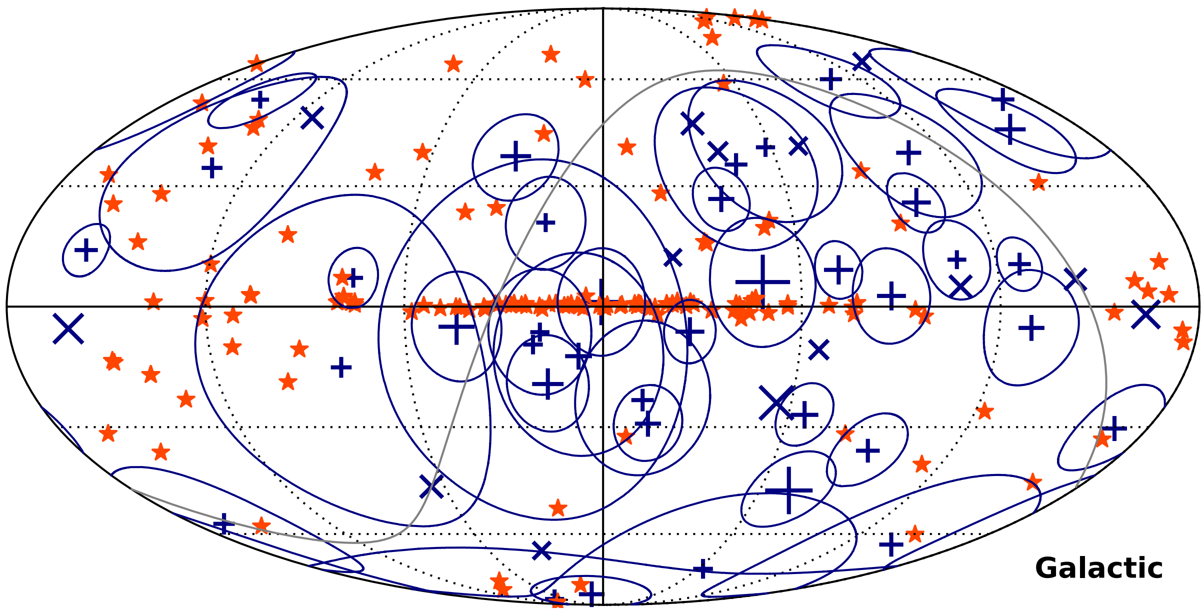


**Figure 3.5:** Position of TeV gamma ray emitter from TeVCat [44] (red stars) and the arrival direction and median angular uncertainty of high-energy neutrinos (dark blue) in four years of HESE ('x': tracks, '+': cascades)

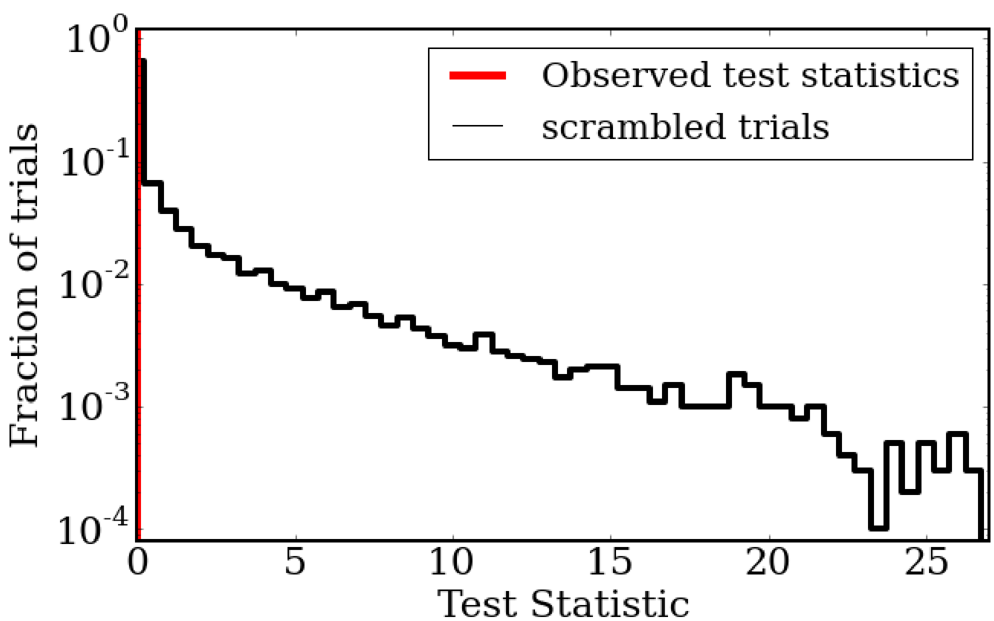


**Figure 3.6:** Distribution of test statistics results for scrambled data sets (black) for stacking likelihood test for TeVCat sources. The red line denotes the observed test statistic.

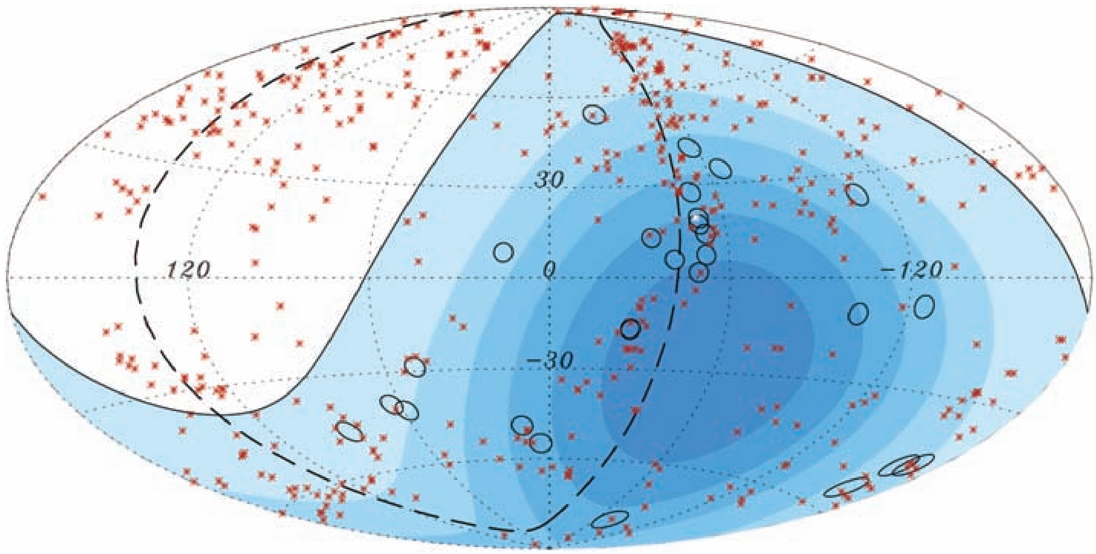


**Figure 3.7:** Association of ultra high-energy cosmic rays with active galactic nuclei [45]. The circles of radius 3.1 degrees are centered around arrival direction of ultra high-energy cosmic rays from Pierre Auger Observatory. Red asterisks show the position of active galactic nuclei with $z \leq 0.18$ from VCV12.

## 3.4 Correlation study with Vernon-Cetty Vernon catalog of AGN and Quasars

Active galactic nuclei are one of the few candidates for acceleration and production of ultra high-energy cosmic rays. An evidence for correlation between the arrival direction of ultra high-energy cosmic rays and the local active galactic nuclei (with redshift smaller than 0.18) was reported by Pierre Auger collaboration [45], see Fig. 3.7. Although this correlation has weakened in further years of observation [42], such association is expected provided that active galactic nuclei were the sources of ultra high-energy cosmic rays.

Here, we use Véron-Cetty Véron catalog of active galactic nuclei and quasars (VCV13) [46] that Auger collaboration used in their search to study the correlation with high-energy neutrinos. We also restrict to sources with redhift smaller than 0.18 (75 Mpc), which is the horizon for ultra high-energy cosmic rays to reach earth.

Arrival direction of high-energy neutrinos and the position of active galactic nuclei from VCV13 is shown in Fig. 3.8. Stacking likelihood analysis does not show any correlation between VCV13 active galactic nuclei and HESE neutrinos. This indicates that no correlation with a statistical significance exist between the two sets. Fig. 3.9 shows the distribution of test statistics.

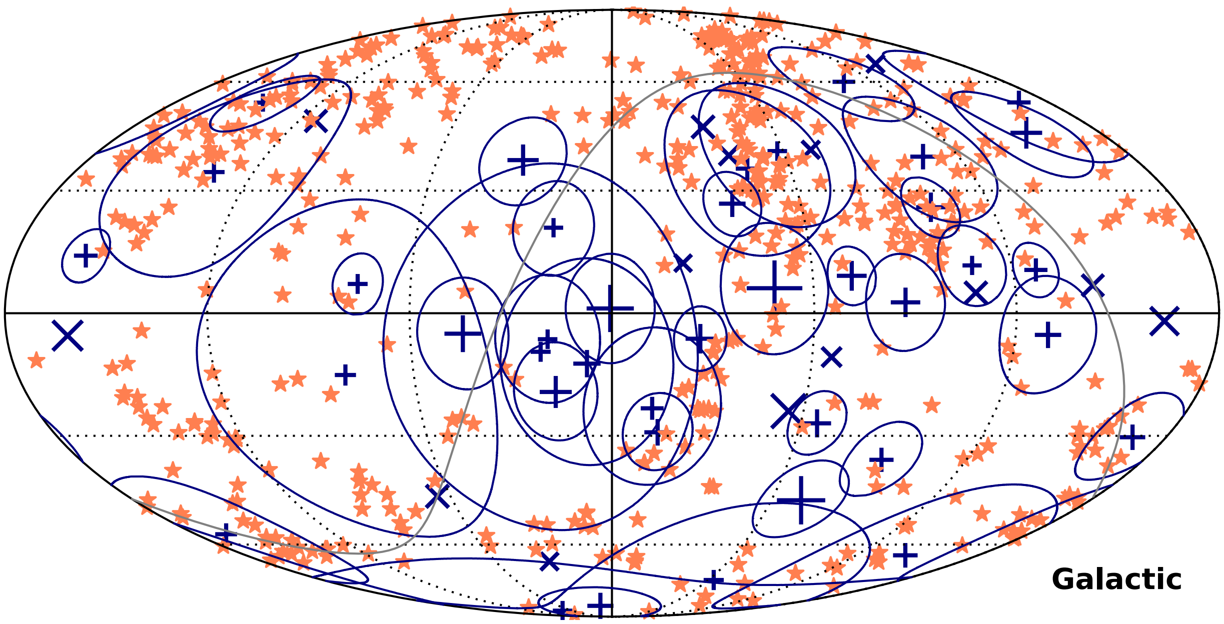


**Figure 3.8:** Position of active galactic nuclei with $z \leq 0.18$ from VCV13 [46] (corals stars) and the arrival direction and median angular uncertainty of high-energy neutrinos (dark blue) in four years of HESE ('x': tracks, '+': cascades)

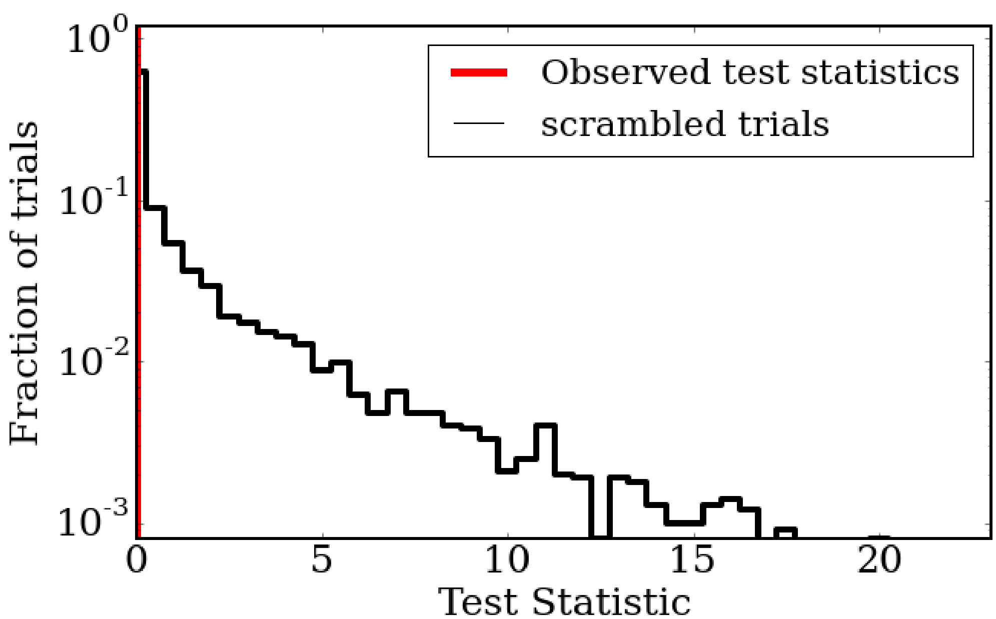


**Figure 3.9:** Distribution of test statistics results for scrambled data sets (black) for stacking likelihood test for VCV13 catalog of active galactic nuclei. The red line denotes the observed test statistic.

# Chapter 4

# High energy neutrinos from radio galaxies

## 4.1 Introduction

Active Galactic Nuclei (AGN) have long been discussed as one of the few possible source classes being able to accelerate particles up to the observed maximum energies of around $10^{20} - 10^{21}$ eV [47]. There exist different acceleration scenarios and the unified AGN model allows for different sub-AGN/classes to possibly be the dominant source of ultra high-energy cosmic rays. Both intrinsic properties as well as the orientation of the objects play a role in this respect. For a summary of a discussion concerning AGN sub-classes as neutrino emitters, see [14]. A schematic representation of AGN classes in the unified scheme is shown in Fig. 4.1. In particular, radio loud AGN are typically discussed as interesting candidates: although these only make up a fraction of about 10% of the entire AGN population, they have very powerful radio jets, not provided by radio quiet galaxies like Seyferts. Among radio loud galaxies, FR-I and FR-II type AGN are among the most prominent candidates, having powerful radio jet and being very frequent among the radio loud class of AGN.

As mentioned in Chapter 3, a first hint of an anisotropy in the ultra high-energy cosmic rays distribution at Earth was announced in [45], where ultra high-energy cosmic rays above $6 \times 10^{19}$ eV appear to show some correlation with the distribution of local AGN (within a distance of $\sim 75$ Mpc): as the flux of ultra high-energy cosmic rays at larger distances is expected to be absorbed at those energies by interactions with the Cosmic Microwave Background (CMB), such a clustering would be expected if AGN are the sources of ultra high-energy cosmic rays. Although there has not been a clear confirmation of the signal yet, the anisotropy persists at a low level and the nearest AGN Centaurus A - an FR-I type AGN - is discussed to

*This study has been published in* J. Becker Tjus, B. Eichmann, F. Halzen, A. Kheirandish, and S. M. Saba, Phys. Rev., vol. D89, no. 12, p. 123005, 2014 be responsible for a large fraction of the correlated events [48, 49]. The detection of high-energy gamma rays from Centaurus A [50, 51, 52] could be another hint for pion production in AGN, see e.g. [53], but it is not yet confirmed if the origin of the gamma rays is of hadronic or leptonic nature. Neutrinos, on the other hand, must be of hadronic origin and observation of high-energy neutrinos provides a unique opportunity to identify the sources of ultra high-energy cosmic rays.

Cosmic rays have been discussed to be able to be accelerated at different sites in AGN. Their acceleration in AGN cores would lead to photo-hadronic production of neutrinos [54, 55]. Shock acceleration in knots of AGN jets as they are observed in FR-I galaxies, or in the termination shock of the jet with the intergalactic medium as seen in FR-II galaxies, have been discussed as possible cosmic ray acceleration sites, see e.g. [47, 56, 57, 58]. These sites are connected to a specific column depth, and so, cosmic ray and gamma ray interactions with matter are an inevitable consequence of each acceleration scenario.

Only radio galaxies and proton-proton (*pp*) interactions are considered here. Photo-hadronic emission could potentially lead to an additional contribution to the neutrino flux at higher energies. This, and the uncertainties associated with photo-hadronic interactions will be discussed at the end.

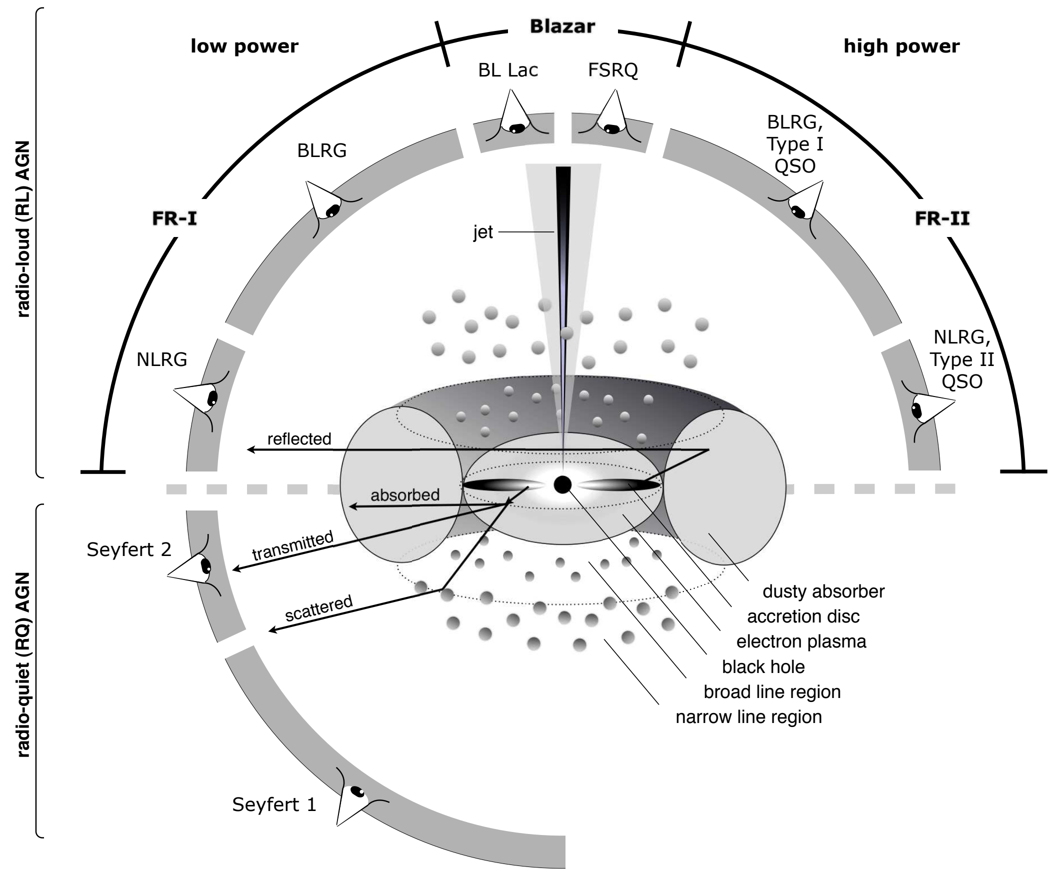


**Figure 4.1:** Schematic representation of AGN classes. The type depends on the viewing angle, and the power of the AGN. Graphic courtesy of Marie-Luise Menzel.

## 4.2 The neutrino flux at the source

Pions are produced in proton-proton interactions via $p\,p \to \pi^{0/\pm}$ and neutrinos are produced subsequently via the decay of the charged pions. In the following calculation the formalism introduced in [59] has been used to estimate the neutrino flux. It should be noted that Monte Carlo approaches like SIBYLL, QGSJet, EPOS or DPMJet provide much more detailed and up-to-date particle physics. However, the uncertainty included by using the analytic approximation is rather small when compared to the astrophysical uncertainties. Therefore, the delta-functional approach is used here. In the approach sketched by [59], the cross section for proton-proton interactions is assumed to be constant, $\sigma_{\rm pp} \approx 3 \cdot 10^{-26}$ cm$^2$ and the pion production efficiency of protons with an energy $E_p$ that is above the threshold energy $E_{\rm th}$ is given as

$$\xi_{\pi^\pm} = 2 \cdot \left(\frac{E_{\rm p} - E_{\rm th}}{\rm GeV}\right)^{1/4} . \tag{4.1}$$

The number of pions per energy and time interval $q_{\pi^\pm}(E_\pi)$ is related to the proton rate $q_{\rm p}(E_{\rm p}, \tau)$ as

$$q_{\pi^\pm} = \int_{E_{\rm th}}^{\infty} dE_{\rm p}\, \xi_{\pi^\pm}\, \delta\left(E_\pi - \langle E_\pi \rangle\right) \int_0^{\tau} d\tau'\, q_{\rm p}(\tau') \,, \tag{4.2}$$

where it is assumed that all energy is going to the average pion, $E_\pi \approx \langle E_\pi \rangle$.

Proton rate is determined by $q_{\rm p}(\epsilon, \tau) = j_{\rm p}(\epsilon)\, \exp(-\tau)$, where $j_{\rm p}(\epsilon)$ is the undamped rate $j_{\rm p}(\epsilon)$, and $\tau$ is the optical depth. Therefore pion rate at the source is described as:

$$q_{\pi^\pm} = \int_{E_{\rm th}}^{\infty} dE_{\rm p}\, (1 - \exp(-\tau))\, j_{\rm p}(E_{\rm p})\, \xi_{\pi^\pm}\, \delta\left(E_\pi - \langle E_\pi \rangle\right) . \tag{4.3}$$

Approximating for low optical depths, $\tau = l \cdot n \cdot \sigma_{\rm pp} < 1$, then

$$q_{\pi^\pm} = 1.6 \cdot n_H \cdot l \cdot \sigma_{\rm pp} \cdot \int_{E_{\rm th}}^{\infty} d\epsilon\ j_{\rm p}\, \xi_{\pi^\pm}\, \delta\left(E_\pi - \langle E_\pi \rangle\right) . \tag{4.4}$$

using $n \approx 1.6\, n_H$, which takes H-I, H-II and $H_2$ as well as He into account [59]. As discussed in [60], assuming only protons here does not change the results since different composition scenarios lead to scaling of the cross section. Here, $l$ is the length scale the cosmic rays traverse through the dense medium. The product of the density and the length scale can be abbreviated as the column density, $N_H = l \cdot n_H$. The threshold energy is close to the proton mass and is approximated to be $E_{\rm th} \approx m_{\rm p}\, c^2$.

The differential proton number per energy and time interval at the source is

$$j_{\rm p}(\epsilon) = A_{\rm p} \cdot \left(\frac{\epsilon - m_p \cdot c^2}{\rm GeV}\right)^{-p} . \tag{4.5}$$

Substituting $x := \langle E_\pi \rangle = \frac{1}{6}\left(\frac{E_{\rm p} - m_p\, c^2}{\rm GeV}\right)^{3/4}$ GeV gives a pion spectrum at the source of

$$q_{\pi^\pm}(E_\pi) \approx 26 \cdot N_H \cdot A_{\rm p} \cdot \sigma_{\rm pp} \cdot \left(\frac{6 \cdot E_\pi}{\rm GeV}\right)^{-\frac{4}{3}(p - \frac{1}{2})} . \tag{4.6}$$

The total neutrino rate at the source is then given by the sum of the first muon neutrino (directly from the pion), the second muon neutrino and the electron neutrino, both from the muon decay,

$$q_{\nu,\mathrm{tot}} = q_{\nu_\mu}^{(1)} + q_{\nu_\mu}^{(2)} + q_{\nu_e} \,. \tag{4.7}$$

The neutrino spectra are received from the pion spectrum by assuming that the total energy of the pions is distributed equally among the four produced particles

$$q_{\nu_i}(E_{\nu_i}) = q_\pi(4\,E_{\nu_i})dE_\pi/dE_{\nu_i} = 4 \cdot q_\pi(4\;E_{\nu_i}) \tag{4.8}$$

for each neutrino, $\nu_i = \overline{\nu}_e/\nu_e$, $\nu_\mu$, $\overline{\nu}_\mu$. Here, it depends on the charge of the pion if an electron or an anti-electron neutrino is produced. As IceCube does not distinguish between neutrinos and anti-neutrinos, we will neglect this piece of information in the following.

The total neutrino rate at the source becomes

$$q_{\nu,\mathrm{tot}} \approx 3 \cdot 10^2 \cdot N_H \cdot A_\mathrm{p} \cdot \sigma_\mathrm{pp} \cdot \left(\frac{24 \cdot E_\nu}{\mathrm{GeV}}\right)^{-\frac{4}{3}p+\frac{2}{3}} \,. \tag{4.9}$$

Equation 4.9 now provides the total neutrino flux at the source. The spectral behavior of the protons can be estimated from diffusive shock acceleration and is taken to be $p = 2$ here. The main free parameter in this calculation is the column density, $N_H$. The proton normalization for a radio galaxy can be estimated from radio observations as discussed in the next section.

## 4.3 Cosmic ray normalization

The normalization of the cosmic ray spectrum can be estimated from the following considerations: The radio luminosity of AGN, $L$, provides a measure for the AGN luminosity in electrons. The electron luminosity is equal to or larger than the radio luminosity of the source, as the latter is produced when electrons are accelerated and emit synchrotron radiation: $L_\mathrm{e} = \chi \cdot L$ with $\chi \geq 1$.

Hadronic cosmic rays and electrons are connected via a constant fraction $f_e$: $L_\mathrm{e} = f_e \cdot L_\mathrm{p}$,

$$L_\mathrm{p} = \int j_\mathrm{p}(\epsilon)\epsilon\, d\epsilon \approx \frac{\chi \cdot L}{f_e} \,. \tag{4.10}$$

Therefore, for $p = 2$, the normalization of the CR spectrum is:

$$A_{\mathrm{p}} = A_{\mathrm{p}}(L, z) = \frac{\chi}{f_e} \cdot \left[\ln\left(E_{\max}/E_{\min}\right)\right]^{-1} \cdot L\,\mathrm{GeV}^{-2} \tag{4.11}$$

For the case of $p \neq 2$,

$$\begin{aligned} A_{\mathrm{p}} &= A_{\mathrm{p}}(L, z) = \frac{\chi}{f_e} \cdot \frac{1}{-p+2} \\ &\cdot \left[\left(\frac{E_{\max}}{\mathrm{GeV}}\right)^{-p+2} - \left(\frac{E_{\min}}{\mathrm{GeV}}\right)^{-p+2}\right]^{-1} \\ &\cdot L \cdot \mathrm{GeV}^{-2} \end{aligned} \tag{4.12}$$

The uncertainties in the parameters of this result will be discussed later.

## 4.4 The diffuse neutrino flux from AGN

The *diffuse neutrino flux at Earth* is given as

$$\Phi_\nu = \int_L \int_z \frac{q_{\nu,tot}}{4\,\pi\, d_L(z)^2} \cdot \frac{dn_{\mathrm{AGN}}}{dV\, dL} \cdot \frac{dV}{dz}\, dz\, dL\,. \tag{4.13}$$

Here, $d_L$ is the luminosity distance, $\mathrm{d}n_{\mathrm{AGN}}/(\mathrm{d}V\,\mathrm{d}L)$ is the radio luminosity function of the AGN and $\mathrm{d}V/\mathrm{d}z$ is the comoving volume at a fixed redshift $z$. The radio luminosity function is usually represented by the product of a luminosity-dependent and a redshift-dependent function, $\mathrm{dn}_{\mathrm{AGN}}/(d\mathrm{V}\,d\mathrm{L}) = g(L) \cdot f(z)$. Including the single source flux Eq. 4.9 and the representation for the cosmic ray spectrum normalization given in Eq. 4.11, the diffuse neutrino flux can be parametrized as

$$\Phi_\nu = \zeta_c \cdot \zeta_z \cdot \zeta_L \cdot \left(\frac{E_{\nu,0}}{\mathrm{GeV}}\right)^{-\frac{4}{3}p+\frac{2}{3}}\,. \tag{4.14}$$

Here, the adiabatic energy losses is taken into account by $E_\nu = (1+z)\cdot E_{\nu,0}$, with $E_\nu$ as the energy at the source and $E_{\nu,0}$ the energy at the detector.The above introduced factors represent:

$$
\begin{aligned}
\zeta_c &\approx 2.4\cdot 10^{-4}\cdot 24^{-\frac{4}{3}p+\frac{2}{3}}\,\mathrm{GeV}^{-2} \\
&\cdot \begin{cases} \frac{1}{-p+2}\cdot\left[\left(\frac{E_{\max}}{\mathrm{GeV}}\right)^{-p+2}-\left(\frac{E_{\min}}{\mathrm{GeV}}\right)^{-p+2}\right]^{-1} & \text{for } p\neq 2 \\ \ln\left[\frac{E_{\max}}{E_{\min}}\right]^{-1} & \text{for } p=2 \end{cases} \\
&\cdot \left(\frac{\chi}{f_e}\right)\cdot\left(\frac{N_H}{10^{20}\mathrm{cm}^{-2}}\right) \qquad (4.15)\\
\zeta_L &= \int_{L_{\min}}^{L_{\max}} g(L)\cdot L\,dL \qquad (4.16)\\
\zeta_z &= \int_{z_{\min}}^{z_{\max}} \frac{1}{4\,\pi\,d_L^2\cdot(1+z)^{\frac{4}{3}p-\frac{2}{3}}}\cdot f(z)\,\frac{dV}{dz}\,dz\,. \qquad (4.17)
\end{aligned}
$$

Above, it is assumed that the energy range is $\ln(E_{\max}/E_{\min})\approx 6$, assuming approximately 3 orders of magnitude between minimal and maximal energy. This range corresponds to the observed ultra high-energy spectrum and probably extends towards lower minimal energies, but as the behavior is logarithmic, the expected changes are rather small and are neglected here. The neutrino rate from one single source is transformed into a flux at Earth by dividing by $1/(4\,\pi\,d_L^2)$ as we derive the flux from a radio luminosity given at the source. Hence, no additional redshift factor, but the redshift-dependent luminosity distance is needed, as this distance measure is defined to transform from luminosities at the source and fluxes at Earth.

### 4.4.1 Radio Luminosity Function

The radio luminosity function is expressed as the product of a redshift dependent part, $f(z)$ and a luminosity dependent part, $g(L)$,

$$\frac{dn_{\mathrm{AGN}}}{dV\,dL} = f(z)\cdot g(L)\,. \qquad (4.18)$$

Depending on what sub-class of AGN is considered, the behavior of the radio luminosity function can vary. As mentioned earlier, FR-I and FR-II galaxies are studied here.

Concerning FR-I and FR-II galaxies, Willott et al. [61] provide luminosity functions for $(\Omega_{\mathrm{M}},\,\Omega_\Lambda)=(1,\,0)$ and $(\Omega_{\mathrm{M}},\,\Omega_\Lambda)=(0,\,0)$. As the authors argue that their results for $(\Omega_{\mathrm{M}},\,\Omega_\Lambda)=(0,\,0)$ even reproduce a $\Lambda$CDM cosmology with $(\Omega_{\mathrm{M}},\,\Omega_\Lambda)=(0.3,\,0.7)$, we use their results for the $(\Omega_{\mathrm{M}},\,\Omega_\Lambda)=(0,\,0)$ cosmology, model C in the paper. For other redshift-dependent factors entering the calculation, we use a ΛCDM cosmology with $h = 0.7$ and $(\Omega_{\rm M},\, \Omega_\Lambda) = (0.3,\, 0.7)$.

The reference luminosity given at 0.151GHz and per steradian by [61] is converted into a total luminosity by multiplying with the frequency, 0.151 GHz and integrating over $4\pi$.

#### 4.4.1.1 FR-I galaxies

Generally, the luminosity-dependent part behaves as

$$g(L) = \frac{1}{\ln(10)\,L}\,\rho_0 \cdot \left(\frac{L}{L_\star}\right)^{-\alpha} \cdot \exp\left[-(\frac{L}{L_\star})^\beta\right] \tag{4.19}$$

Parameters for FR-I galaxies are $\rho_{0,FR-I} = 10^{-7.523}$ $\mathrm{Mpc}^{-3}$ $\Delta\log(L_{151})$, $\alpha = 0.586$, $L_{\star,FR-I} = 10^{42.76}$ erg/s and $\beta = 1$. FR-II galaxies have the parameter setting $\rho_{0,FR-II} = 10^{-6.757}$ $\mathrm{Mpc}^{-3}$ $\Delta\log(L_{151})$, $\alpha_{FR-II} = 2.42$ and $L_{\star,FR-II} = 10^{43.67}$ erg/s and $\beta = -1$.

The redshift dependence is parametrized as

$$f_{\rm FR-I}(z) = \begin{cases} (1+z)^\gamma & \text{for} \quad z < z_{0,FR-I} \\ (1+z_{0,FR-I})^\gamma & \text{for} \quad z \geq z_{0,FR-I} \end{cases} \tag{4.20}$$

where $z_{0,FR-I} = 0.710$ and $\gamma = 3.48$. Therefore, for FR-I galaxies

$$\zeta_{L,FR-I} = 7.8 \cdot 10^{37}\,\mathrm{GeV/(s\,Mpc^3)} \tag{4.21}$$

$$\zeta_{z,FR-I} = 240\,\mathrm{Mpc/sr} \tag{4.22}$$

The redshift-integrated factor $\zeta_{z,FR-I}$ (and later also $\zeta_{z,FR-II}$) is calculated in a ΛCDM cosmology, $(\Omega_m,\, \Omega_\Lambda) = (0.3,\, 0.7)$ with $h = 0.7$.

#### 4.4.1.2 FR-II galaxies

The radio luminosity function for FR-II galaxies similarly to FR-I galaxies, but with other parameters,

$$g_{\rm FR-II}(L)) = \frac{1}{\ln(10)\,L}\,\rho_0 \cdot \left(\frac{L}{L_\star}\right)^{-\alpha} \cdot \exp\left[-\frac{L}{L_\star}\right]\,. \tag{4.23}$$

Most importantly, the luminosity power-law dependence behaves inversely for the two samples. While FR-I galaxies become more frequent towards lower luminosities, the FR-II radio luminosity function cuts off at $L_\star$ and has a dominant contribution towards high-luminosity sources. This behavior reflects the division of FR-I and FR-II galaxies by their luminosities, FR-II galaxies representing the high-luminosity sample with dominant emission from the lobes, FR-I galaxies representing the low-energy sample with the main emission along the central part of the jet.

The redshift dependence for FR-II galaxies is given as

$$f_{\mathrm{FR-II}}(z) = \begin{cases} \exp\left(-\frac{1}{2}\left[\frac{z-z_{0,FR-II}}{z_1}\right]^2\right) & \text{for} \quad z < z_{0,FR-II} \\ \exp\left(-\frac{1}{2}\left[\frac{z-z_{0,FR-II}}{z_2}\right]^2\right) & \text{for} \quad z \geq z_{0,FR-II} \end{cases} \tag{4.24}$$

Parameters for the redshift dependence of FR-II galaxies are $z_{0,FR-II} = 2.03$, $z_{1,FR-II} = 0.568$ and $z_{2,FR-II} = 0.956$. Therfore, for FR-II galaxies

$$\zeta_{L,FR-II} = 1.6 \cdot 10^{39}\,\mathrm{GeV/(s\,Mpc^3)} \tag{4.25}$$

$$\zeta_{z,FR-II} = 4\,\mathrm{Mpc/sr}\,. \tag{4.26}$$

### 4.4.2 Doppler Boosting

Effects due to possible Doppler boosting cancel out in this calculation: the radio luminosity used in order to determine the proton density of the source is measured in the observer's frame. Thus, the additional factor based on the transformation of the luminosity from the observer's frame to the frame of the source vanishes due to the inverse transformation of the neutrino flux from the source to the observer's frame. Effects of area transformation cancel out as well, as the radio luminosity per steradian is transformed into a luminosity by multiplying by an opening angle of $4\pi$ and then divide by the same factor to account for the fraction of neutrinos that reaches Earth. Both factors scale with the boost factor in the same way.

## 4.5 Constraints on cosmic ray acceleration regions

Considering certain class of AGN as responsible for the IceCube diffuse flux, the total neutrino flux per flavor must match the observed flux,

$$\frac{1}{3}\left(\frac{E_{\nu,0}}{\mathrm{GeV}}\right)^2 \Phi_\nu = 1.2 \cdot 10^{-8}\,\mathrm{GeV}^{-1}\,\mathrm{cm}^{-2}\,\mathrm{s}^{-1}\,\mathrm{sr}^{-1} \tag{4.27}$$

$$= \frac{1}{3} \cdot \zeta_c \cdot \zeta_L \cdot \zeta_z\,. \tag{4.28}$$

Here, the measured flux is given per flavor. Comparing Eq. 4.28 with the prediction from Eq. 4.14, the column density of the interaction region in this scenario is constrained to

$$N_{H,FR-I} \approx 10^{24.57\pm1.0}\left(\frac{f_e}{0.06}\right)\left(\frac{100}{\chi}\right)\mathrm{cm}^{-2} \tag{4.29}$$

$$N_{H,FR-II} \approx 10^{25.03\pm1.0}\left(\frac{f_e}{0.06}\right)\left(\frac{100}{\chi}\right)\mathrm{cm}^{-2}\,. \tag{4.30}$$

using realistic parametrizations for $f_e$ and $\chi$ as shown in the following. The uncertainty estimate of about one order of magnitude is a combination of the uncertainties attached to the central parameters which is discussed in the following section.

## 4.6 Quantitative discussion of uncertainties

Main parameters and their uncertainties, which could be on the order of a factor of a few, are discussed in the following paragraphs.

### 4.6.1 Electron-to-proton luminosity ratio $f_e$

Assuming that AGN are the sources of ultra high-energy cosmic rays, the ratio between electron and proton luminosity, $f_e$ can be estimated empirically by comparing the average energy density rate, $\dot{\rho}_e$ (units: erg/(Mpc$^3$· yr)) that is obtained from integrating over all synchrotron output from AGN, using the RLF mentioned above; and $\dot{\rho}_{\mathrm{CR}}$ which is found by integrating over the observed CR spectrum from $E_{\mathrm{p}}^{\mathrm{min}}$. For $E_{\mathrm{p}}^{\mathrm{min}} \approx 3 \cdot 10^{18}$ eV, $f_e \approx 0.01$ (FR-I) and $f_e \approx 0.4$ (FR-II). Such an approach is common to use in order to correlate possible cosmic ray sources with the observed flux of cosmic rays, see e.g. [62]. While [62] apply this strategy to gamma ray bursts, we use it for FR-I and FR-II galaxies.

From theoretical considerations (see e.g. [63]), for equal spectral indices of electrons and protons at injection, the ratio of the luminosities should be $f_e \approx (m_e/m_p)^{(p-1)/2} \approx 0.02$ for a primary spectral index of $p = 2$. While this value is subject to change in case of spectral indices deviating from $p = 2$, the ratio is certainly to be expected to be $f_e \ll 1$. Thus, the values received for FR-I or FR-II galaxies respectively, seem to be a realistic range: $0.01 < f_e < 0.4$.

As it is extremely difficult to pinpoint the exact value, $f_e = 10^{-1.2}$ is used, so that a symmetric uncertainty $\Delta f_e \approx 10^{\pm 0.8}$ is obtained. Thus, a higher value of $f_e$ would lead to a density increase, so the density could become at maximum a factor of 6 higher.

### 4.6.2 Radio-electron correlation $\chi$

In the above calculation, it is assumed that the electron luminosity corresponds to a factor of a few of the observed radio luminosity, where $\chi = 100$ is chosen. It is clear that synchrotron radiation from electrons is distributed over a wider energy range and that not necessarily all energy is radiated. Assuming that the relativistic electrons have a power law distributed energy with a spectral index $p$ and predominantly lose their energy via synchrotron emission, $\chi$ is subsequently determined by the ratio of electron and radio emissivity. In the case of $p = 2$ the electron emissivity (in units of eV cm$^{-3}$ ster$^{-1}$ s$^{-1}$) yields $\rho_e \propto \ln(\gamma_{\max}/\gamma_{\min})$, where $\gamma_{\min}$ and $\gamma_{\max}$ is the minimal and maximal Lorentz factor of the electrons, respectively. The radio emissivity $\rho_{\rm radio}$ is determined by integrating the synchrotron emission coefficient in the radio band, i.e. between $\nu_{\min} = 100\,\mathrm{MHz}$ and $\nu_{\max} = 5\,\mathrm{GHz}$. Since the radio emission is determined by the rising part of the synchrotron emission spectrum, the spectral synchrotron power is accurately approximated by [64], $P(\nu,\, \gamma) = 1.19\, P_0\, (\nu/(\nu_s\, \gamma^2))^{1/3}\, H[\nu_s \gamma^2 - \nu]$, with $P_0 = 2.64 \times 10^{-10} (B/1\,\mathrm{G})\,\mathrm{eV\,s^{-1}\,Hz^{-1}}$ and $\nu_s = 4.2 \times 10^6\, (B/1\,\mathrm{G})\,\mathrm{Hz}$. Thus, the spectral cut-off by the Heaviside function yields in the case of $p = 2$ and $\nu_s \gamma_{\max}^2 > \nu_{\max} > \nu_{\min}$ the following three different $\chi$-dependencies

$$\chi = \frac{\rho_e}{\rho_{\rm radio}} = \frac{32\pi\, m_e c^2}{3\, P_0\, \tau_0}\, \nu_s^{\frac{1}{3}}\, \ln(\gamma_{\max}/\gamma_{\min}) \cdot \begin{cases} (a-b)^{-1}\,, & \text{for } \nu_s\, \gamma_{\min}^2 < \nu_{\min}\,, \\ (c_s + a_s - b_s)^{-1}\,, & \text{for } \nu_{\min} \leq \nu_s\, \gamma_{\min}^2 \leq \nu_{\max}\,, \\ d^{-1}\,, & \text{for } \nu_s\, \gamma_{\min}^2 > \nu_{\max}\,, \end{cases} \tag{4.31}$$

with the synchrotron cooling timescale $\tau_0 = 7.7 \cdot 10^8\, (B/(1\,\mathrm{G}))^{-2}\,\mathrm{s}$.

The parameters are

$$\begin{aligned}
a &= \nu_s^{\frac{4}{3}} \ln\left(\nu_{\max}/\nu_{\min}\right) \,, &(4.32)\\
b &= \tfrac{3}{4}\gamma_{\max}^{-\frac{8}{3}}\left(\nu_{\max}^{\frac{4}{3}}-\nu_{\min}^{\frac{4}{3}}\right) \,, &(4.33)\\
d &= \tfrac{3}{4}\left(\gamma_{\min}^{-\frac{8}{3}}-\gamma_{\max}^{-\frac{8}{3}}\right)\left(\nu_{\max}^{\frac{4}{3}}-\nu_{\min}^{\frac{4}{3}}\right) \,, &(4.34)\\
a_s &= \nu_s^{\frac{4}{3}} \ln\left(\nu_{\max}/(\nu_s\gamma_{\min}^2)\right) \,, &(4.35)\\
b_s &= \tfrac{3}{4}\gamma_{\max}^{-\frac{8}{3}}\left(\nu_{\max}^{\frac{4}{3}}-(\nu_s\gamma_{min}^2)^{\frac{4}{3}}\right) \,, &(4.36)\\
d_s &= \tfrac{3}{4}\left(\gamma_{\min}^{-\frac{8}{3}}-\gamma_{\max}^{-\frac{8}{3}}\right)\left((\nu_s\gamma_{\min}^2)^{\frac{4}{3}}-\nu_{\min}^{\frac{4}{3}}\right) \,. &(4.37)
\end{aligned}$$

The above equations indicate that the spectral cut-off by the Heaviside function yields three different $\chi$-dependencies at (1.) $\nu_s < \nu_{\min}\,\gamma_{\min}^{-2}$, (2.) $\nu_{\min}\,\gamma_{\min}^{-2} \leq \nu_s \leq \nu_{\max}\,\gamma_{\min}^{-2}$ and (3.) $\nu_s > \nu_{\max}\,\gamma_{\min}^{-2}$.

Consequently, $\chi$ depends on the magnetic field strength of the considered emission area, where $B$ generally decreases with increasing distance from the central engine of the AGN and therefore varies between some mG to a few kG.

Figure 4.2 shows the dependence of $\chi$ on the magnetic field strength for different choices of $\gamma_{\min}$ and $\gamma_{\max}$. Since FR-I and FR-II galaxies emit a significant amount of energy at radio energies, the electrons are expected to cool down till a minimal Lorentz factor $\gamma_{\min} \leq \sqrt{\nu_{\max}/\nu_s} \simeq 10^{3/2}\,(B/1\,\mathrm{G})^{1/2}$, so a value somewhere in between $\gamma_{\min} = 1-10$. The maximum energy reached in the acceleration process itself (not including losses, only acceleration) must be around $\gamma_{\max} = 10^{10\pm1}$ in order to explain the observed cosmic ray spectrum which reaches up to $E_{\mathrm{CR,max}} \approx 10^{20}$ eV. This maximum energy, if dominated by iron, could be a factor of $Z = 26$ lower for protons due to the dependence of the acceleration process on the charge $Z$. Thus, a range of $\gamma_{\max} = 10^9 - 10^{11}$ seems plausible. The uncertainty of the maximal Lorentz factor of the electrons produce only an uncertainty factor of about $\Delta\chi \approx 10^{\pm0.2}$. The choice of the minimum of the Lorentz factor determines at which critical magnetic field strength $B_{\mathrm{c}}$ the factor $\chi$ goes from being constant to increasing with a power-law, see Fig. 4.2. At the most extreme case of $\gamma_{\min} = 1$, $\chi$ becomes significantly larger from $B_{\mathrm{c}} \sim 10$ Gauss, for $\gamma_{\min} = 10$, the relation between $\chi$ and $B$ stays approximately constant within a factor of 2 below $B < 30$ Gauss.

Therefore, $\chi$ is constant around 100 for magnetic fields of $B < 10$ Gauss and that it increases at higher magnetic fields. This behavior is taken into account in the interpretation of the results. In general, $\chi$ is around $10^{2\pm0.2}$ and independent of the magnetic field strength when the emission region is at a distance

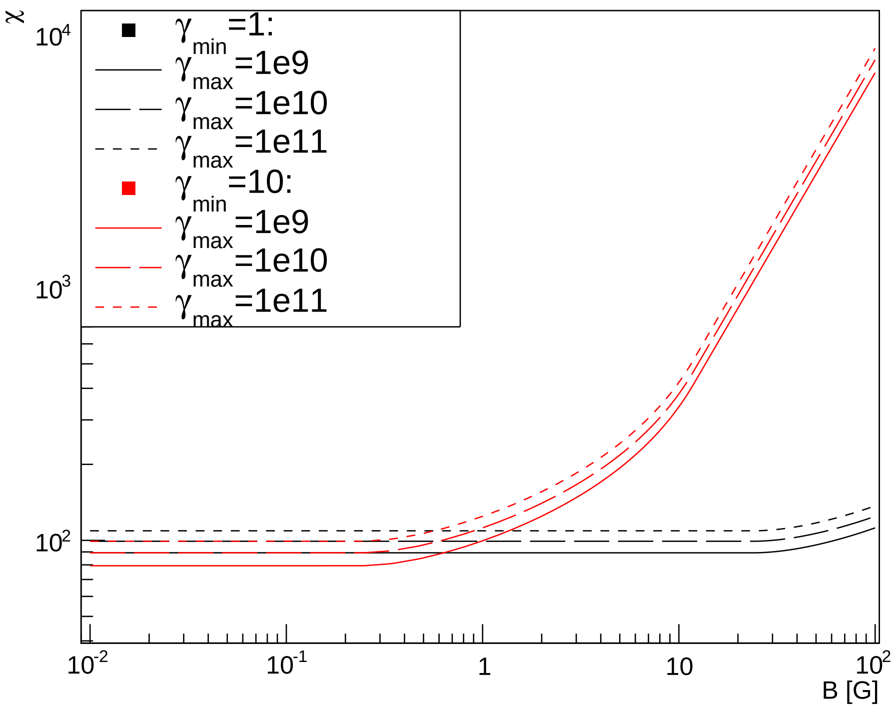


**Figure 4.2:** Dependence of the factor $\chi$ on the magnetic field strength $B$. Uncertainties from the primary electron spectrum, i.e. maximum and minimum Lorentz factor $\gamma$, lie below $10^{\pm 0.2}$.

of more than about a parsec from the central engine of the AGN due to the correlated $B$-regime where $\nu_s\,\gamma_{\min}^2 < \nu_{\min}$.

### 4.6.3 Radio Luminosity Function

The two AGN sub-classes used here, FR-I and FR-II galaxies, represent the two most extreme scenarios of source evolution, one population having a large contribution from low-luminosity sources, one being focused on high-luminosity sources. The final result is still somehow compatible, as the differences in redshift dependence and luminosity dependence cancel out. If one separately considers the differences in the results for $\zeta_L$ and $\zeta_z$, there is a factor of $\sim 10$ variation in each of the factors. When comparing the same source classes, the uncertainties are expected to be much smaller, on the order of a factor of $\sim 2-3$ for the product of $\zeta_L$ and $\zeta_z$. The main reason is that both factors are mainly dominated by the integration limits, as they have very strong evolving integrands. So, changing the functions themselves does not change too much in the total result. We thus apply a maximum of a factor of 3 uncertainty from this, so $10^{\eta \pm 0.5}$, where $\eta = \log[(\zeta_z \cdot \zeta_L)/(\mathrm{GeV\,Mpc^{-2}\,s^{-1}\,sr^{-1}})]$ for FR-I and FR-II galaxies.

## 4.7 Results

In the previous sections, it was showed that proton-proton interactions can produce a neutrino signal of a given strength for a fixed combination of magnetic field strength $B$ and column depth $N_H = n_H \cdot l$ at the source. Uncertainties in the calculation of approximately one order of magnitude are applied using an uncorrelated Gaussian error estimate to combine the uncertainties in the parameters discussed above. This constrains the possible acceleration site in the $(B, N_H)$-space.

The results are shown in Fig. 4.3. The shaded band represents the parameter space for $(N_H,\, B)$ derived from the IceCube observations, applying the above-discussed error of $10^{\pm 1.0}$ to the region in which the parameter $\chi$ is constant, i.e. for $B < B_c$ as discussed before. At higher magnetic fields, we show the range possible for $1 < \gamma_{\min} < 10$.

The radio emission from electron synchrotron radiation, used to determine the neutrino flux, comes from the knots in the case of FR-I galaxies and from the lobes for FR-II galaxies. We therefore compare the shaded band for FR-I galaxies with the approximate parameters in the knots. For the calculation of the column depth, assuming that a density of $\sim 10^9$ cm$^{-3}$ and a knot size of $10^{-3}$ pc close to the foot of the jet, see [58]. As the density decreases, the knot size increases with the distance $z$ from the foot of the jet, so that the column is expected to stay approximately the same. The most important contribution is expected to come from the foot of the jet, see [65]. The magnetic field decreases with the distance along the jet $z$ as well, $B(z) \sim B_0 \cdot (z/z_0)^{-1}$ [66], see [65] for a discussion of neutrino production in that context. In the graph, we indicate the highest magnetic fields, $B_0 \sim 0.1 - 10$ Gauss. For lower fields, which should be present along the jets for large $z$ [67], our results do not change. These considerations result in a possible parameter range for FR-I galaxies of $(N_H,\, B) = (10^{24\pm1}\mathrm{cm}^2,\, 10^{0.5\pm0.5}$ Gauss). This realistic range of parameters for FR-I galaxies is now compared with the allowed range if the IceCube signal should be explained by emission from FR-I galaxies. This is shown in the left panel of Fig. 4.3. The knots fall right into the allowed region and we therefore consider FR-I galaxies as a serious candidate as the sources for the detected IceCube signal. The right plot of Figure 4.3, on the other hand, shows that FR-II lobes are far too less dense to produce the signal. For the calculation of the column depth present in FR-II radio lobes, a density of $0.01 - 0.1$ cm$^{-3}$ is assumned, as the jets meet the intergalactic medium, and a lobe size of $10^{22} - 10^{23}$ cm, see e.g. [68]. The

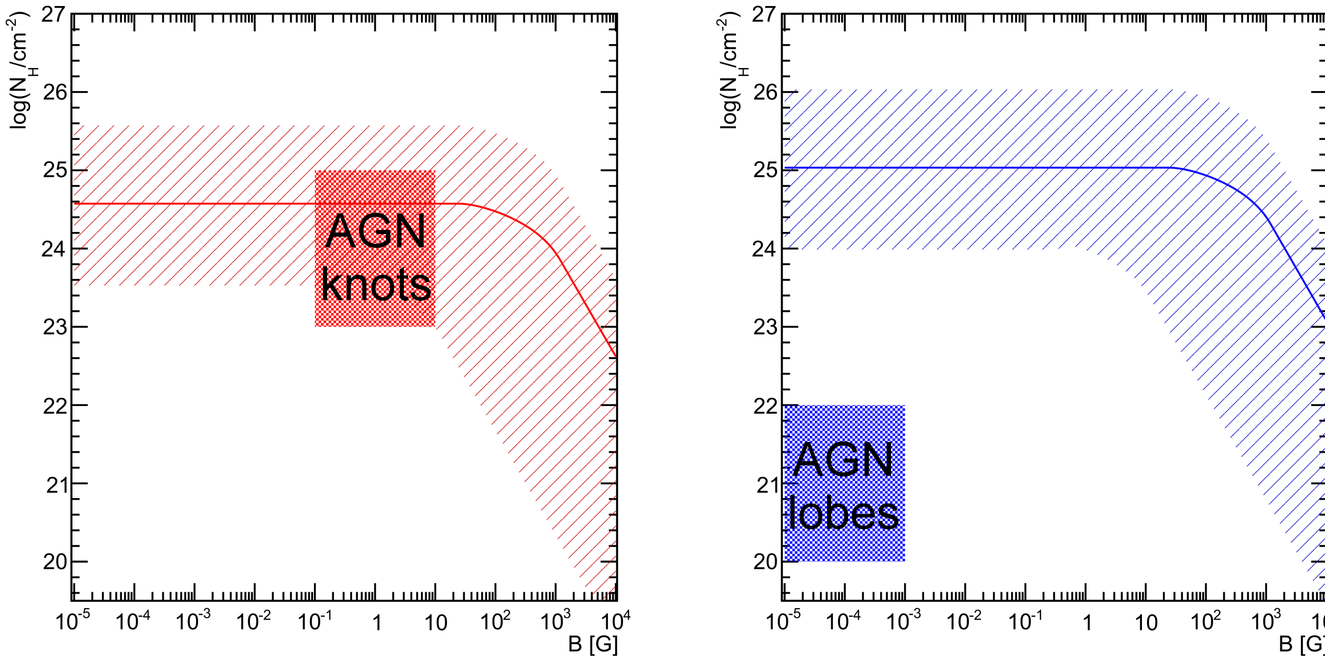


**Figure 4.3:** Allowed parameter range for column density $N_H$ and magnetic field strength $B$ in FR-I (left panel) and FR-II (right panel) galaxies. The dashed areas represent the regions derived including uncertainties in the calculation, dominated by the parameters $\eta$, $\chi$ and $f_e$, as discussed in the text. The encircled areas mark the approximate position of the knots and lobes, producing the radio signal in the respective calculation.

approximate value of the magnetic field is taken from [67], i.e. $(N_H,\, B) = (10^{21\pm1}\text{cm}^2,\, 10^{-4\pm1}$ Gauss) for the lobes. Thus, proton-proton interaction in radio lobes of FR-II galaxies can be excluded as the sources of the IceCube signal.

It should be noted that this discussion only includes proton-proton interactions, and does not take into account photo-hadronic interactions of cosmic rays with ambient photon fields. In principle, proton-photon interactions could contribute to a possible signal in the lobes, see [69] for discussion. As it is kinetically necessary to produce the delta resonance, however, a relatively high-energy photon field needs to be present in order to produce a high optical depth for the process. With the dominant electromagnetic emission coming from radio wavelengths in the lobes, this seems rather unlikely.

In order to show what the results mean in terms of the absolute neutrino flux, the estimates for FR-I and FR-II galaxies are shown in Fig. 4.4. For FR-I galaxies in the case of an $E^{-2}$ spectrum, we use a column of $N_H \sim 10^{24.5}$ and assume that the magnetic field on average is lower than 10 Gauss. Also a spectrum corresponding to an $E^{-2.2}$ proton injection spectrum is shown. Here, a column of $10^{23.6}$ is used, required to approximately match the IceCube data. In this approximate way, the number is compatible with what is expected from the observation of the column density from radio galaxies. The general result does not change for an $E^{-2.2}$ spectrum: FR-I galaxies are still well-compatible with the observations, while FR-II galaxies have too low columns.

The flux is well-suited to explain the IceCube signal. Definitely, more tests are clearly necessary to prove (or disprove) this model. A smoking gun would of course be the detection of the nearest point sources, which would be M87 and Cen A [53], or possibly a stacked signal of the nearest FR-I galaxies, see [70] and references therein. Further, future observations by IceCube will show if the spectrum really does persist beyond PeV energies or if there is a cutoff at PeV energies. In the latter case, AGN can be excluded if the flux should at the same time be associated with the production of ultra high-energy cosmic rays. In that case, a cutoff in the spectrum should only be present at $\sim 10^3 - 10^4$ PeV. On the other hand, AGN models are very well compatible with energy spectra slightly steeper than $E^{-2}$. Gamma ray observations of Cen A and M87 would even indicate a spectral behavior close to $E^{-2.3}$ rather than $E^{-2}$ (see [53] and references therein).

For FR-II galaxies, we use the most optimistic case of a column depth of $N_H \sim 10^{22}$ cm$^{-2}$. It would be extremely difficult to raise the level of this flux by tuning the parameters by the three orders of magnitude needed to explain the IceCube signal. It is obvious from Fig. 4.4 that this emission scenario can be excluded from the possible list of sources for the IceCube signal. This result supports the study of proton-proton interactions in the lobes of Centaurus A, which are also discussed to be too weak to contribute significantly to a neutrino signal [71].

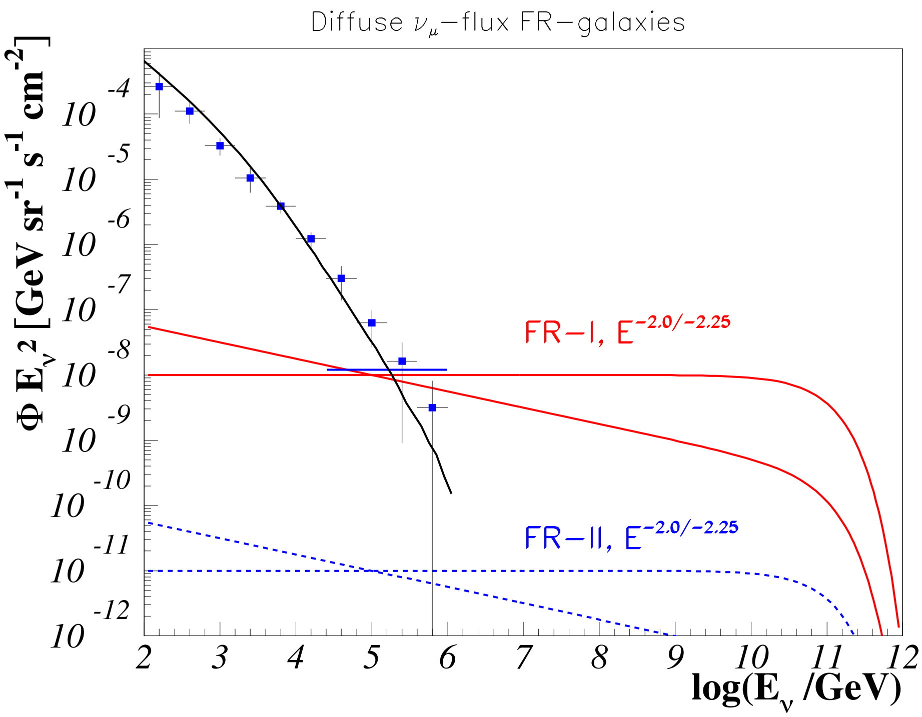


**Figure 4.4:** Expected neutrino flux for FR-I galaxies (solid, red line) and FR-II galaxies (dashed, blue line). For FR-I galaxies, an average value for the column depth of $N_H = 10^{24.5}$ cm$^{-2}$ and a magnetic field $B < 10$ Gauss are used, which are realistic parameters, see Fig. 4.3. In addition, we show the potential flux, close to what is expected from IceCube if the measured flux is steeper than $E^{-2}$. Concretely, we show a proton spectrum of $E^{-2.2}$, which translates to a neutrino spectrum close to $E^{-2.25}$. For FR-II galaxies, we use the most optimistic assumption of a column depth of $10^{22}$ cm$^{-2}$ and a B-field of $B < 10$ Gauss.

## 4.8 Summary

The conditions required to prevail in an acceleration environment in FR-I and FR-II radio jets in order to provide a cosmic ray interaction site which is capable of explaining the observed IceCube signal. Assuming that leptonic and hadronic cosmic rays are accelerated at the same site at a constant luminosity ratio and that the observed synchrotron radiation from AGN represents a part of the energy budget available in cosmic ray electrons. The exact fraction of radio-to-electron energy depends on the magnetic field at the acceleration site, which turns out to be one of the free parameters connected to the acceleration site. A second parameter in the calculation is the column depth at the interaction site.

We estimated the uncertainties connected to the determination of the column depth in dependence on the magnetic field. For the electron-to-proton ratio, this lies at $f_e = 10^{-1.2\pm0.8}$. The factor $\chi$ is shown to be known within $\chi = 10^{2\pm0.2}$. For the luminosity and redshift factors, we have taken into account an uncertainty of $\Delta(\zeta_L \cdot \zeta_z) = 10^{\pm0.5}$, associated with the uncertainty in the luminosity function.

Considering the observed flux of high-energy neutrinos with IceCube at a level of $10^{-8}\,\frac{\mathrm{GeV}}{\mathrm{cm^2\,s\,sr}} \cdot E_{\nu,0}^{-2}$, for magnetic fields at the acceleration site of $B < 10$ Gauss, a column depth of $N_H \sim 10^{24.5}$ cm$^{-2}$ (FR-I) and $N_H \sim 10^{25}$ cm$^{-2}$ cm$^{-2}$ (FR-II) is needed in order to explain the observed astrophysical signal as coming from FR-I or FR-II radio jets, respectively. For higher magnetic fields, the column depth must be lower. This is an effect of decreasing contribution of the electron population to the flux radiated at radio wavelengths. Here, we discuss two scenarios as examples:

1. Acceleration and interaction in AGN knots: with a column of $\sim 10^{24\pm1}$ cm$^{-2}$ and a magnetic field of around $1-10$ Gauss we find that AGN knots are well-suited to explain the observed signal with proton-proton interactions from FR-I galaxies.

2. Acceleration and interaction in AGN lobes of FR-II galaxies: here, the column depth is too low $\sim 10^{21\pm1}$ cm$^{-2}$ at a given magnetic field of $\sim 10^{-4\pm1}$ Gauss in order to explain the signal with proton-proton interactions. It might still be possible to produce the neutrino flux via photo-hadronic interactions.

Determination of the spectral behavior with high significance will already help to further exclude source models. The model presented here predicts that the neutrino spectrum persists up to far beyond PeV energies. This condition comes from the assumption that these neutrinos are directly connected to the extragalactic flux of ultra-high energy cosmic rays. If a cutoff at PeV energies is observed, the sources proposed here can be excluded as a possible class for the detected neutrinos. In that case, starburst galaxies, with a cutoff below or probably at 1 PeV would be an interesting alternative, see e.g. [65, 72].

Identification of point sources responsible for the so-far diffuse high-energy neutrino flux will ease the investigate both the source class and the exact emission region within the specific source and by that identify the sources of ultra high-energy cosmic rays. The relation between the diffuse neutrino flux and the contribution from point sources will provide information on the luminosity function of the sources of ultra high-energy cosmic rays. Another important piece of information will be provided through the exact measurement of the spectral behavior of the astrophysical flux.

Here, the focus was on radio galaxies. Another option would be to discuss blazars, where the boosted emission of the jet by directly pointing towards the observer. A model of blazar emission is presented in [73] where the focus lies on the modeling of the photon fields and has difficulties to explain the IceCube results. We refrain from modeling these blazars as well as the effects of photo-hadronic emission in order to keep ourselves to as little parameters as possible: as for the blazars, both the luminosity function and boosting effects lead to relatively high uncertainties. Concerning photo-hadronic emission scenarios, a primary source of uncertainty comes from the composition of cosmic rays. For a large fraction of heavy nuclei, the neutrino flux is significantly reduced with respect to a pure proton flux. In addition, the spectral shape of the neutrino spectrum from photo-hadronic interactions is highly sensitive to the shape and bandwidth of the target photon field. The main effect comes from the fact that a delta resonance needs to be produced.

The framework represented here for producing neutrinos in AGNs accommodates the diffuse flux observed by IceCube; when the neutrino production happens in the relatively dense matter near the black hole. A different scenario that argues radio galaxies are responsible for IceCube flux is presented in [74] where high-energy cosmic rays are confined within the volumes of radio galaxies, where they interact with gas to generate the observed diffuse fluxes of neutrinos and gamma rays. In yet another scenario, Wang and Loeb argue that quasar driven outflows interact with interstellar protons to produce IceCube's neutrinos [75].

# Chapter 5

# High energy neutrinos from blazar flares

## 5.1 Introduction

The energy density of cosmic neutrinos measured by IceCube matches the one observed by Fermi in extragalactic photons that predominantly originate in blazars. This has inspired attempts to match Fermi sources with IceCube neutrinos. A spatial association combined with a coincidence in time with a flaring source may represent a smoking gun for the origin of the IceCube flux. In June 2015, the Fermi Large Area Telescope observed an intense flare from blazar 3C 279 that exceeded the steady flux of the source by a factor of forty for the duration of a day. In this chapter, we study the prospects for IceCube to observe neutrinos, if indeed hadronic in origin, from the flare in data that are still blinded at this time. We also discuss other opportunities for coincident observations that include a recent flares from blazar 1ES 1959+650 that previously produced an intriguing coincidence with AMANDA observations.

The higher statistics data observed by IceCube reinforce the observation that the flux is predominantly extragalactic, and as mentioned before reveal a flux of neutrinos with a total energy density that matches the one observed by Fermi in extragalactic gamma rays. This has bolstered the speculation that blazars, which are responsible for the majority of Fermi photons, are the sources of cosmic neutrinos.

Blazars are a subclass of active Galactic nuclei (AGN) with collimated jets aligned with the line of sight of the observer. With gamma-ray bursts, they have been widely speculated to be the sources of the highest energy cosmic rays and of accompanying neutrinos and gamma rays of pionic origin. Recent studies with the Fermi Large Area Telescope (Fermi LAT) have shown that blazars are responsible for more than 85% of the extragalactic gamma-ray background (EGB) [76]. From that along with the fact that a gamma-ray

*This study has been published in* F. Halzen and A. Kheirandish, Astrophys. J., vol. 831, no. 1, p. 12, 2016.

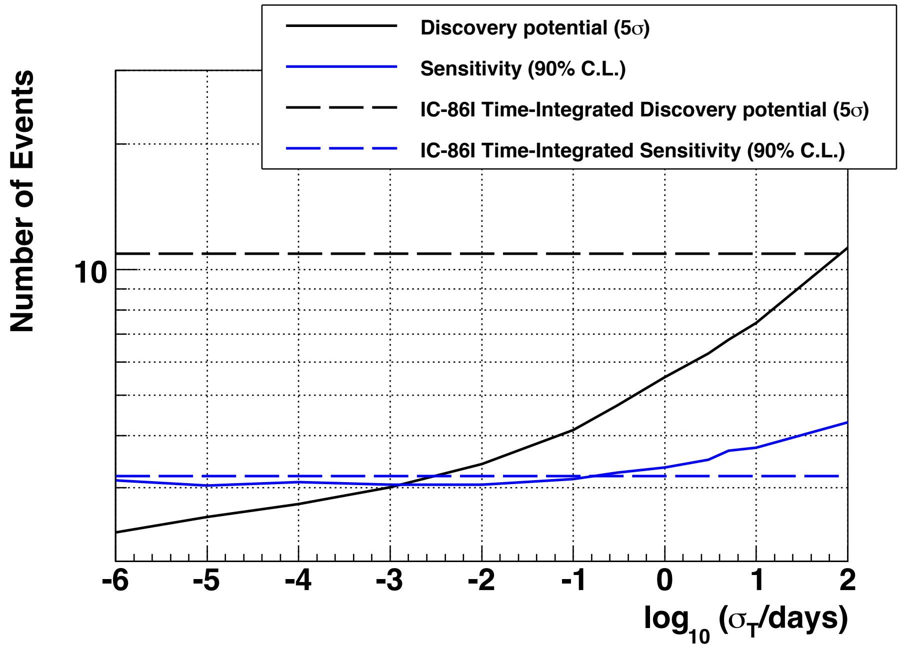


**Figure 5.1:** $5\sigma$ discovery potential and sensitivity of IceCube in terms of mean number of signal events for a source at declination $16°$ with $E^{-2}$ spectrum [80].

flux from neutral pions, accompanying the flux of the charged pions responsible for the IceCube neutrinos, matches the Fermi flux [77, 36], blazars emerge as a plausible source of cosmic neutrinos. Recent studies have argued for a correlation between cosmic neutrinos and blazar catalogs [78]. Because blazars are flaring sources coincident in time as well in direction, they provide a powerful opportunity to make the case for such a connection, possibly with a single observation. The recent association of the second highest energy neutrino event of 2 PeV with the blazar PKS B1424-418 provides an interesting hint in this context [79].

It is worth mentioning that in principle, temporal coincident neutrino with a transient source will provide a more statistical power to pinpoint the source of high energy neutrinos thanks to the lower background rates. Fig. 5.1 shows the discovery potential for transient sources with respect to the flaring time. It is easy to see that even observation of few events coincident in time meets discovery potential criteria.

The blazar spectral energy distribution generically has two components with two peaks in the IR/X-ray and the MeV/TeV photon energy ranges. The two components can typically be described in *leptonic* and *hadronic* scenarios where the acceleration of electrons and protons, respectively, are the origin of the high-energy photons. In the leptonic scenario, synchrotron radiation by electrons is responsible for the

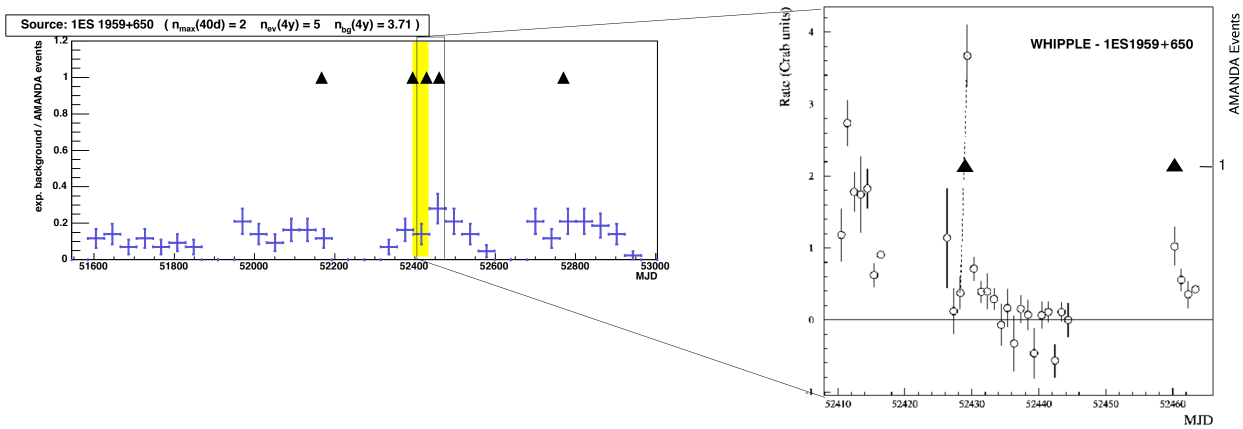


**Figure 5.2:** Left: AMANDA-II neutrino candidates within 2.25° from the direction of the blazar 1ES 1959+650. The triangles indicate the arrival time of the observed events; the crosses refer to the background events in the 40-days windows. The window showing the highest multiplicity is highlighted. Right: Zoom-in of the time-window MJD 52410-52460. The arrival time of two out of the five AMANDA-II events is compared with the Whipple light curve. [84]

first peak, and Inverse Compton scattering on electrons produces the second [81]. In hadronic models [82], both protons and electrons are accelerated. Synchrotron radiation still produces the low-energy peak in the spectrum, while the high-energy MeV/TeV photons are the decay products of pions produced in *pp* or $p\gamma$ interactions in the jet. In one model, the protons interact with the synchrotron photons, for instance. The charged pions inevitably produced with neutral pions will be the parents of neutrinos that provide incontrovertible evidence of cosmic-ray acceleration in the source. Therefore, the detection of high-energy neutrinos accompanying photons represents direct evidence for the hadronic model of blazars.

The multiwavelength association of blazars and neutrinos is greatly facilitated by the fact that their emission is highly variable on different timescales, from flares that last minutes to days to several months in a high state of radiation. Also, it is easier to identify a point source in a transient search because of the lower background accumulated over the relatively short duration of the burst [83]. It is noteworthy that AMANDA detected three neutrino events in temporal coincidence with a rare orphan flare of blazar 1ES 1959+650 [84]. No attempt was made to evaluate a posteriori statistics for this event although its significance by any account exceeds that of the coincidences presently under discussion. Fig. 5.2 shows the coincident neutrinos in AMANDA .

In June 2015, blazar 3C 279 underwent an intense flare observed by Fermi LAT. The gamma-ray flux increased up to forty times over the steady flux and developed a relatively hard spectrum during the flare

[85]. An in-depth study of the data revealed an even higher photon flux and a harder spectral index [86]. An increase in X-ray emission was observed by SWIFT [87]. The event represents an extraordinary opportunity to investigate the pionic origin of the gamma rays by identifying temporally coincident cosmic neutrinos in IceCube. IceCube data is routinely subjected to a blind analysis. The data covering this event, and others discussed in this paper, have not been unblinded, which follows a yearly process.

Here, prospects of observing muon neutrinos in coincidence with flares of blazar 3C 279 has been investigated by calculating the number of neutrino events based on estimates previously developed in connection with the 2002 burst of blazar 1ES 1959+650. We also comment on a recent flare of this blazar. It should be noted that we focus on muon neutrinos, whose directions can be reconstructed with a resolution of 0.3°, allowing for statistically compelling coincidences that are unlikely to emerge with electron and tau neutrinos, which at present are only reconstructed to about 10°.

## 5.2 Neutrino flux from a pionic gamma-ray source

In the hadronic scenario, MeV-TeV gamma rays are produced from protons colliding with radiation or gas surrounding the object. These collisions generate charged and neutral pions which decay, producing high-energy gamma rays and neutrinos. Here, we follow estimates [88] that relate the neutrino flux to the observed gamma-ray flux using energy conservation:

$$\int_{E_\gamma^{\min}}^{E_\gamma^{\max}} E_\gamma \frac{dN_\gamma}{dE_\gamma} dE_\gamma = K \int_{E_\nu^{\min}}^{E_\nu^{\max}} E_\nu \frac{dN_\nu}{dE_\nu} dE_\nu, \tag{5.1}$$

where the factor $K = 1(4)$ for $pp(p\gamma)$ interactions. Considering multipion interaction channels, $K$ is changed to approximately 2 in the case of $p\gamma$ interactions. The proton spectrum, resulting from Fermi acceleration, as well as the accompanying photon and neutrino spectra are expected to follow a power law spectrum with $\alpha \approx 2$. However, the observed photon spectrum steepens because the gamma rays are absorbed by propagation in the EBL and, possibly, also in the source. Therefore, the observed gamma-ray spectrum is assumed to follow

$$\frac{dN_\gamma}{dE_\gamma} = A_\gamma E_\gamma^{-\alpha}, \tag{5.2}$$

with $\alpha > 2$. In contrast to the photons, the neutrino spectrum is not modified by absorption. Although one may propagate the observed gamma rays in the EBL to find the de-absorbed spectrum, it is in general not possible to match the neutrino spectrum to the gamma rays because of gamma rays cascading inside the source. However, energy is conserved in the process, and the total energy between neutrinos and photons can still be related. Even this will result in a lower limit on the neutrino flux because photons absorbed in the source are not accounted for in the left hand side of Eq. 5.1. On the other hand, we assume that all high energy photons originate from proton acceleration, neglecting an electromagnetic component that must contribute at some level. Using Eq. 5.1 and assuming $E_{\gamma,\mathrm{max}} \gg E_{\gamma,\mathrm{min}}$, we obtain the following neutrino spectrum:

$$\frac{dN_\nu}{dE_\nu} \approx A_\nu\, E_\nu^{-2} \approx \frac{A_\gamma E_{\gamma,\mathrm{min}}^{-\alpha+2}}{(\alpha-2)K\ln\left(E_{\nu,\mathrm{max}}/E_{\nu,\mathrm{min}}\right)}\, E_\nu^{-2}. \tag{5.3}$$

Here, $E_{\gamma,\mathrm{min}}$ is the minimum energy of photons reflecting the threshold energy of pion production in $pp$ interactions and for the production of the delta resonance in $p\gamma$ interactions. For $pp$ collisions, the minimum energy required for pion production is:

$$E_p^{\mathrm{min}} = \Gamma\,\frac{(2m_p+m_\pi)^2-2m_p^2}{2m_p} \simeq \Gamma\times 1.23\,\mathrm{GeV}, \tag{5.4}$$

where $\Gamma$ is the Lorentz factor of the jet relative to the observer. Given that three pions are produced and that, on average, each charged pion produces four leptons and each neutral pion two photons, the relation between proton energy and gamma-ray and neutrino energies is:

$$E_\gamma^{\mathrm{min}} = \frac{E_p^{\mathrm{min}}}{6},\;\; E_\nu^{\mathrm{min}} = \frac{E_p^{\mathrm{min}}}{12}. \tag{5.5}$$

For $p\gamma$ collisions, the energy threshold is set by the delta resonance $p\gamma \to \Delta \to \pi N$:

$$E_p^{\mathrm{min}} = \Gamma^2\,\frac{m_\Delta^2-m_p^2}{4E_\gamma^\circ} \simeq \Gamma^2\left(\frac{1\,\mathrm{MeV}}{E_\gamma^\circ}\right)\times 160\,\mathrm{GeV}, \tag{5.6}$$

where $E_\gamma^\circ$ is the target photon energy. In this case, the gamma-ray and neutrino energies are related to the proton energy by

$$E_\gamma^{\mathrm{min}} = \frac{E_p^{\mathrm{min}}\,x_{p\to\pi}}{2},\;\; E_\nu^{\mathrm{min}} = \frac{E_p^{\mathrm{min}}\,x_{p\to\pi}}{4}, \tag{5.7}$$

where $x_{p\to\pi} \simeq 0.2$ is the average fraction of proton's energy transferred to the pion.

## 5.3 Neutrinos in coincidence with 3C 279 Flares

Blazar 3C 279 is a flat spectrum radio quasar (FSRQ) located at declination $-5.8^\circ$ and right ascension $194^\circ$ with a redshift of 0.536. It is one of the brightest sources in the EGRET catalogue [89] and was the first FSRQ discovered at TeV energy by MAGIC in 2006 [90]. The MAGIC collaboration has reported a gamma-ray flux from 3C 279 of $5.2 \times 10^{-10}\,\mathrm{TeV}^{-1}\mathrm{cm}^{-2}\mathrm{s}^{-1}$ with a spectral index of 4.1. The EBL corrected spectrum has a smaller spectral index of 2.94.

Blazar 3C 279 has consistently exhibited rapid variations in flux, and multiple flares have been observed. On June 16, 2015, Fermi observed an intense flare of GeV gamma rays from 3C 279 reaching forty times the steady flux of this source. The spectral study of this flux found a relatively hard spectral index. Specifically, we will use in our estimates the average daily photon flux of $24.3 \times 10^{-6}\, ph\, cm^{-2}\, s^{-1}$ with a spectral index of 2.1. Fig. 5.3 shows the light curves of 3C 279 during this flare as observed by *Fermi*.

The expected number of well-reconstructed muon neutrinos in IceCube is calculated using Eq. 5.3 and

$$N_{\nu_\mu+\overline{\nu}_\mu} = t \int \frac{dN_\nu}{dE_\nu}\, A_{eff}(E,\theta)\, dE \tag{5.8}$$

where the effective area $A_{eff}$ is taken from [91]. The neutrino flux calculated from the energy balance relation of Eq. 5.1 depends on the value of $E_{\nu,\mathrm{max}}/E_{\nu,\mathrm{min}}$, which represents the energy interval over which proton interactions produce pionic gamma rays. We will consider three possible values for this ratio:

- Case 1: We assume that neutrinos are exclusively produced in a specific energy range. This is similar to the approach in reference [79] where the neutrino spectrum is assumed to peak at PeV energies. The number of events for various values of $E_{\nu,\mathrm{max}}/E_{\nu,\mathrm{min}}$ is shown in Fig. 5.4 for $pp$ and $p\gamma$ interactions. For $pp$ collisions, the number of neutrinos expected is within IceCube's sensitivity for the wide range of values for the Lorentz factor and the neutrino energy range considered. For $p\gamma$ collisions, large values of $E_\gamma^\circ/\Gamma^2$ are required for observing the flare in neutrinos. Note that for $p\gamma$ interactions we label the energy in terms of the ratio $E_\gamma^\circ/\Gamma^2$. The actual energy depends on the value of $\Gamma$ which is often not directly measured and must be obtained from further modeling of the spectrum [86, 92].

- Case 2: We assume that neutrinos are produced over the same energy range as the gamma rays, i.e., $E_{\nu,min}$ is obtained from Eq. 5.4(5.6) for $pp$ and $p\gamma$ collisions. The resulting number of neutrino events is shown in Fig. 5.5 for different values of maximum neutrino energy. Here, the estimated number of events strongly depends on the maximum energy achieved by the cosmic accelerator.

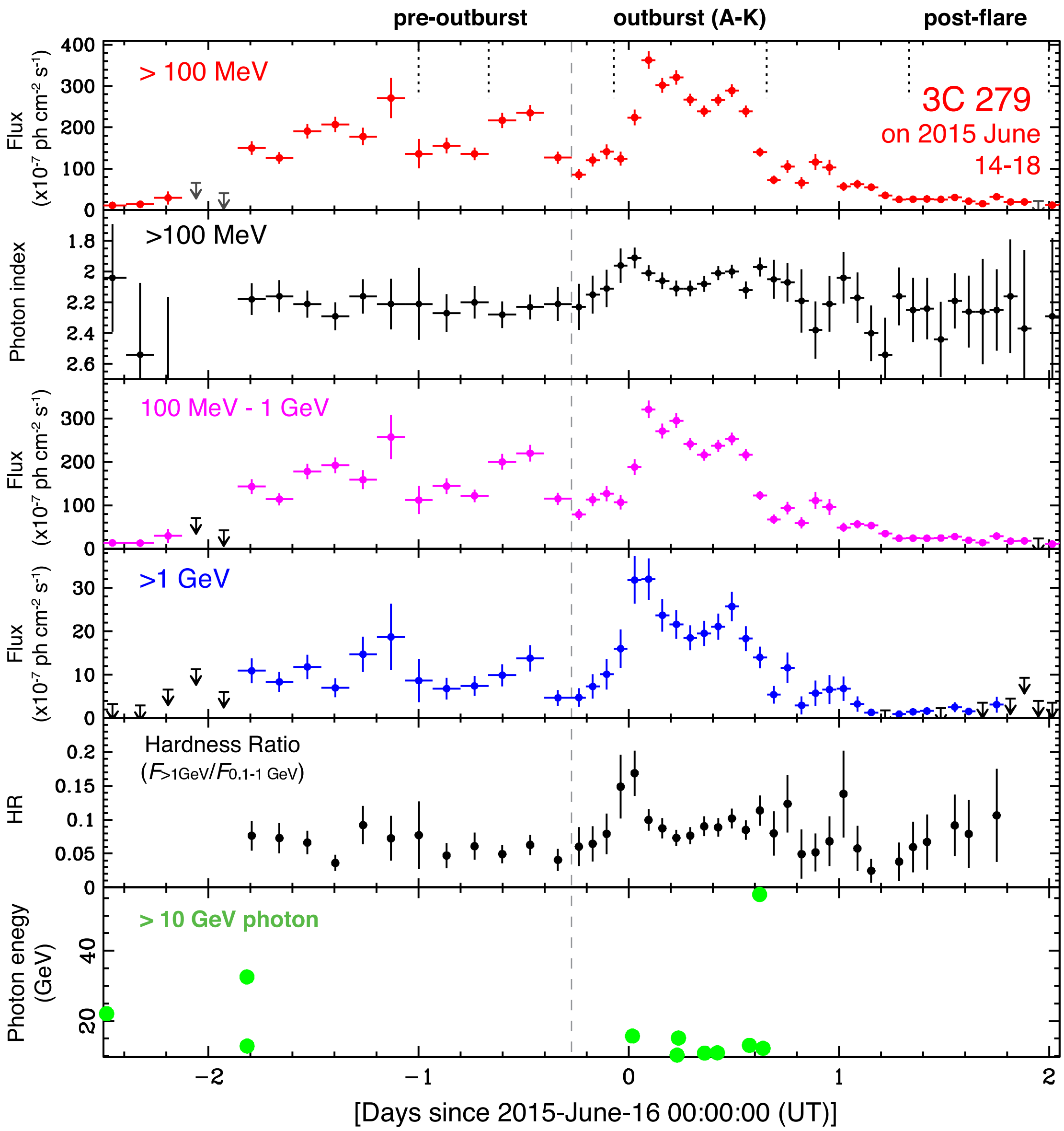


**Figure 5.3:** Light curves of 3C 279 in the $\gamma$ ray band as observed by Fermi-LAT [86]

- Case 3: Finally, we consider different threshold energies for neutrinos, assuming that the maximum neutrino energy is 10 PeV, the highest energy observed by IceCube so far. The results are shown in Fig. 5.6 for $pp$ and $p\gamma$ collisions. Notice that a higher minimum neutrino energy corresponds to a larger number of events observed.

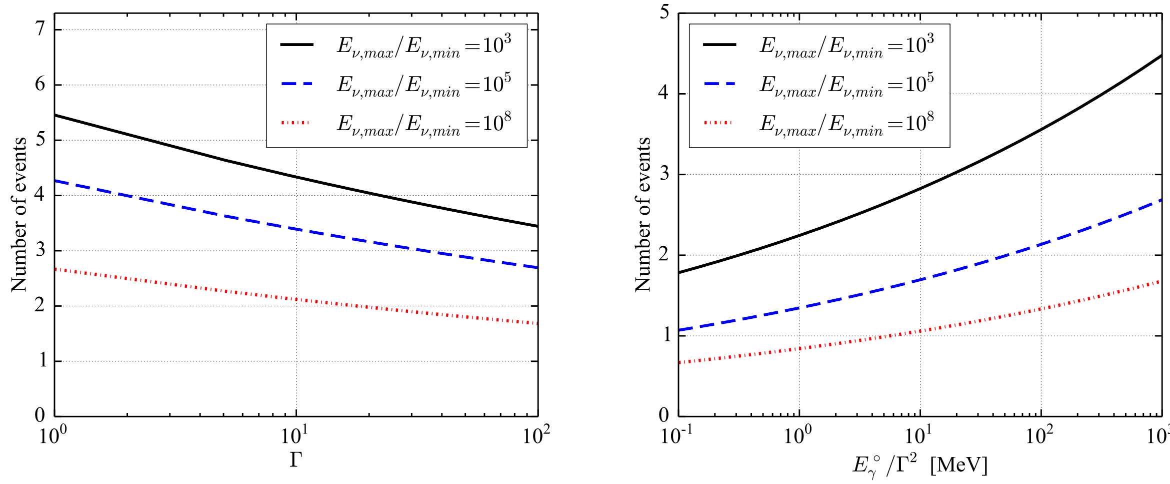


**Figure 5.4:** Estimated number of events from blazar 3C 279 flare in June 2015 for different energy ranges of neutrino emission from $pp$ (left) and $p\gamma$ (right) collision. The events correspond to neutrino energies above 1 TeV.

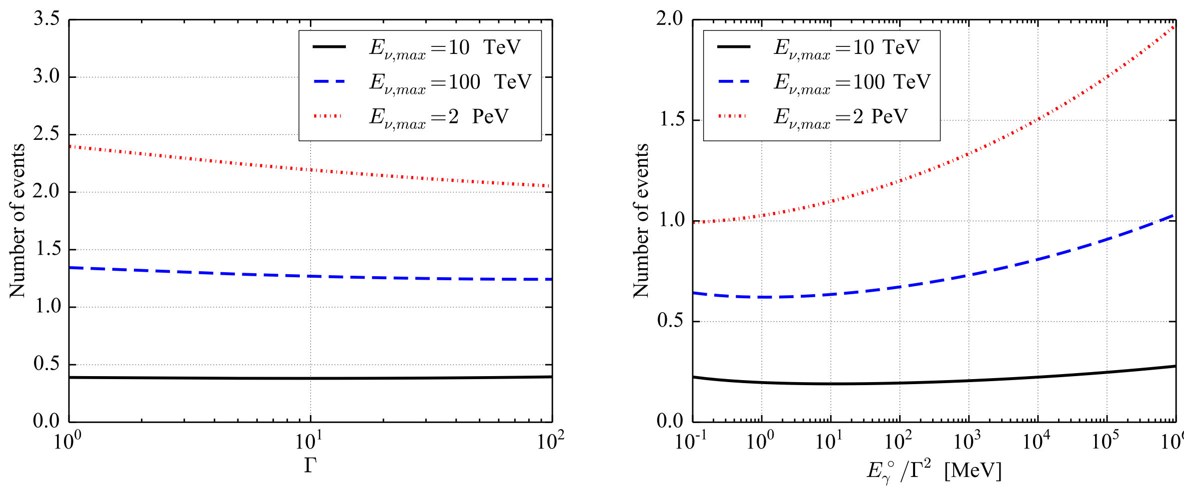


**Figure 5.5:** Estimated number of events from blazar 3C 279 flare in June 2015 for different values of maximum neutrino energy in $pp$ (left) and $p\gamma$ (right) collision when neutrinos and gamma rays are produced in the same energy range. The events correspond to neutrino energies above 1 TeV.

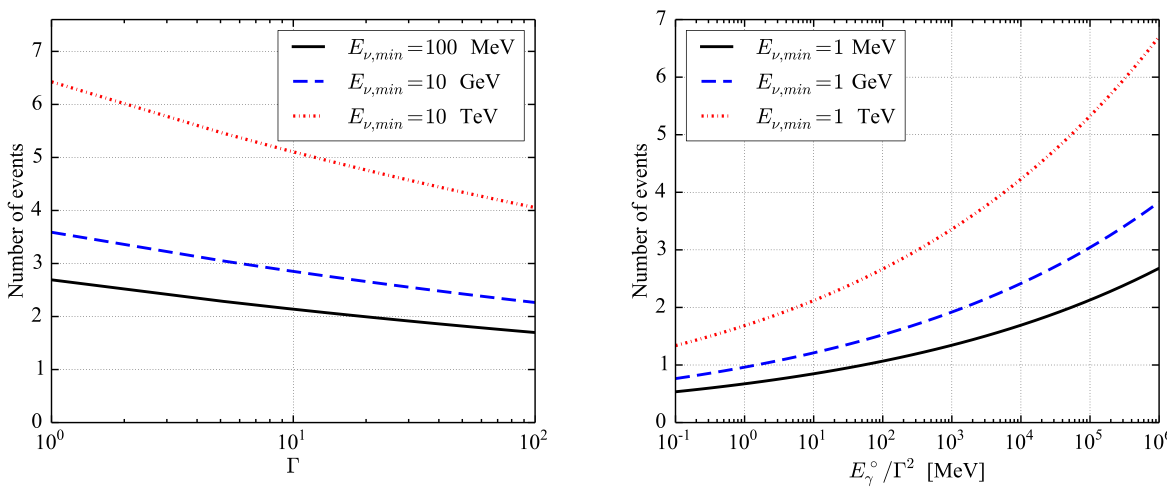


**Figure 5.6:** Estimated number of events from blazar 3C 279 flare in June 2015 for different minimum energy ranges of neutrinos in $pp$ (left) and $p\gamma$ (right) collision, assuming that the maximum neutrino energy is 10 PeV. The events correspond to neutrino energies above 1 TeV.

## 5.4 Summary

The above calculations illustrate that blazar flares represent an extraordinary opportunity to identify the origin of IceCube neutrinos. The short time window results in a lower number of events but also a suppressed background. For the specific burst of 3C 279, we have shown that there is a clear opportunity for observing coincident neutrinos, especially in the case of $pp$ interaction.

In addition to the intense flare in June 2015, two previous flares were observed during December 2013 and April 2014 [93]. Although their photon flux is not as large as for the flare discussed above, stacking them will result in a higher likelihood of finding neutrinos. The average daily photon flux of all three flares is listed in Table 5.1. Assuming, for simplicity, that the neutrino spectrum would follow the gamma-ray spectrum, the total number of events for a flat spectrum of neutrinos will be about 4(2) for $pp(p\gamma)$ collisions. We have

| Date | $F_\gamma\,[ph\,cm^{-2}s^{-1}]$ |
|---|---|
| December 20, 2013 | $6 \times 10^{-6}$ |
| April 3, 2014 | $6.4 \times 10^{-6}$ |
| June 16, 2015 | $24.3 \times 10^{-6}$ |

**Table 5.1:** The date and average daily photon flux of observed flares from 3C 279. All fluxes are measured above 100 MeV [93, 86].

also estimated the number of events for each flare using detailed information of fluxes and assuming same spectral behavior for neutrinos and gamma rays. Detailed duration and flux are listed in Table 5.2. The total number of events obtained is 4(2) for $pp(p\gamma)$ collisions. Statistics are straightforward with less than 0.001 background of atmospheric events per day within the resolution of 0.3°.

The FSRQ 3C 279 is included in the IceCube source list for both time-dependent [80] and time-independent point source searches [91]. The latest time-dependent search looked for a correlation of neutrinos with observed flares up until 2012. This period did not include any flares from 3C 279. Future time-dependent studies may reveal signals from these flares.

Recalling the temporal coincidence observed in AMANDA with flares of blazar 1ES 1959+650, it is noteworthy that a new very high energy flare from 1ES 1959+650 was observed by VERITAS during October 2015 [94]. According to the preliminary analysis of the data, the flux has reached $\sim 50\%$ of the Crab flux with a spectral index of 2.5. Detailed analysis will provide more information about the duration and spectrum of this flare. Based on the preliminary results, and provided that the gamma rays are hadronic in origin, IceCube expects to observe $\sim 0.1$ events per hour for this burst. If the burst has lasted for more than a day,

| Date | $F_\gamma \, [ph \, cm^{-2} s^{-1}]$ | $\alpha$ | Duration [day] |
|---|---|---|---|
| December 20, 2013 | $11.71 \times 10^{-6}$ | 1.71 | 0.2 |
| April 3, 2014 | $11.79 \times 10^{-6}$ | 2.16 | 0.267 |
| June 16, 2015 | $24.3 \times 10^{-6}$ | 2.1 | 1 |

**Table 5.2:** The date, photon flux, spectral index, and duration of observed flares from 3C 279. All fluxes are measured above 100 MeV [93, 86].

then it is very likely that accompanying neutrinos would be observed in IceCube. Its location is obscured by the earth, and the highest energy events will therefore be absorbed.

# Chapter 6

# Prospects for Detecting Galactic Sources of Cosmic Neutrinos with IceCube

## 6.1 Introduction

The position of the knee in the cosmic ray spectrum indicates that some sources accelerate cosmic rays to energies of several PeV. These PeVatrons therefore produce pionic gamma rays whose spectrum should extend to several hundred TeV. Like for gamma rays, the search for Galactic neutrino sources concentrates on the search for PeVatrons, supernova remnants with the required energetics to produce cosmic rays, at least up to the knee in the spectrum. Some may have been revealed primarily by the highest energy all-sky survey in $\sim$ 10 TeV gamma rays using the Milagro detector.

Although predominantly extragalactic, the present data cannot exclude a subdominant flux of Galactic origin in the IceCube data [95, 96, 97, 98]. Unidentified sources [99], Fermi bubbles [95, 100, 101], and Sagittarius A$^*$ [102] have been reviewed as potential Galactic sources. However, the general conclusion is that these sources can account for a fraction of the events detected. Specifically, the possibility that the hot spot close to the Galactic Center (GC) is produced by a single point source with a flux normalization of $6 \times 10^{-8}$ GeV cm$^{-2}$ s$^{-1}$ has been excluded [103, 104].

In a map of the northern Galactic plane obtained with Milagro data, six promising neutrino sources were identified in [105, 106]. The IceCube Collaboration has carried out extensive searches for point and extended sources, reporting evidence with a significance of 2.5 $\sigma$, when the six Milagro sources are considered together [91].

---

*This study has been published in* F. Halzen, A. Kheirandish, and V. Niro, Astropart. Phys., vol. 86, pp. 46-56, 2017.

In Ref. [104], the authors investigated the prospects for observing the three confirmed Milagro sources and re-evaluated the probability and constraints in light of the low-energy cut-off reported by the Milagro collaboration [107, 108]. They concluded that more than 10 years of running IceCube is necessary to yield a discovery at the level of $3\sigma$. In the case of the source MGRO J1908+06, evidence at $3\sigma$ could be obtained in seven years assuming values of the spectral index and the cut-off energy that are in good agreement with the best fit reported in [107].

Here, we update the predictions using the observation and flux measurements reported by HAWC, ARGO-YBJ, and air Cherenkov telescopes (ACT) VERITAS and HESS. Most importantly, with a detector superior to Milagro, the HAWC experiment has confirmed only four of the six sources [109, 110]: MGRO J1908+06, MGRO J1852+01, MGRO J2031+41, and MGRO J2019+37. Fig. 6.1 shows HAWC's observation of these sources. For these, we will construct a gamma ray spectrum based on all information available and evaluate the neutrino flux. Subsequently, we will compute the number of signal and background events as well as the p-value for observing the sources as a function of time. Finally, we will determine exclusion limits on a flux of hadronic origin in the absence of an observation. The main results can be summarized as follows:

- MGRO J1908+06: Although historically classified as a pulsar wind nebula (PWN) and currently as an unidentified source, its large size and hard spectrum in TeV photons suggest that it may be a supernova remnant (SNR). SNRs are suspected to be the sources of the highest energy cosmic rays in the Galaxy. We re-evaluate the probability of observing the source using the flux reported by HESS and anticipate a $3\sigma$ observation in about 10 years of IceCube data. However, the answer depends on the actual threshold of the specific analysis. By increasing the energy threshold, IceCube has the potential to observe MGRO J1908+06 at the some statistical level with only six years of data. A lack of observation in 15 years of IceCube data will indicate that MGRO J1908+06 is not a cosmic-ray accelerator.

- MGRO J1852+01: In the original Milagro map of the TeV sky, this source missed the statistical threshold for candidate sources. It has now been conclusively observed by HAWC and is a potential neutrino source considering its relatively large flux. Since the proper study of spectrum and extension of the source have not been performed by HAWC, we have studied the neutrino flux under different assumptions for the source's extension and spectrum. We find that IceCube should see this source in 5 years of data provided that the source is not extended. However, if the source is extended, 15 years is required to reach a significant level of observation.

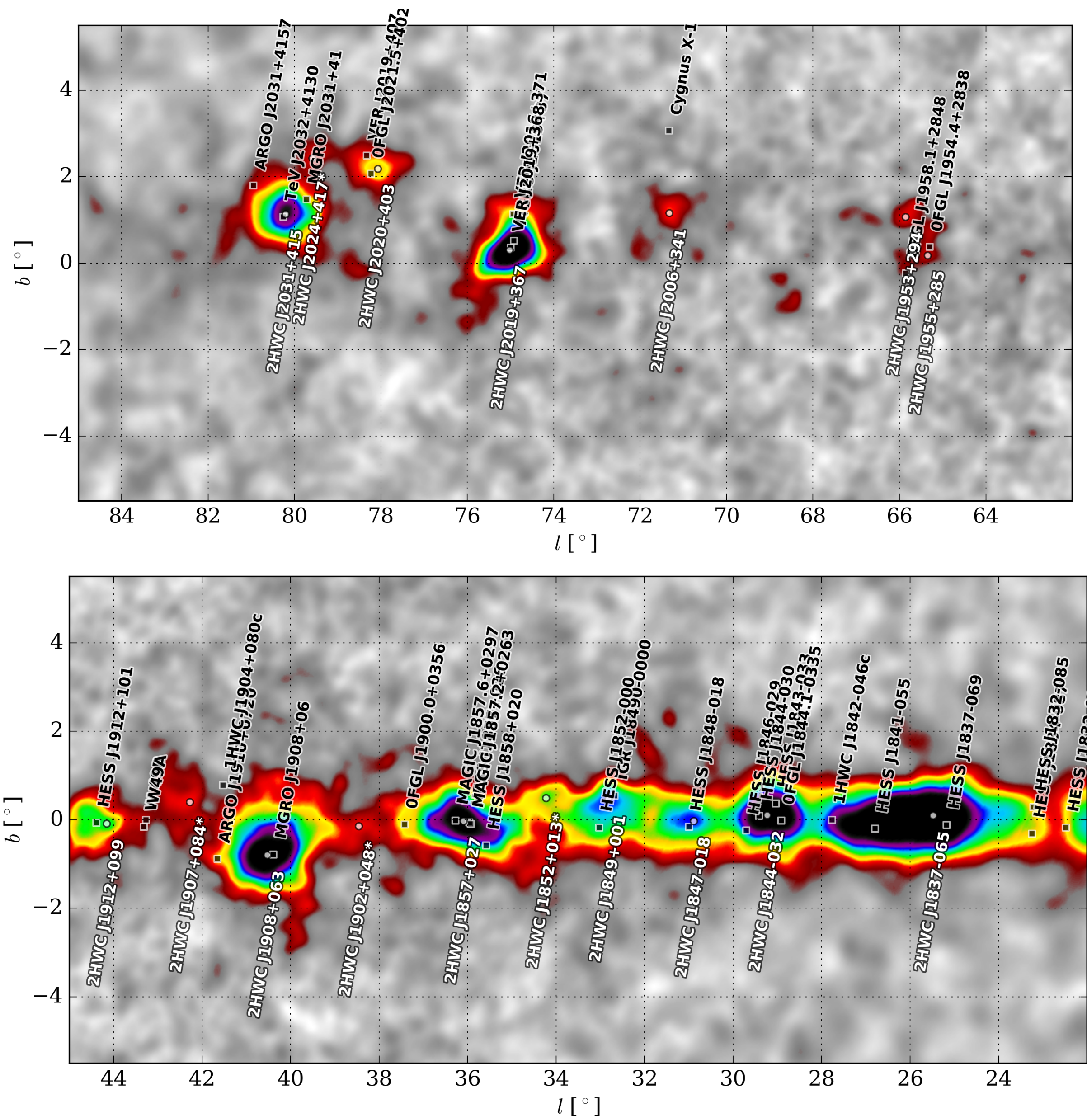


**Figure 6.1:** Up: HAWC observation of Cygnus region of the Galaxy. MGRO J2031+41 and MGRO 2019+37 are located in this region. Bottom: HAWC observation of inner Galaxy. HAWC observes the known source MGRO 1908+06 and confirms MGRO J1852+06 [111] which was found under significance thresold in Milagro.

- MGRO J2031+41: Due to the uncertainties associated with the origin of the flux of the Cygnus cocoon and $\gamma$-Cygni, a complete picture of this source is missing. Its extension and other TeV emissions in its vicinity have made it difficult for ACT experiments like VERITAS to measure the TeV flux from this source. Although previous studies indicated that observing the source would be challenging [104], using recent ARGO-YBJ and Fermi data, we argue that neutrino observations at the level of $3\sigma$ may be possible in 10 years of IceCube data.

- MGRO J2019+37: We present an update on the neutrino observation from this source based on the spectrum measured by VERITAS, which has provided up to now the most precise measurement for the spectrum of the source up to 30 TeV. We show that IceCube is likely to observe the source in 15 years. This source is currently classified as a PWN. Thus, the detection of neutrinos from this region could point towards the production mechanism of neutrinos in a PWN as described in [112].

## 6.2 Milagro sources

After confirmation by HAWC [109, 110], the Milagro sources that we consider in this analysis are, as mentioned above, MGRO J1908+06, MGRO J1852+01, MGRO J2031+41, and MGRO J2019+37. In this section, we summarize the experimental information on these sources.

**MGRO J1908+06:** The source MGRO J1908+06 has been detected by large-acceptance air-shower detectors (EAS) like the Milagro experiment, see Refs. [113, 114, 108], and the ARGO-YBJ experiment [115]. This source has been detected also by ACTs, like HESS [116], which finds a spectrum with no evidence of a cut-off for energies $< 20$ TeV. The HESS detector reports a flux systematically lower than the Milagro and ARGO-YBJ data. With better angular resolution, it could be that HESS detects the flux from a point source that is not resolved by the Milagro and ARGO-YBJ observation. MGRO J1908+06 has also been recently detected by VERITAS [117], and the flux reported is of the same order as the one measured by HESS. Also, the value recently reported by HAWC points towards a similar normalization [109].

We report in Table 6.1 the extension for MGRO J1908+06 observed by HESS, VERITAS, and ARGO-YBJ, while in Table 6.2 we report the flux measured by HESS and VERITAS. In Fig. 6.3, we have compiled the spectra for MGRO J1908+06 from the different experiments.

Finally, note that Fermi-LAT observes the pulsar PSR J1907+0602 within the extension of the Milagro source MGRO J1908+06 [118]. On the other hand, the large size and hard spectrum in TeV photons of MGRO J1908+06 are not characterstic of a PWN and perhaps consistent with a SNR. SNRs are suspected to be the sources of the highest energy cosmic rays in the Galaxy [119], see also [120, 121].

**MGRO J1852+01:** In the original Milagro survey, its statistical significance fell just below the statistical threshold to be a candidate source. With its recent observation by HAWC [110] MGRO J1852+01 becomes a plausible neutrino source candidate. The primary study of the six Milagro sources [105] suggested that this source, due to its large flux, could considerably increase the probability of detecting neutrinos in IceCube in five years. The flux from a $3 \times 3$ degree region around MGRO J1852+01 is given by $dN/dE = (5.7 \pm 1.5_{stat} \pm 1.9_{sys}) \times 10^{-14}$ TeV$^{-1}$ cm$^{-2}$ s$^{-1}$ at the median detected energy of 12 TeV, assuming a differential source spectrum of $E^{-2.6}$ [122]. In Table 6.1 and Table 6.2, the information on this source is summarized, while in Fig. 6.5 we show the best-fit spectrum from the Milagro collaboration.

**MGRO J2031+41:** The flux from MGRO J2031+41 has been measured by Milagro [113, 114, 107]; the measurement cannot distinguish between a power law and a power law with cut-off. This is also the case for the ARGO-YBJ observations [123]. The two experiments have comparable angular resolution. The flux measured by ARGO-YBJ [123] for this source is compatible with the one reported by Milagro, which extends to energy below 1 TeV.

In general, ACT experiments report much smaller fluxes for this source. Indeed, measurements by MAGIC [124], HEGRA [125], and Whipple [126] can account for just a few percent of the Milagro flux. The source has been recently studied by the VERITAS collaboration, which has reported a flux comparable to the one reported by MAGIC. In the current picture [127], there are several sources contributing to the emission of MGRO J2031+41: the cocoon, the $\gamma$-Cygni SNR, VER J2019+407, and TeV J2032+4130. The latter has been detected by both VERITAS and MAGIC. In conclusion, a complete picture and understanding of this source is still not given. New data have been presented by the ARGO-YBJ detector [128], which suggests identifying ARGO J2031+4157 as the TeV-energy counterpart of the Cygnus cocoon. For this reason, they report the best fit not only considering the ARGO-YBJ data but also including in their fit the Fermi-LAT data from the Cygnus cocoon. This results in a harder spectral index with significant consequences for the neutrino prediction. Since leptonic processes could contribute to the cocoon emission at

| Source | Type | $\sigma_{\rm ext}$ (ACT) | $\sigma_{\rm ext}$ (EAS) |
|---|---|---|---|
| MGRO J1908+06 | UNID | | |
| $\hookrightarrow$ ARGO-YBJ | | | $0.49^\circ \pm 0.22^\circ$ [123] |
| $\hookrightarrow$ HESS J1908+063 | | $0.34^\circ\ ^{+0.04}_{-0.03}$ [116] | |
| $\hookrightarrow$ VERITAS | | $0.44^\circ \pm 0.02^\circ$ [117] | |
| MGRO J1852+01 | UNID | | Milagro: $3^\circ \times 3^\circ$ search region [122] |
| MGRO J2031+41 | UNID | | |
| $\hookrightarrow$ ARGO J2031+4157 | | | $1.8^\circ \pm 0.5^\circ$ [128] |
| MGRO J2019+37 | PWN | | Milagro: $0.7^\circ$ [107] |
| $\hookrightarrow$ VER J2019+368 | | $\sim 0.35^\circ$ [130] | |

**Table 6.1:** Extensions of the sources as reported by different experiments. For the source MGRO J2031+41, we do not report the extension of the corresponding sources detected by ACT experiments, since the flux of these sources is much smaller than the one reported by the Milagro collaboration, see text for details. Note that the four sources have been recently detected by HAWC [109, 110].

the energies detected by Fermi-LAT, we might expect the purely hadronic component of MGRO J2031+41 to lie somewhere between the two fits obtained by the ARGO-YBJ collaboration. We report in Table 6.1 the extension of MGRO J2031+41 as given by the ARGO-YBJ experiment, while in Table 6.2 we show the fluxes obtained with and without the inclusion of the Fermi-LAT data in the fit. In Fig. 6.7, we report the spectra for MGRO J2031+41 from different experiments. Note that we do not report the measurements by HEGRA [125] and Whipple [126], but these are in agreement with the MAGIC results.

**MGRO J2019+37:** The flux of the source MGRO J2019+37 has been measured by Milagro, see [113, 114, 107], reporting a power-law with energy cut-off as best fit. This source has not been detected by the ARGO-YBJ detector, which instead set 90% C.L. upper bounds on the flux [123]. Additionally, a limit on the flux at 115 TeV has been inferred through the CASA-MIA experiment [129].

The Milagro source MGRO J2019+37 has been recently detected by VERITAS. VERITAS collaboration reported two sources in the region of MGRO J2019+37: the faint point-like source VER J2016+371 and the bright extended source VER J2019+368 [130]. This second source is likely to account for the bulk of the Milagro emission. The VERITAS collaboration reported a very low spectral index for this source on the order of 1.75, between 1–30 TeV. We list in Table 6.1 the extension for MGRO J2019+37 as given by VERITAS and the Milagro 2012 release, and in Table 6.2 the value of the flux reported by the VERITAS experiment. In Fig. 6.8, we show the data for MGRO J2019+37 from different experiments.

| Source | $E_\gamma^{\rm norm}$; $dN_\gamma^{12}/dE_\gamma$ at $E_\gamma^{\rm norm}$; $\alpha_\gamma$ (ACT or EAS) |
|---|---|
| MGRO J1908+06 | |
| $\hookrightarrow$ HESS J1908+063 | 1 TeV; $4.14 \pm 0.32_{stat} \pm 0.83_{sys}$; $2.10 \pm 0.07_{stat} \pm 0.2_{sys}$ [116] |
| $\hookrightarrow$ VERITAS | 1 TeV; $4.23 \pm 0.41_{stat} \pm 0.85_{sys}$; $2.20 \pm 0.10_{stat} \pm 0.20_{sys}$ [117] |
| MGRO J1852+01 | |
| $\hookrightarrow$ Milagro | 12 TeV; $(5.7 \pm 1.5_{stat} \pm 1.9_{sys}) \times 10^{-2}$; 2.6 [122] |
| MGRO J2031+41 | |
| $\hookrightarrow$ ARGO J2031+4157 | w/o Fermi-LAT: |
| | 1 TeV; $(2.5 \pm 0.4) \times 10$; $2.6 \pm 0.3$ [128] |
| | w Fermi-LAT: |
| | 0.1 TeV; $(3.5 \pm 0.3) \times 10^3$; $2.16 \pm 0.04$ [128] |
| MGRO J2019+37 | |
| $\hookrightarrow$ VER J2019+368 | 5 TeV; $(8.1 \pm 0.7_{stat} \pm 1.6_{sys}) \times 10^{-2}$; $1.75 \pm 0.08_{stat} \pm 0.2_{sys}$ [130] |

**Table 6.2:** Flux in units of $10^{-12}$ TeV$^{-1}$ cm$^{-2}$ s$^{-1}$ at a specific energy $E_\gamma^{\rm norm}$ and spectral index $\alpha_\gamma$ as recently reported by ACT or EAS experiments.

## 6.3 Gamma rays and neutrino flux

Perfoming a fit to the the gamma-ray flux using the parametrization

$$\frac{dN_\gamma(E_\gamma)}{dE_\gamma} = k_\gamma \left(\frac{E_\gamma}{\rm TeV}\right)^{-\alpha_\gamma} \exp\left(-\sqrt{\frac{E_\gamma}{E_{cut,\gamma}}}\right) , \tag{6.1}$$

the neutrino fluxes at Earth can be described by the following expression [131, 132]:

$$\frac{dN_{\nu_\mu+\bar\nu_\mu}(E_\nu)}{dE_\nu} = k_\nu \left(\frac{E_\nu}{\rm TeV}\right)^{-\alpha_\nu} \exp\left(-\sqrt{\frac{E_\nu}{E_{cut,\nu}}}\right) , \tag{6.2}$$

where

$$\begin{aligned} k_\nu &= (0.694 - 0.16\alpha_\gamma)k_\gamma \, , \\ \alpha_\nu &= \alpha_\gamma \, , \\ E_{cut,\nu} &= 0.59 E_{cut,\gamma} \, . \end{aligned} \tag{6.3}$$

The number of throughgoing muon neutrinos from a source at zenith angle $\theta_Z$ is given by Ref. [105]:

$$N_{ev} = t \int_{E_\nu^{\rm th}} dE_\nu \, \frac{dN_\nu(E_\nu)}{dE_\nu} \times A_\nu^{\rm eff}(E_\nu, \theta_Z) \, , \tag{6.4}$$

where we have summed over neutrino and antineutrino contributions. We will use the IceCube neutrino effective area reported in Ref. [91]. The effective area for the location of each source is shown in Fig. 7.4.

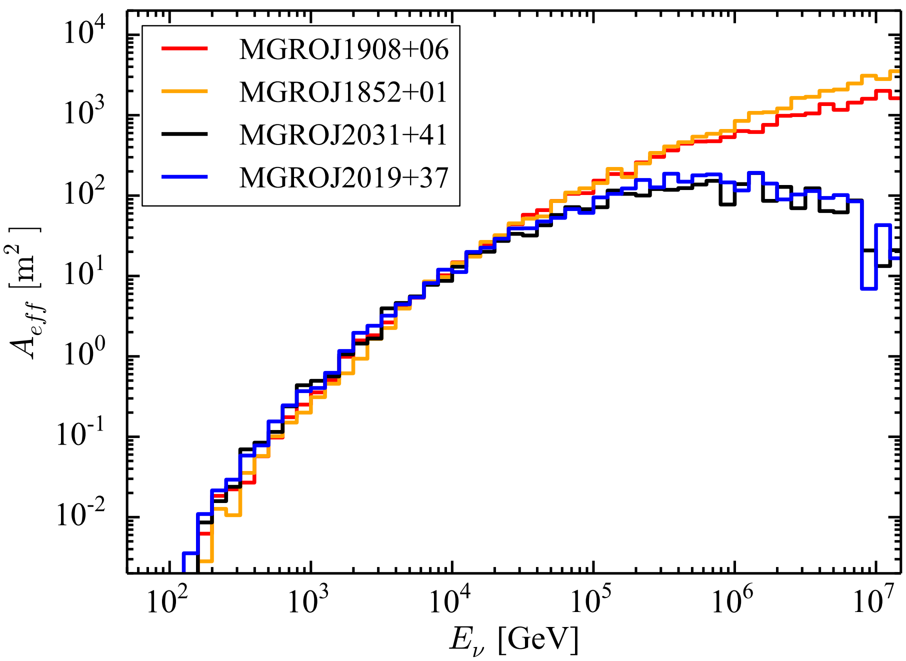


**Figure 6.2:** IC86 neutrino effective area as function of energy in the direction of each source considered in this study.

## 6.4 Results

Based on the updated information from gamma-ray experiments described in the previous section, we revisit the prospects for observing neutrinos from these sources with IceCube, using the effective area for the 86-string detector configuration [91]. This study updates a previous study of three of the sources [104] using Milagro [107, 108] and ARGO-YJB (2012) measurements [123]. For related studies of the neutrino emission from Milagro sources, see also Refs. [129, 105, 133, 134, 135, 136, 137].

The new information from gamma-ray experiments turns out to be important for a better parametrization of the flux of the gamma-ray sources. The uncertainties in the normalization and spectrum of the sources can result in important variations in the prediction of the neutrino fluxes. In this context, using updated data is important to make more reliable predictions and more appropriate interpretations of potential IceCube observations.

After calculating the neutrino flux, we compute the number of through-going muon neutrinos in IceCube. These have been produced inside or below the detector by neutrinos that have traversed the Earth. Any background of cosmic ray muons has thus been filtered out and only atmospheric neutrinos remain as a background for the northern hemisphere sources in a detector located at the South Pole. For each source, we fix the flux normalization to the best-fit values listed in Table 6.2. The expected number of muon neutrinos per energy bin are shown in Figs. 6.3, 6.5, 6.7 and 6.8 for the four sources considered in the analysis. For MGRO J1908+06, we have fixed $\alpha_\gamma = 2$, consistent with the value reported by HESS, and we have varied the cut-off energy from 30 TeV up to 800 TeV. For MGRO J1852+01, besides assuming $\alpha_\gamma = 2$, we have also considered $\alpha_\gamma = 2.6$ because this is the spectrum assumed by the Milagro collaboration. For MGRO J2031+41, we have considered the best-fit values for $\alpha_\gamma$ provided by the ARGO-YBJ collaboration, considering also the case in which the Fermi-LAT data have been added to the fit. Finally, for MGRO J2019+37 we have considered the case of $\alpha_\gamma \sim 1.75$, the best-fit value reported by the VERITAS collaboration.

To calculate the number of background atmospheric neutrino events, we have integrated the atmospheric flux [138] over an opening angle $\Omega = \pi(1.6\sigma_{\rm eff})^2$ around the direction of the source, where the angle $\sigma_{\rm eff} = \sqrt{\sigma^2_{\rm ext} + \sigma^2_{\rm IC}}$. The angular resolution of the IceCube detector is about 0.4° at the energies relevant for this analysis [31]. This solid angle correspond to a solid angle that contains roughly 72% of the signal events from the source; see also Ref. [139] for a discussion.

We have subsequently estimated the statistical significance for observing the sources using the analytic expression [140]:

$$p_{\rm value} = \frac{1}{2}\left[1 - {\rm erf}\left(\sqrt{q_0^{obs}/2}\right)\right] , \tag{6.5}$$

where $q_0^{obs}$ is defined as

$$q_0^{obs} \equiv -2\ln \mathcal{L}_{b,D} = 2\left(Y_b - N_D + N_D \ln\left(\frac{N_D}{Y_b}\right)\right) . \tag{6.6}$$

Here, $Y_b$ is the theoretical expectation for the background hypothesis, while $N_D$ is the estimated signal generated as the median of events Poisson-distributed around the signal plus background. We have considered the total number of events (not binned in energy) to have a closer prediction to what is done in the IceCube point-source searches [91].

In Fig. 6.4, we show the results for MGRO J1908+06. For this source, recent ACT data have reported a spectral index $\alpha_\gamma$ that is compatible with $\sim 2$. Despite the fact that the ACTs' normalization is smaller than the one previously reported by Milagro, the hard spectral index makes the source an interesting candidate for neutrino detection. For this reason, we also estimated how the p-value depends on the threshold energy that can be reached in a realistic analysis. We find that a $3\sigma$ discovery is possible in six years, if an energy threshold of about 5 TeV can be reached in the analysis, and that the spectrum extends to $E_{\mathrm{cut},\gamma}$ of 800 TeV. For the more conservative case that $E_{\mathrm{cut},\gamma} \sim 300$ TeV, as expected for galactic sources able to explain the cosmic-ray spectrum up to the knee, then an energy threshold of about 10 TeV would be required. Obtaining a $3\sigma$ discovery at a specific energy threshold will indicate a particular value of the cut-off energy $E_{\mathrm{cut},\gamma}$.

In Fig. 6.6, we show the statistical significance for MGRO J1852+01. For this source, due to the lack of data, not only is the spectral index poorly known but also the morphology of the source, whether extended or point-like, is uncertain. For the point-like hypothesis, a $3\sigma$ discovery can be reached in six years, independently of the energy cut-off $E_{\mathrm{cut},\gamma}$ and spectral index $\alpha_\gamma$ of the source, while more than 10 years are required if the source is extended.

In Fig. 6.7, we show the p-value for MGRO J2031+41. As explained in detail in the previous section, the origin of the gamma-ray emission from this source is not understood. Using the best fit obtained by the ARGO-YBJ collaboration in conjunction with the Fermi-LAT data, we find that a $3\sigma$ discovery is possible with 10 years of IceCube data. If this is indeed realized, the IceCube data not only would point towards a hadronic emission at TeV energies for MGRO J2031+41 but would help clarify the origin of the gamma-ray emission from the cocoon.

In Fig. 6.8, we show the statistical significance for MGRO J2019+37. A detection of neutrinos from this source would be extremely interesting since it might point towards the mechanism described in Ref. [112] for neutrino production in PWNs. For this source, we expect to obtain a $3\sigma$ discovery in roughly 15 years. Future data from HAWC on the spectrum of this source are important to confirm the hard spectral index, on the order of $\alpha_\gamma \sim 1.75$, reported by the VERITAS collaboration.

The Milagro collaboration has presented results on the energy spectrum of these sources obtained by unfolding of the data [107]. It is obviously important for other experiments to confirm the presence of a low-energy cut-off that they consistently find in the analysis of every source. In this context, the constraints that IceCube can set in the plane ($\alpha_\gamma$,$E_{cut,\gamma}$) with future data are important and complementary. We have therefore estimated the constraints set on $\alpha_\gamma$ and $E_{\mathrm{cut},\gamma}$ in the absence of a signal after 15 years of exposure with the complete 86-string IceCube detector. We have integrated the number of events from 1 TeV to 1 PeV in neutrino energy $E_\nu$ and defined the confidence level, C.L., as in Refs. [141, 142, 140, 143]:

$$C.L. = \frac{P_{(s+b)}}{1 - P_b}\,. \tag{6.7}$$

with $P_{(s+b)}$ and $P_b$ the p-values for the signal plus background and background-only hypothesis of the data, respectively; see [104] for details.

The results for the expected C.L. are presented in Fig. 6.9 for the four sources considered here for a running time of $t$=15 years. We have fixed the normalization to the best fit reported in Table 6.2, while we have varied the values of the spectral index $\alpha_\gamma$ and the cut-off energy $E_{cut,\gamma}$. As shown in the figure, for MGRO J1908+06, IceCube is able to constrain a major part of the values for $\alpha_\gamma$ reported by the HESS detector. In particular, for a spectral index as hard as $\alpha_\gamma \sim 2$, values of $E_{\rm cut,\gamma}$ greater than 100 TeV could be excluded at 95% C.L. For MGRO J1852+01, IceCube will exclude all the parameter space with $E_{\rm cut,\gamma}$ greater than 30 TeV at 95% C.L. For the source MGRO J2031+41, the allowed region of $\alpha_\gamma$ obtained considering ARGO-YBJ plus Fermi-LAT data will be excluded at 99% C.L., independently of the value of $E_{\rm cut,\gamma}$. Finally, for MGRO J2019+37, considering the standard value of $E_{\rm cut,\gamma}$ of 300 TeV, hard values of the spectral index with $\alpha_\gamma < 2$ will be excluded at 95% C.L.

As mentioned above, the Milagro collaboration has reported a low-energy cut-off in the spectra of the sources MGRO J1908+06, MGRO J2031+41 and MGRO J2019+37 [107, 108]. In this case, the combinations of $\alpha_\gamma$ and $E_{cut,\gamma}$ that could be excluded at 95-99 % C.L. using future IceCube data are important because they can independently probe the presence of a low-energy cut-off.

## 6.5 Conclusions

The highest energy survey of the Galactic plane has been performed by Milagro. This survey has identified bright sources in the nearby Cygnus star-forming region and in the inner part the Galaxy. Initially, the sources showed the expected behavior of PeVatrons. PeVatrons are the sources of cosmic rays in the "knee" region of the cosmic-ray spectrum that are expected to be sources of pionic gamma rays whose spectrum extends to several hundreds of TeV without a cut-off. Gamma rays from the decay of neutral pions are inevitably accompanied by neutrinos with a flux that is calculable.

Here, we re-evaluated the probability of observing four promising Milagro sources in IceCube. We used the updated information from air-Cherenkov and air-shower array experiments to estimate the flux of neutrinos. The prospects for observing these sources in IceCube is highly entangled with discrepancies in the detailed fluxes and morphologies measured by different experiments. Moreover, the uncertainty of the nature of these sources makes it more difficult to understand the observed spectrum. Different spectra and morphology of the sources correspond to different production mechanisms.

It should be noted that the discrepancy between measurements may arise from the difference in angular resolution between air-shower arrays and air-Cherenkov telescopes as well as from the range of energies in which they operate. Future results from HAWC will help resolve these discrepancies and reveal more information about the sources.

If the gamma rays are hadronic in origin, observation of an accompanying neutrino flux is likely over the lifetime of the IceCube experiment. Evidence from IceCube of neutrinos associated with these sources will greatly help in unraveling the nature of the sources.

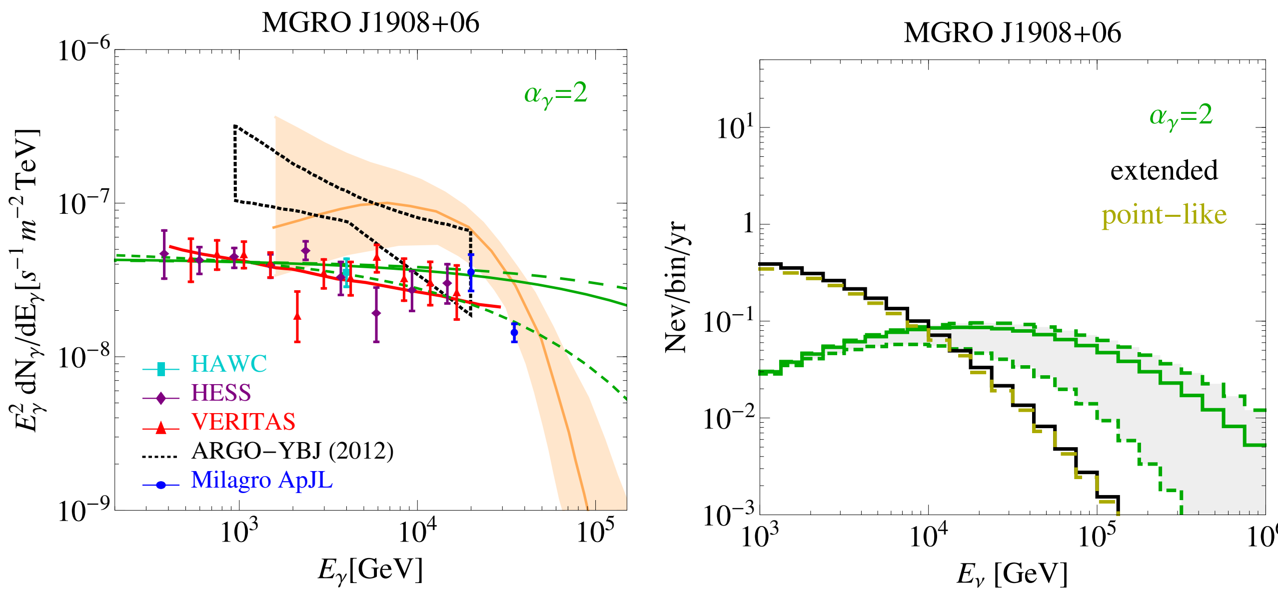


**Figure 6.3:** Left panel: We show in purple the data by HESS [116], in red the one from VERITAS [130], and in cyan the one from HAWC [109]. In blue we show the previous flux measurements by Milagro [113, 114], while the solid orange line and the shaded orange area show the best fit and the $1\sigma$ band as reported in Ref. [108] by Milagro. The dotted area is the ARGO-YBJ $1\sigma$ band [115]. With green lines we show the spectra obtained considering $\alpha_\gamma = 2$ and fixing the normalization to the best fit reported in Table 6.2, where we also allowed the cut-off energy to vary: $E_{\mathrm{cut},\gamma} = 30,\ 300, \textit{and}$ 800 TeV (short-dashed, solid, and long-dashed lines, in green). Right panel: We show the corresponding number of events for these spectra. The gray band encodes the uncertainty on the cut-off energy. With the black (gold dashed) line, we show the background from atmospheric neutrinos for extended (point-like) sources.

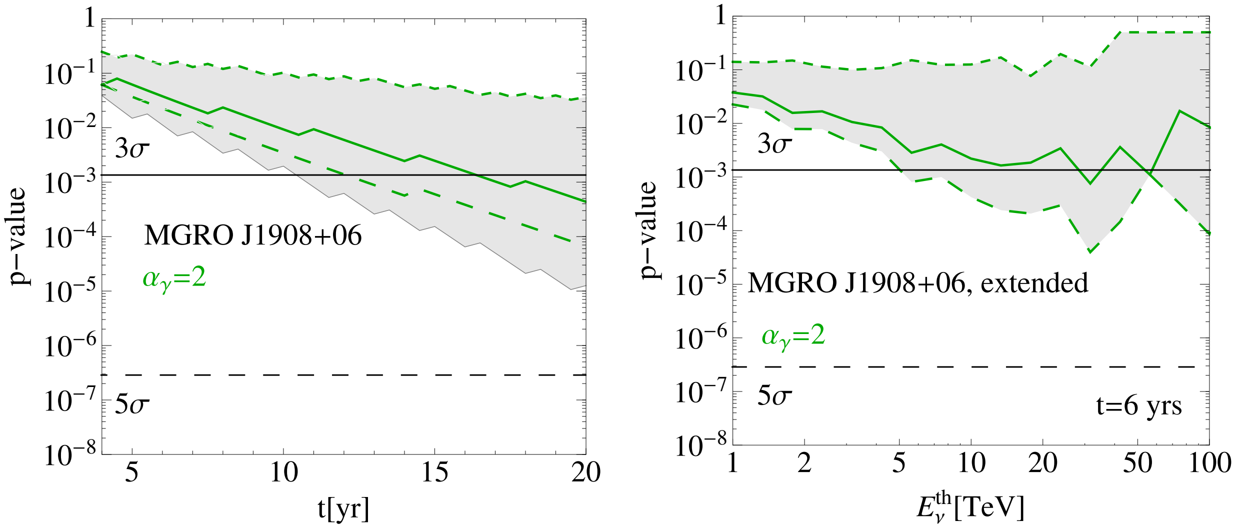


**Figure 6.4:** Left panel: p-values as a function of time, from 4 years to 20 years. The spectra have been fixed, as shown in Fig. 6.3. The gray band encodes the uncertainty due to different values of $E_{cut,\gamma}$, and morphology, see Table. **??**. For the green lines we have considered the case of extended source. Right panel: Dependence of the p-value on the energy threshold $E_\nu^{th}$.

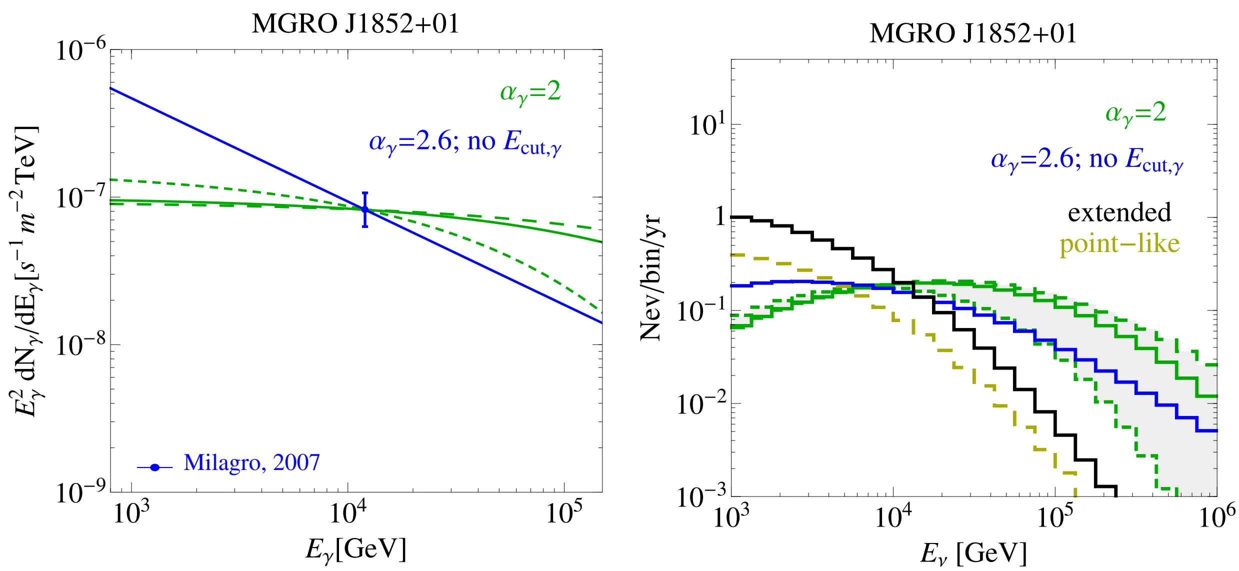


**Figure 6.5:** Left panel: We show in blue the value on the flux reported by the Milagro collaboration [122], which assumed an $E^{-2.6}$ spectrum. With green lines we show the spectra obtained considering $\alpha_\gamma = 2$ and fixing the normalization to the best fit reported in Table 6.2, where we also allowed the cut-off energy to vary: $E_{\mathrm{cut},\gamma} = 30,\ 300, and\ 800$ TeV (short-dashed, solid, and long-dashed lines, in green). Right panel: Number of events for the spectra reported with green and blue lines in the left panel. The gray band encodes the uncertainty on the cut-off energy. With the black (gold dashed) line, we show the background from atmospheric neutrinos for extended (point-like) sources.

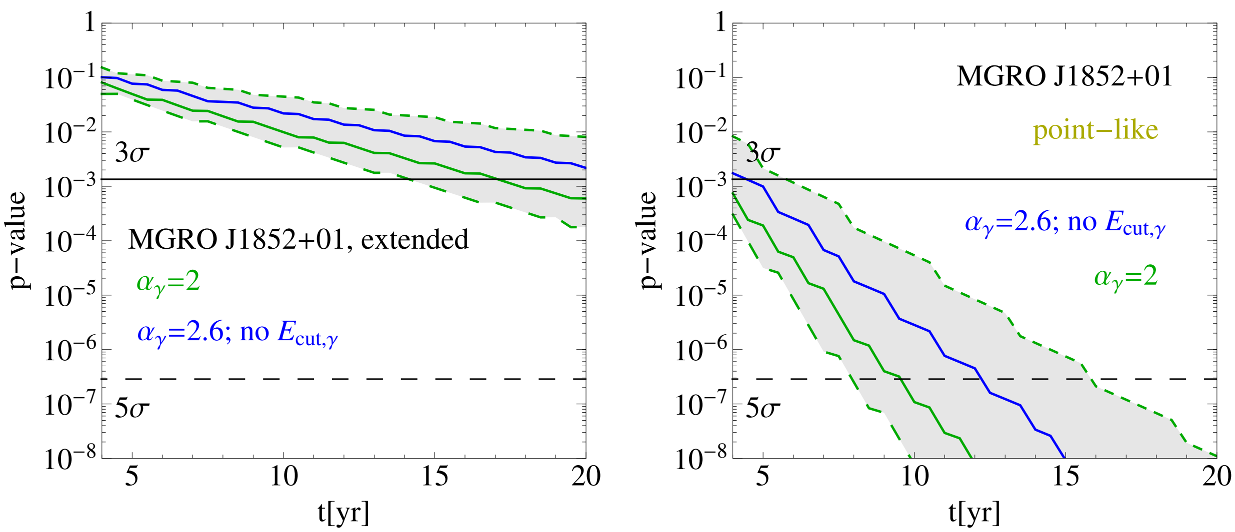


**Figure 6.6:** Left panel: p-values as a function of time, from 4 years to 20 years. The spectra have been fixed, as shown in Fig. 6.5. The gray band encodes the uncertainty due to different values of $E_{cut,\gamma}$. We assume the source to be extended. Right panel: We assume the source to be point-like.

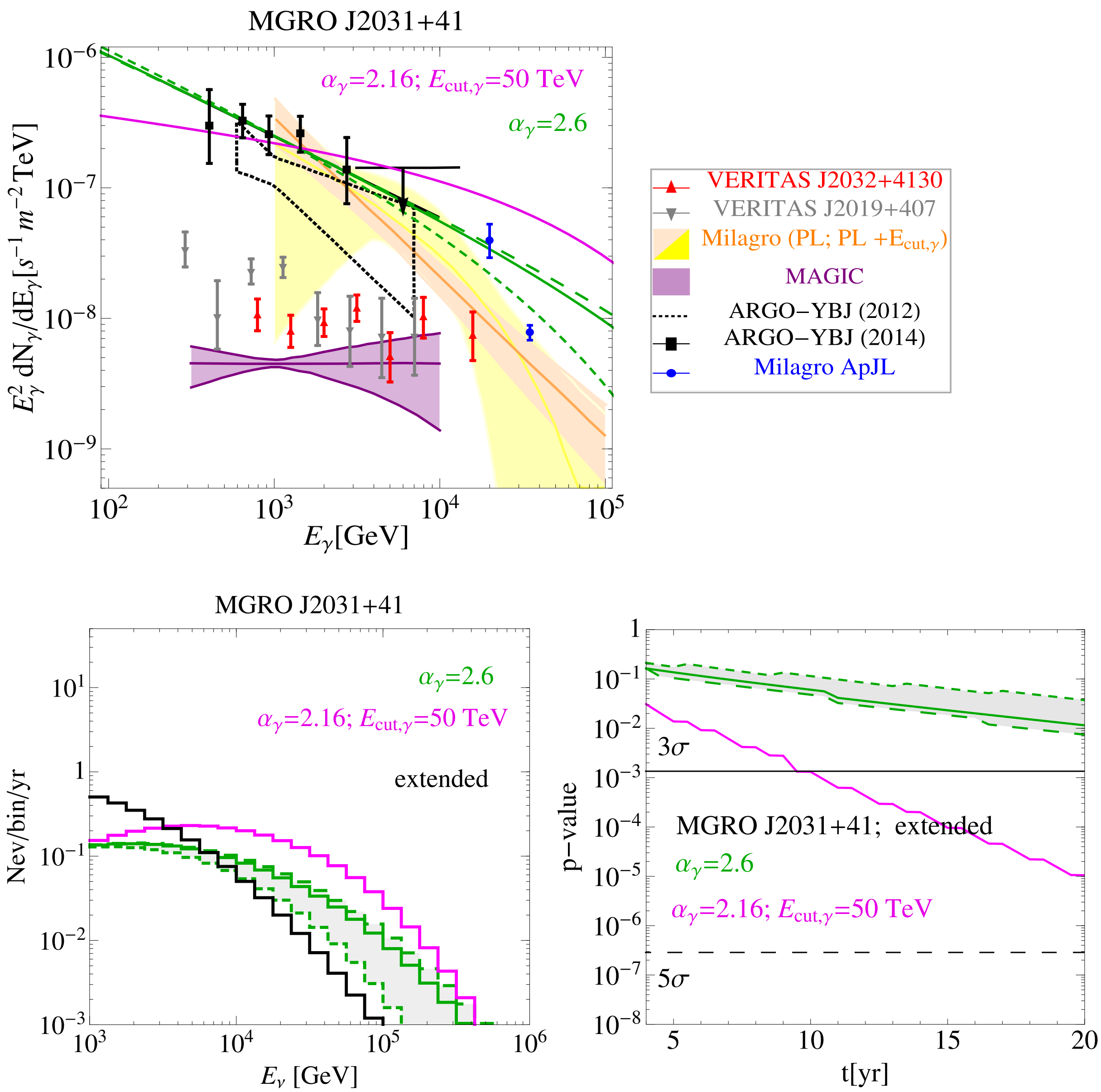


**Figure 6.7:** Upper panel: The black points show the data reported by ARGO-YBJ in Ref. [128], while the dotted region is the one reported in Ref. [123]. The previous flux measurements by Milagro are shown in blue [113, 114], while the orange/yellow area denotes the the power-law model/the power-law model with cut-off as reported in Ref. [107] by Milagro. With the purple band we report the measurements by MAGIC [124]. We report in red and grey the results from the VERITAS detector [127]. With green/magenta lines we show the spectra obtained fixing the parameters to the best fit reported in Table 6.2 for the case without/with Fermi data. In the case without Fermi data, we also allowed the cut-off energy to vary: $E_{\mathrm{cut},\gamma} = 30,\ 300, and\ 800$ TeV (short-dashed, solid, and long-dashed lines, in green. Lower panel, left: Number of events for the spectra reported with green and magenta lines in the upper panel. The gray band encodes the uncertainty on the cut-off energy. With black lines, we show the background from atmospheric neutrinos. Lower panel, right: p-values as a function of time, from 4 years to 20 years.

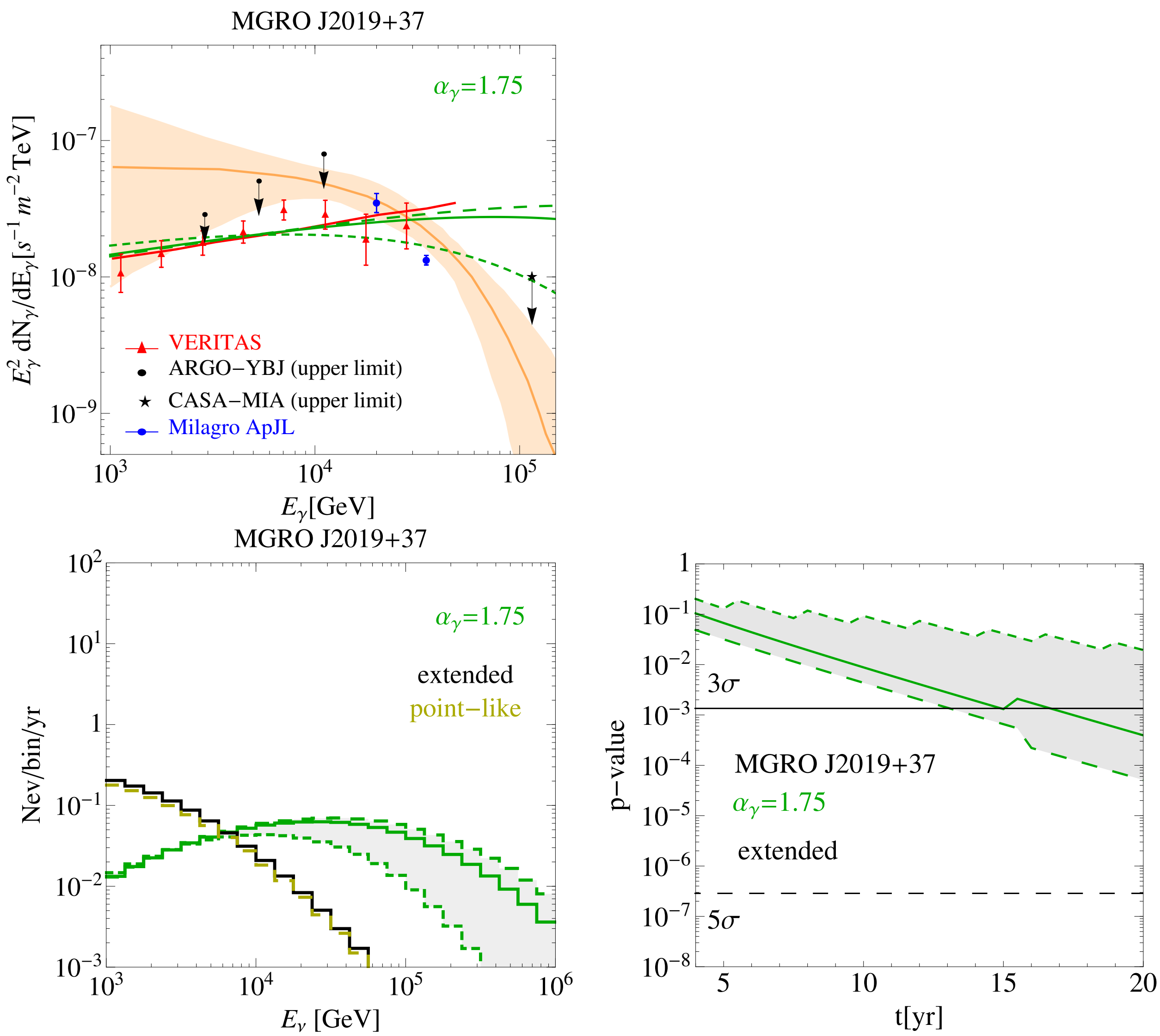


**Figure 6.8:** Upper panel: With red points, we report the VERITAS data [117]. With blue lines, we report the previous flux measurements by Milagro [113, 114], while the continuous orange line and the shaded orange area represent the best fit and $1\sigma$ band [107] as reported by Milagro. The 90% C.L. upper limits from ARGO-YBJ are shown in black [123], and the inferred CASA-MIA bound [129] is shown with a black star. With green lines we show the spectra obtained fixing the parameters to the best fit reported in Table 6.2, where we also allowed the cut-off energy to vary: $E_{\text{cut},\gamma} = 30,\ 300, \textit{and}$ 800 TeV (short-dashed, solid, and long-dashed lines, in green). Lower panel, left: Number of events for the spectra reported with green and magenta lines in the left panel. The gray band encodes the uncertainty on the cut-off energy. With the black (gold dashed) line, we show the background from atmospheric neutrinos for extended (point-like) sources. Lower panel, right: p-values as a function of time, from 4 years to 20 years.

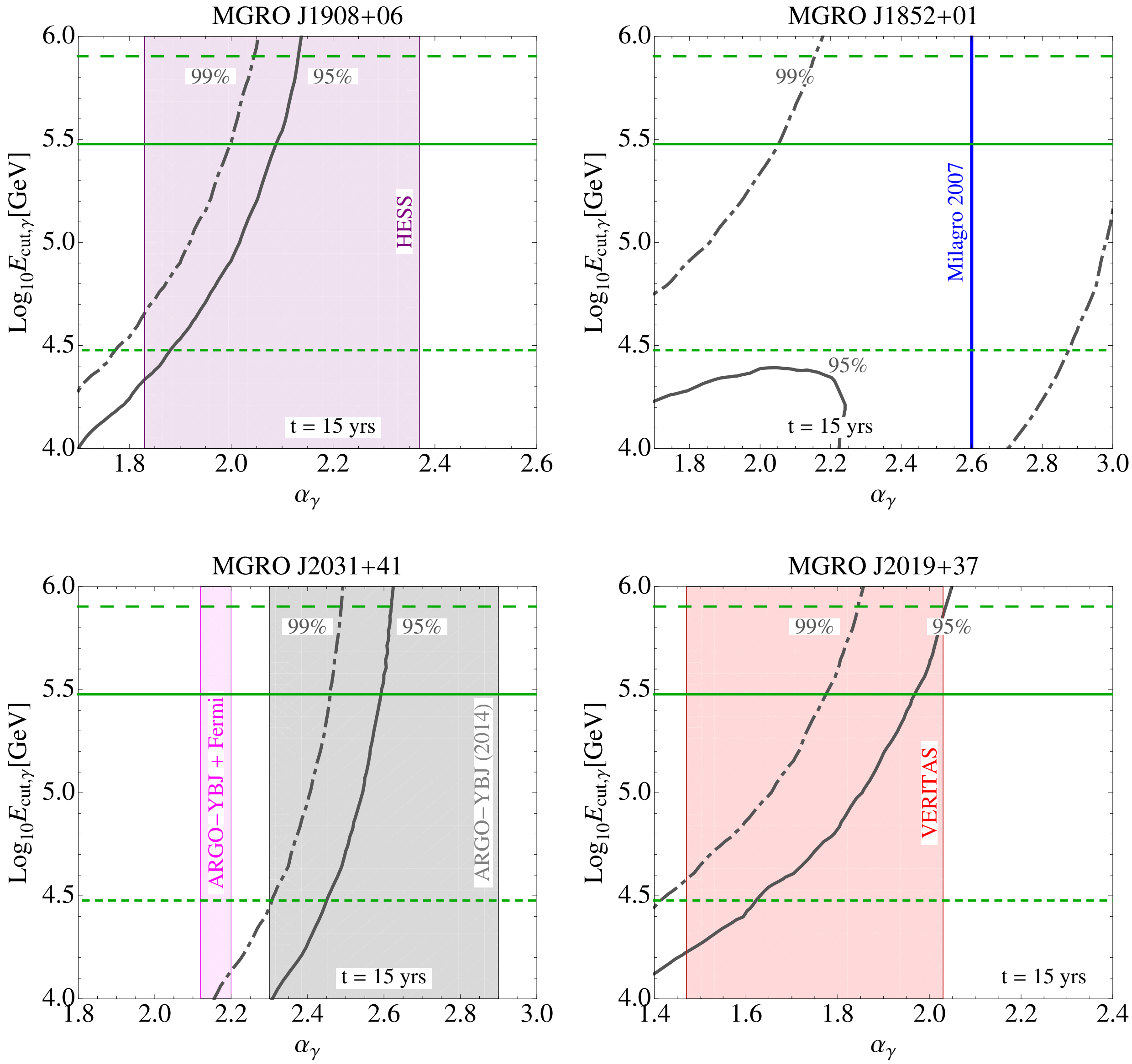


**Figure 6.9:** Upper panel: Values of $\alpha_\gamma$ and $E_{cut,\gamma}$ excluded at 95% (solid) and 99% C.L. (dot-dashed) with 15 years of IceCube running with its 86-string configuration. The normalization has been fixed to the best fit reported by HESS [116] (left) and Milagro 2007 (right). We have assumed extended sources. With horizontal lines we denote the values $E_{\rm cut,\gamma} = 30,\ 300, and\ 800$ TeV (short-dashed, solid, and long-dashed lines, in green). The purple region (left) denotes the values of $\alpha_\gamma$ reported by HESS. The blue line (right) denotes the value of $\alpha_\gamma$ considered by Milagro. Lower panel: The normalization has been fixed to the best fit reported by ARGO-YBJ without Fermi-LAT [123] (left) and VERITAS [130] (right). We have assumed extended sources. The gray/magenta region (left) denotes the values of $\alpha_\gamma$ reported by ARGO-YBJ without/with Fermi data. The red region (right) denotes the values of $\alpha_\gamma$ reported by VERITAS.

# Chapter 7

# Searching for neutrinos from fast radio bursts with IceCube

## 7.1 Introduction

In this chapter, we present the results of a search for temporal and spatial coincidence of neutrinos with four fast radio bursts detected by the Parkes and Green Bank radio telescopes during the first year of operation of the complete IceCube Neutrino Observatory; IC86-I.

Fast radio bursts (FRBs) are a new class of astrophysical radio transients with few millisecond) duration. The first FRB was discovered in a 2007 analysis of archival data from the Parkes telescope in 2001 [144]. The burst became known as the Lorimer Burst. Since 2007, a total of 34 bursts have now been detected by three different telescopes: Parkes, Arecibo, and Green Bank. These bursts have been detected from 18 unique directions. 17 bursts at different times has been reported from the direction of one of the bursts observed by Arecibo [145, 146].

Given their rate of detection by radio surveys performed with relatively low exposure time and field of view, the rate of FRBs across the entire sky is estimated to be several thousand per day [147].

The origin of FRBs, as well as their emission mechanism, is unknown. Models have proliferated and include the birth of black holes from supermassive neutron stars ("blitzars") [148] and giant flares from magnetars [149]. Their large dispersion measures indicate an extragalactic origin, but they could also come from Galactic sources enshrouded in dense plasma [150]. The discovery of a repeating Arecibo burst [145] disfavors cataclysmic models. While leptonic emission is the default assumption, hadronic emission mechanisms are also possible along with the resulting connection to cosmic rays and potential neutrino emission [151]. FRBs

*This study has been submitted to Astrophysical Journal:* S. Fahey, A. Kheirandish, J. Vandenbroucke, and D. Xu, A search for neutrinos from fast radio bursts with IceCube, 2016.

have been detected from high Galactic latitudes. A host galaxy detection and corresponding redshift was claimed [152]. However, this claim turned out to be a background active galactic nucleus [153].

FRBs are solely observed in radio wavelengths. No FRB prompt or after-glow counterpart emission has yet been detected in any wavelength or messenger other than radio waves. Because of their very short duration, prompt counterparts can only be detected serendipitously, most likely by wide field instruments. Because there is still so little known about the nature of fast radio bursts, model-independent searches using a variety of wide-field instruments likely stand the best chance of discovering a counterpart.

## 7.2 Neutrino Sample

Here, we use through going muon sample from first year of completed IceCube detector; IC86. This sample was selected and optimized to search for neutrino point sources, see [91] for details on event selection.

For this study we used the released sample by IceCub collaboration [154], which includes the time of the event truncated to the integer Modified Julian Day (MJD), the best-fit energy and direction, and an estimate of the direction uncertainty (50% containment radius).

The data set includes a total of 138,322 events from 333 days of livetime spanning May 2011 to May 2012 (MJD 55694 through 56062), with a roughly equal number of events from the Northern and Southern hemisphere. Events with declination greater than -5° are considered *up-going* events and are predominantly atmospheric neutrinos. The Southern hemisphere is dominated by cosmic-ray-induced atmospheric muons and high-energy muon bundles (multiple muons produced in the same extensive air shower). Therefore, *down-going* events that were reconstructed to be from declination less than -5° are dominated by atmospheric muons.

As discussed in [91], the event selections were performed separately for the Northern and Southern hemispheres with Boosted Decision Trees. In the *up-going* region, the ice and the Earth act as a shield for atmospheric muons, so a high purity neutrino sample with a wide energy range can be obtained. In the *down-going* region, high-energy neutrinos are also retained, but a high purity neutrino sample cannot be reached due to the rate of atmospheric muons. In order to bring the atmospheric muon contamination under control, a higher energy threshold was applied in the Southern sky.

The rate of detected events in the sample varies from day to day both due to seasonal variation in the production of atmosphere neutrinos and muons [155] and detector effects (downtime). We estimated the size of possible downtime effects from the number of IceCube events detected on the day of each FRB. They

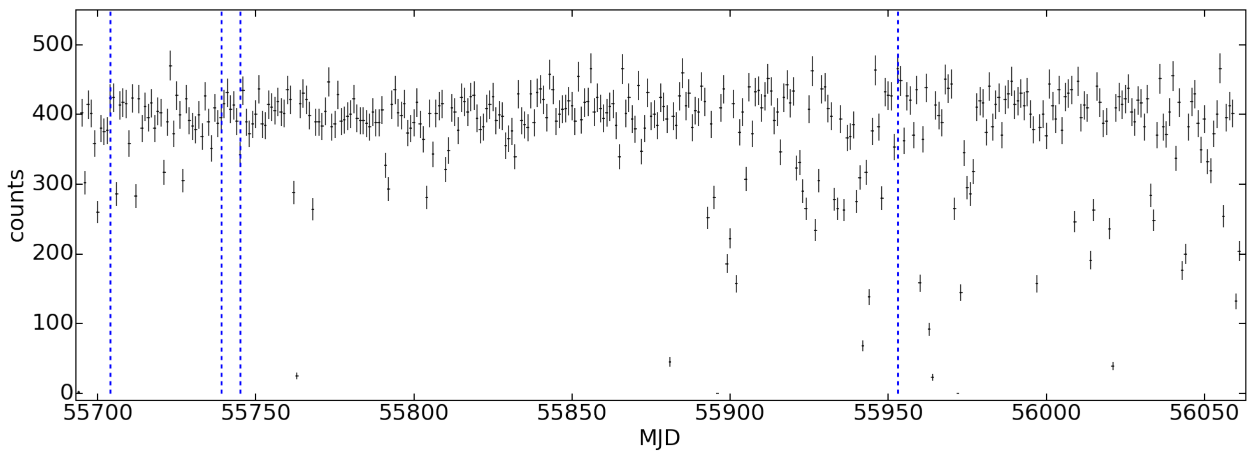


**Figure 7.1:** Number of events observed per day (MJD) (black) during the livetime of IC86-I considered in this analysis. The dates bursts in this analysis have occurred are identified (dashed blue)

are (in time order of the FRB occurrence) 423, 395, 342, and 465. The event count on each day is within ∼20% of the average rate for the full sample (375). Therefore, detector dead-time was likely not substantial on any of the FRB days, see Fig. 7.1.

Fig. 7.2 shows the event rate in this sample as a function of declination, averaged over right ascension and time. Because of the higher energy threshold applied in the Southern hemisphere to counteract the high atmospheric muon rate, the event rate varies by only a factor of ∼2 across the sky. The average rate is 0.009 events per square degree per day.

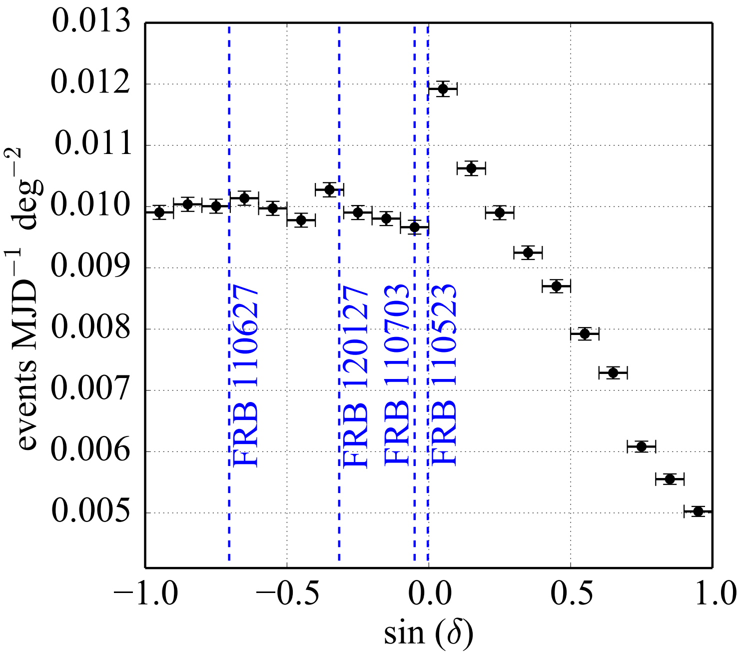


**Figure 7.2:** Event rate in the IceCube data sample as a function of declination, averaged over right ascension within each declination band. The declination of each FRB is shown for reference. The rate is normalized per day between MJD 55694 and 56062 (369 days), not per day of livetime.

## 7.3 Coincidence search

During IC86-I, four FRBs have been detected: FRB 110523 [156], FRB 110627, FRB 110703, and FRB 120127 [157]. Two are near the celestial equator and two are well South of it. Since IceCube neutrinos times are available as truncated in MJD, temporal coincidence with these FRBs can only be tested on the one-day scale. However, the event rate is low enough that this time resolution is sufficient for an effective search. For each FRB, we truncate the detection time was in MJD and find the angular distance to each MJD-coincident IceCube event. The localization error of each FRB is $\sim 0.2°$ or better, negligible in this analysis in comparison to neutrinos angular resolution [156].

We assume for this search that the point spread function for each event can be approximated by a radially symmetric two-dimensional Gaussian. Under this assumption, the radius of the 90% and 99% error circles can be determined from the 50% error circle by multiplying by a factor of 1.82 and 2.58, respectively. Figure 7.3 shows these error circles for coincident events near each of the FRBs. The nearest (relative to its error circle) coincident event is separated by 4.27° from FRB 110703 on MJD 55745, with a 50% angular error of 1.2°.

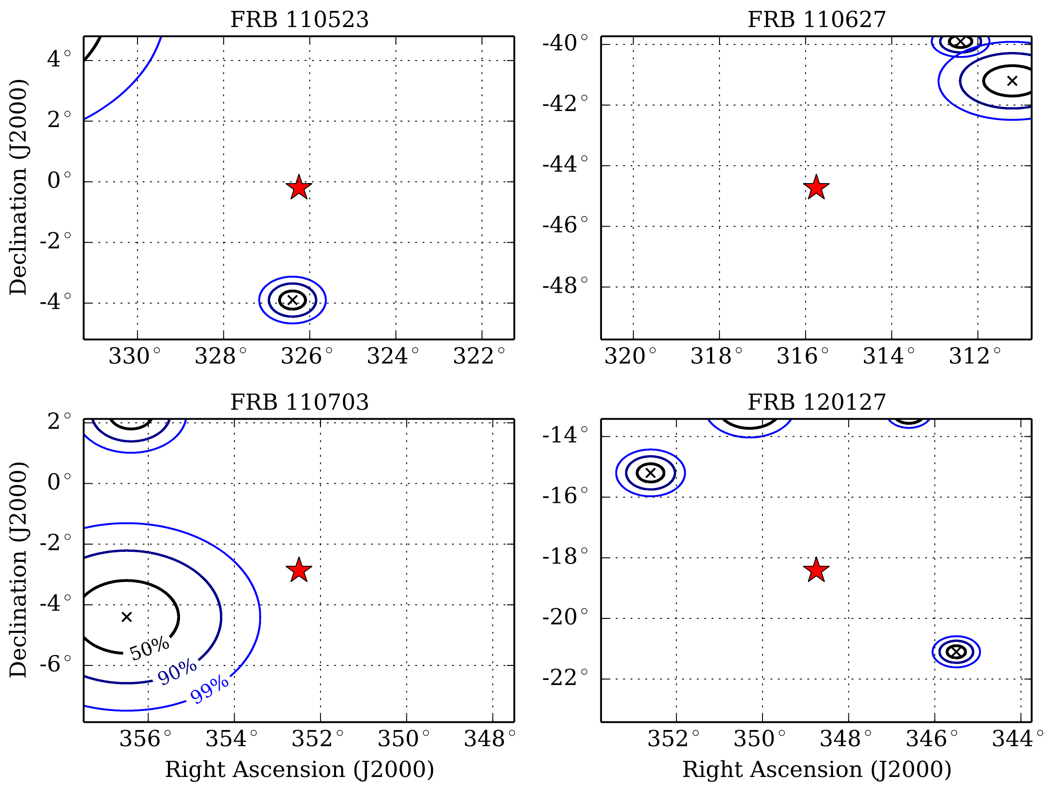


**Figure 7.3:** The region of interest centered on each FRB ($\star$) in this sample is shown in equatorial coordinates in Cartesian projection. The best-fit direction of each IceCube event is indicated with an $\times$. The 50%-containment circle for each event is shown, as is an estimate of the 90%-, and 99%-containment circles under the approximation that the point spread function is a radially symmetric two-dimensional Gaussian distribution.

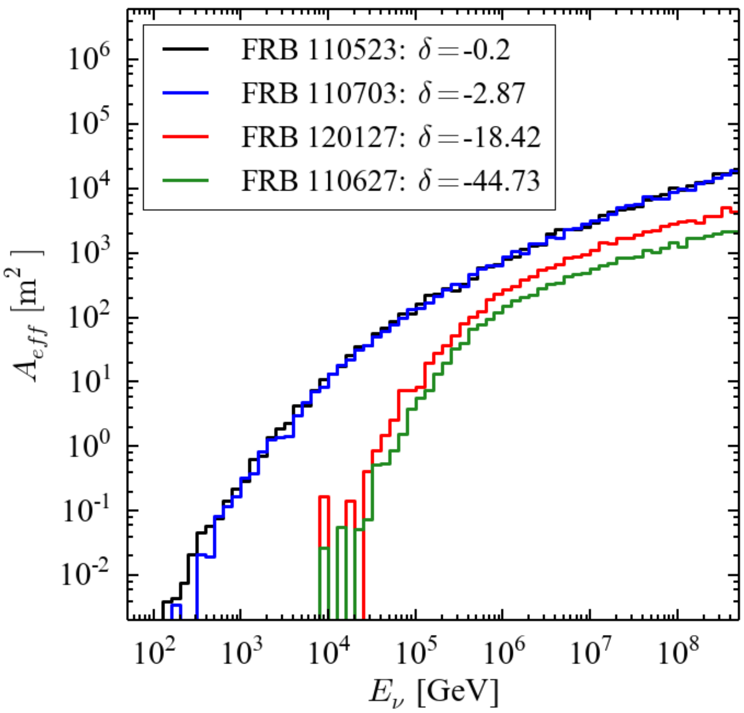


**Figure 7.4:** Muon neutrino effective area as a function of energy for the event selection used in this analysis, in the direction of each FRB. The effective area in the southern sky is less than that near the celestial equator due to tighter cuts used to reduce the atmospheric muon background.

## 7.4 Results and Constrains

In light of the absence of any coincident neutrinos in the point source sample from the first year of the full IceCube detector with the four FRBs observed in this period, we constrain the possible neutrino emission for each burst. Using the Poisson distribution to find the 90% upper limit on the flux of neutrinos, we estimate the maximum value of neutrino flux leading to detection of 2.3 neutrinos in a day.

The expected number of muon neutrinos detected from a source at zenith angle $\theta$ is

$$N_{\nu_\mu+\overline{\nu}_\mu} = \int \phi(E_\nu)\, A_{eff}(E_\nu,\theta)\, dE_\nu\, dt, \tag{7.1}$$

where $\phi(E_\nu)$ is the neutrino flux at the earth and $A_{eff}$ is the IceCube effective area as a function of neutrino energy and zenith. The effective area corresponding to the event selection and selected for each FRB based on its declination is shown in Fig. 7.4. In order to constrain the neutrino flux, we assume the flux to be a power law

$$\phi(E_\nu) = \phi_0 \big(\frac{E_\nu}{E_0}\big)^{-\gamma}. \tag{7.2}$$

We set the normalization energy, $E_0$, to 100 TeV and consider five different spectral indices ranging from 1 to 3. To calculate the expected number of events we perform the integral in Equation 7.1 from 1 TeV to 1 PeV in neutrino energy.

Fig. 7.5 shows for each burst the distribution of event energies that IceCube would detect for various power law neutrino spectra. The shape of each curve is determined by multiplying the flux by the effective area, and each curve is normalized to 2.3 total number of events, i.e. to the 90% confidence level upper limit on the expected number of events detected from the burst. As the figure shows, the tightest limits arise from the FRBs found near the celestial equator. This is a result of IceCube's effective area peaking in this direction.

For the two bursts well below the celestial equator, the effective area curves at these declinations have large fluctuations near ∼20 TeV, perhaps due to statistical uncertainty close to the energy threshold in the Monte Carlo used to determine the effective area. This is the cause of the fluctuations seen at ∼20 TeV in the right two panels of Figure 7.5. Fig. 7.6 shows the corresponding time-integrated flux upper limits for several assumed spectral models for each FRB.

The neutrino fluence (time-integrated energy flux) is

$$f = \int_{E_{min}}^{E_{max}} E\,\phi(E)\,dE\,dt, \tag{7.3}$$

where $E_{min} = 10$ TeV and $E_{max} = 1$ PeV. Table 7.1 shows the neutrino fluence upper limit for each burst for the specific case of $\gamma = 2.0$.

A more sensitive search can be performed for high-energy neutrinos from these and additional FRBs both by analyzing subsequent years of IceCube data and by using a looser event selection with greater effective area and greater background rate but on shorter time scales, similar to the strategy used for gamma-ray burst neutrino searches [158, 159]. Furthermore, a search for MeV neutrinos can be performed using an analysis strategy similar to that used for nearby supernovae [160].

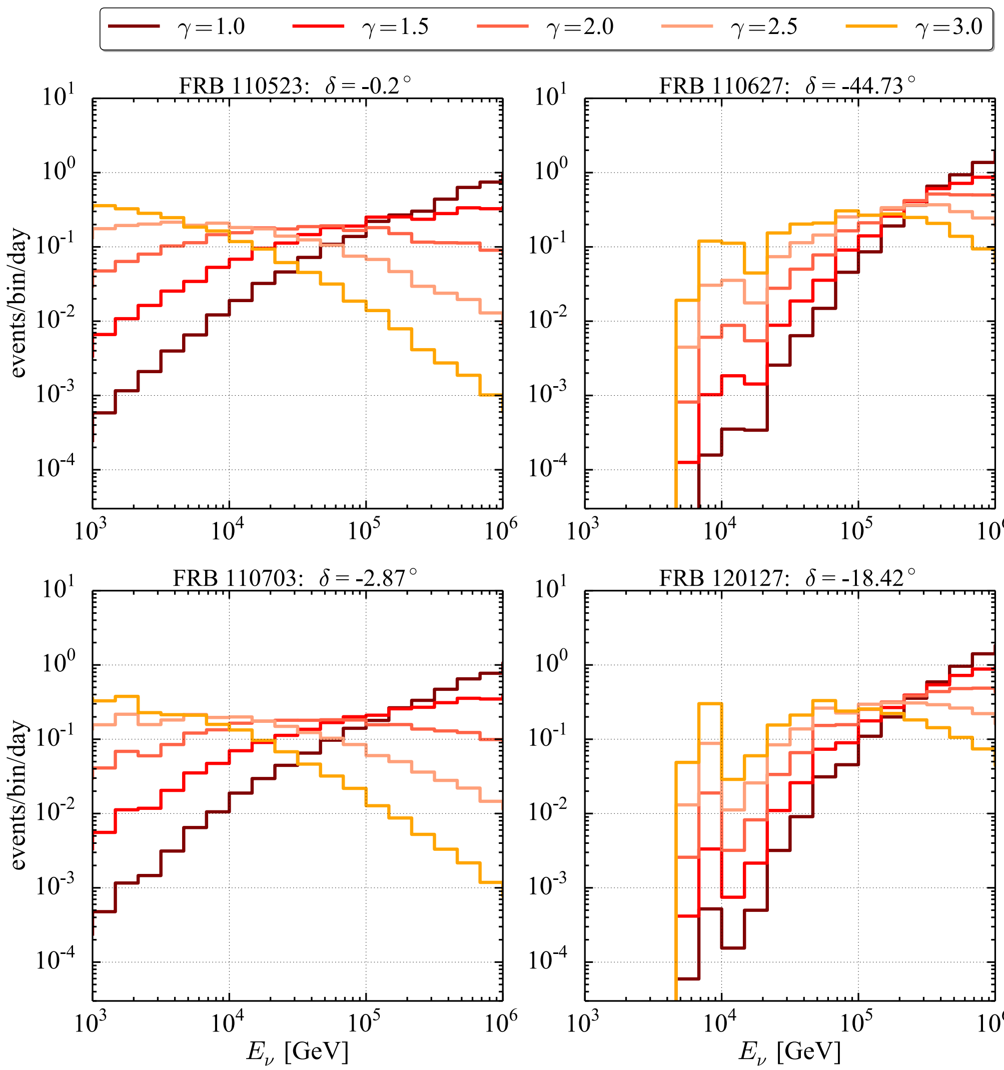


**Figure 7.5:** Energy distribution of events that would be detected if the neutrino flux saturated our upper limits. Each curve is determined by multiplying the power-law spectral model by the detector effective area and normalizing so that the integral is 2.3 events (the 90% confidence level upper limit on the event rate given that zero events were detected). Several power law indices ($\gamma$) were tested.

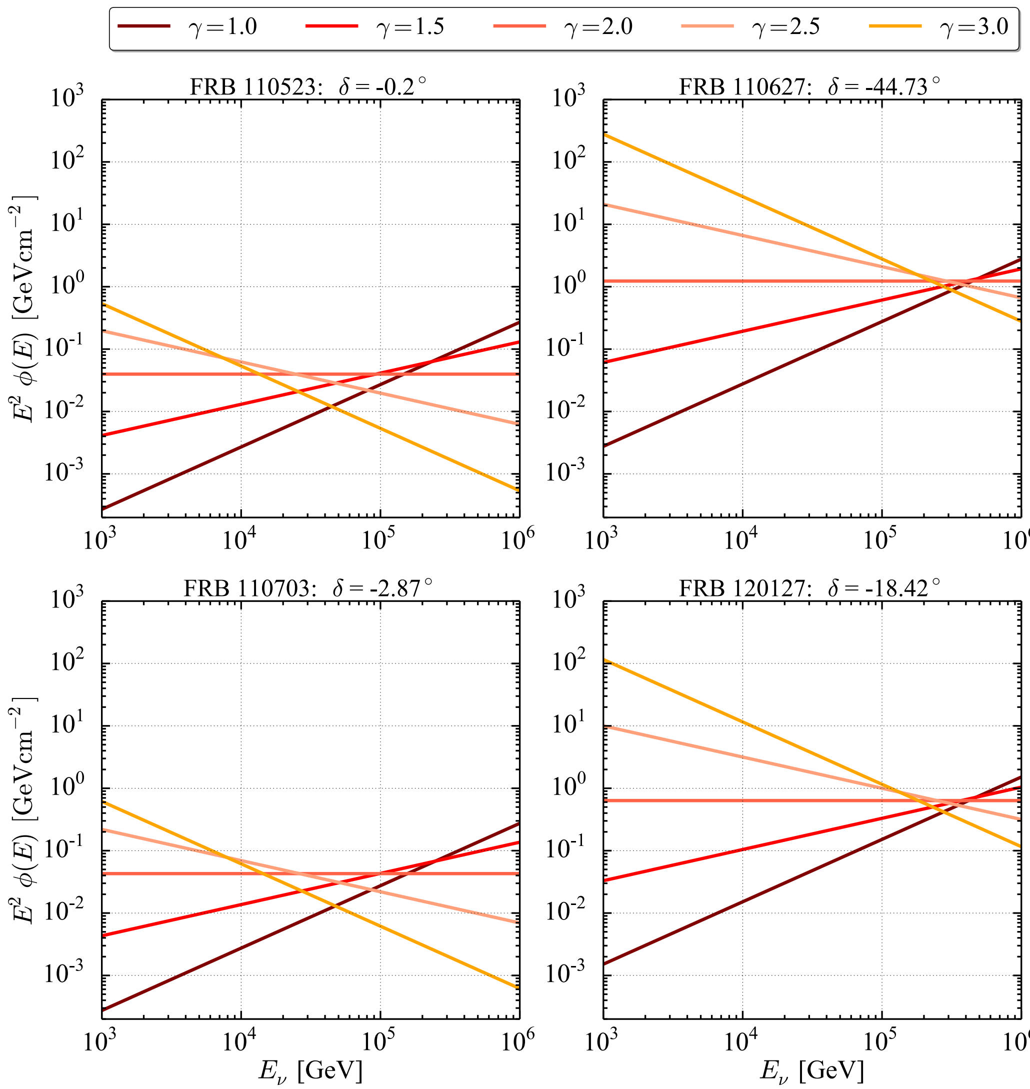


**Figure 7.6:** Upper limits (90% confidence level) on the time-integrated neutrino flux from each FRB, assuming a power-law neutrino spectrum with index $\gamma$.

| FRB | R.A. | Dec. | FRB MJD | Radio fluence (GeV cm$^{-2}$) | Telescope | $\Delta\Psi_{\nu-\mathrm{FRB}}$ | $\nu$ error (50%) | $f^{90\%}$ (GeV cm$^{-2}$) |
|---|---|---|---|---|---|---|---|---|
| 110523 | 21h45' | -00°12' | 55704.63 | $2.37 \times 10^{-15}$ | Green Bank | 3.70° | 0.3° | 0.184 |
| 110627 | 21h03' | -44°44' | 55739.90 | $1.75 \times 10^{-15}$ | Parkes | 4.85° | 0.5° | 4.84 |
| 110703 | 23h30' | -02°52' | 55745.79 | $4.49 \times 10^{-15}$ | Parkes | 4.27° | 1.2° | 0.184 |
| 120127 | 23h15' | -18°25' | 55953.34 | $1.50 \times 10^{-15}$ | Parkes | 4.07° | 0.2° | 2.76 |

**Table 7.1:** Characteristics of each fast radio burst (right ascension, declination, time, radio fluence, and telescope that detected it) and of the nearest IceCube event detected on that day (angular distance from FRB, error radius). The final column gives the 90% confidence level upper limit on the neutrino fluence from the burst assuming the neutrino spectrum is a power law with index 2.0.

# Chapter 8

# Constraining dark matter-neutrino interactions with high-energy astrophysical neutrinos

## 8.1 Introduction

Even though the effects of cosmological dark matter (DM) have only been observed via its gravitational influence, the O(1) ratio between the dark and baryonic components of the Universe $\Omega_{DM} \sim 5\Omega_b$ hint at a non-gravitational link between the two sectors. An annihilation cross section of DM near the weak scale, for instance, easily produces the observed relic density through thermal decoupling – an observation known as the *WIMP miracle* (see e.g. [161]). Regardless of the exact production mechanism, the existence of a process $\mathrm{DM} - \mathrm{DM} \to \mathrm{SM} - \mathrm{SM}$ implies that the elastic scattering process $\mathrm{DM} - \mathrm{SM} \to \mathrm{DM} - \mathrm{SM}$ exists and may be measured in the laboratory. Most notably, this is the basis for the plethora of underground direct detection experiments, aiming at observing elastic scattering between DM and quarks. However, interactions between the DM and other particles may also be present and could be the dominant, or even sole, link between the dark and visible sectors. A DM-neutrino interaction is especially attractive for light DM models, where annihilation into heavier products is kinematically forbidden, and appears naturally in some models, for example when the DM is the sterile neutrino (see [162]).

Such a possibility has been considered in depth, mainly in the context of cosmology [163, 164, 165, 166, 167, 168, 169, 170, 171, 172, 173, 174, 175, 176]. There are two ways in which dark matter-neutrino interactions can affect cosmological observables. First, if the DM is light enough ($\lesssim 10$ MeV) and is still in thermal equilibrium with neutrinos during or after Big Bang nucleosintesis (BBN), it will transfer entropy to the neutrino sector as it becomes non-relativistic. This effect, parametrized via the effective number of

This study is done in collaboration with Carlos Argüelles and Aaron Vincent, and is in preparation for publication relativistic degrees of freedom, $N_{eff}$, can dramatically affect BBN and cosmic microwave background (CMB) observables. Second, a small ongoing interaction will lead to *diffusion damping* of cosmological perturbations on small scales as power is carried away from the collapsing DM overdensities (and thus from gravitational potential perturbations) by relativistic neutrinos. This suppresses structure on small scales and, if the effect is large enough, affects the acoustic peaks of the CMB. While the former effect relies on thermal equilibrium – independent of the interaction rate–, the latter does not, and, instead, leads to limits on the cross section as a function of the DM mass.

Here, we turn to a novel complementary approach. We focus on present-day interactions between high-energy cosmic neutrinos and the dark matter halo of the Milky Way. We use events from four years of HESE observation that was already discussed in chapter 2. There, it was noted that the events arrival direction are consistent with isotropic distribution. Indeed, this isotropy has been used to place constraints on a galactic contribution, either from standard sources [97] or from the decay or annihilation of halo dark matter [177]. Here, we constrain the dark matter-neutrino interaction strength by its effect on the isotropy of the extragalactic signal. As they pass through the galaxy on their way to earth, the flux of interacting neutrinos would be preferentially attenuated in the direction of the galactic centre, where the dark matter column density is the largest. For large enough coupling strengths, this should lead to an observable anisotropy in the neutrino sky.

In order to model the DM-$\nu$ interactions at relativistic energies, explicit cross-sections must be derived. To do this, we make use of simplified models, in which a DM and mediator spin, mass, and coupling are specified, without making further assumptions on UV completion or gauge invariance of the underlying model. Simplified models are a popular and convenient middle ground between contact-interaction effective field theories – which break down when energy scales exceed the scale of new physics – and a full, rigid UV-complete theory. Such models have been in use for over a decade [178] and have gained prominence in the past few years in the quest to compare high-energy collider results with low-energy searches of particle dark matter.

We consider four distinct simplified models which give rise to different high-energy behavior: a scalar DM candidate with a scalar mediator; a fermionic DM candidate that interacts via a scalar or vector mediator (a Higgs-like or Z'-like interaction), and finally a scalar DM candidate interacting via a fermionic mediator – reminiscent of sneutrino DM with a neutralino mediator [179, 180], though this scenario has also been generalized as a way of obtaining neutrino masses via a light DM sector [181].

To compute our constraints, we construct a full un-binned likelihood for the observed events at IceCube, based on the observed event energies and arrival directions. This must include a non-zero probability that each event be of background (atmospheric) origin. We establish our limits via a Markov Chain Monte Carlo search of the parameter space of each model, represented by the dark matter, mediator masses, and the coupling strength.

In this chapter first, we describe the simplified model framework that we use, laying out the relevant diagrams and dark matter-neutrino elastic scattering cross sections, as well as the propagation equation that must be solved in order to model the attenuation of the cosmological neutrino signal by the Milky Way's DM. This is followed by a description of the IceCube neutrino observatory and of the high-energy events used for this analysis in Sec. 8.3.

## 8.2 Neutrino-Dark Matter interaction

The existence of a new mediator connecting the dark sector to neutrinos leads to a non-vanishing elastic scattering cross section. We use the formalism of "simplified models" [178, 182, 183] to parametrize the effective theory of a new interactions between neutrinos and the dark sector. In this framework, one specifies a spin and mass for the dark matter and the new mediator, as well as a coupling, to construct new effective interaction terms in the Lagrangian. This approach allows consistent computation of interaction cross sections at energies well above the mediator mass, which would not be possible if one simply considered four-point contact interactions.

Here, we focus on four simplified models which give rise to potentially observable neutrino-DM interactions in the galaxy: a scalar DM with a scalar or fermionic mediator; and fermionic DM with a scalar or vector mediator. In all cases, we refer to the DM particle as $\chi$ and the mediator as $\phi$. The four models we considered are shown in Fig. 8.1. Differential and total scattering cross sections for each of these models are given in App. A.1. These are computed in the frame of the Galaxy, where the DM is at rest, since non-relativistic thermal velocities can safely be neglected.

We take the incoming neutrino flux to be isotropic, extragalactic in origin, and model it as a power law in energy. As the neutrinos propagate towards the Earth, they must traverse the diffuse dark matter halo of the Milky Way, and in particular through the very DM dense galactic center. Each arrival direction is therefore subject to a different column density of dark matter, and thus a different scattering rate, which is reflected as an anisotropic attenuation of the signal observed at Earth.

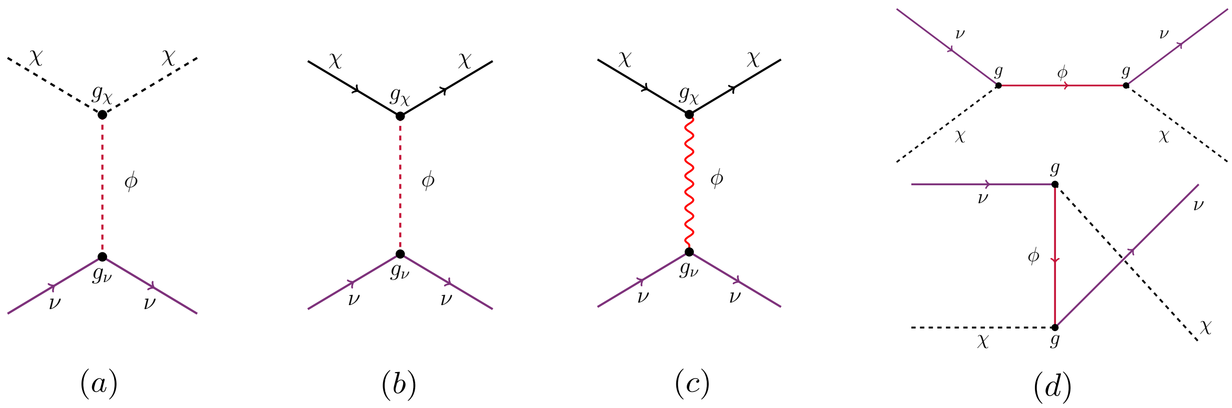


**Figure 8.1:** The four simplified DM-neutrino interaction models considered: (a) scalar dark matter-scalar mediator, (b) fermion dark matter-scalar mediator, (c) fermion dark matter-vector mediator, and (d) scalar dark matter-fermion mediator.

The attenuation of the extragalactic high-energy neutrino flux is described by the following cascade equation

$$\frac{d\phi(E)}{d\tau} = -\sigma(E)\phi(E) + \int d\tilde{E}\frac{d\sigma(\tilde{E},E)}{dE}\phi(\tilde{E}), \tag{8.1}$$

where $\tau$ is the DM column density and $E$ is the neutrino energy. The first term on the right-hand side of (8.1) accounts for the down-scattering of neutrinos from energy $E$ to any other, while the second term accounts for the reverse effect: scattering of neutrinos from any other energy $\tilde{E}$ to $E$. Eq. (8.1) can be simplified by applying the partial solution $\phi \equiv e^{-\sigma\tau}\tilde{\phi}$, reducing to

$$\frac{d\tilde{\phi}}{d\tau} = e^{\sigma(E)\tau}\int d\tilde{E}\frac{d\sigma(\tilde{E},E)}{dE}e^{-\sigma(\tilde{E})\tau}\tilde{\phi}(\tilde{E}), \tag{8.2}$$

which we be solve numerically. This differential equation is solved up to the column density

$$\tau(b,l) = \int_{l.o.s} n_\chi(x;b,l)\ dx, \tag{8.3}$$

where $b$ and $l$ are respectively the galactic latitude and longitude, and $n_\chi(x;b,l)$ is the dark matter number density profile of the Milky Way along the line of sight (l.o.s).

To model dark matter distribution of the Milky Way, we take an Einasto profile with shape parameters that fit the Via Lactea II simulation results , and a local DM density of $\rho_\odot = 0.3$ GeV cm$^{-3}$ . The DM column density and the arrival direction of high-energy cosmic neutrinos are shown in Fig 8.2.

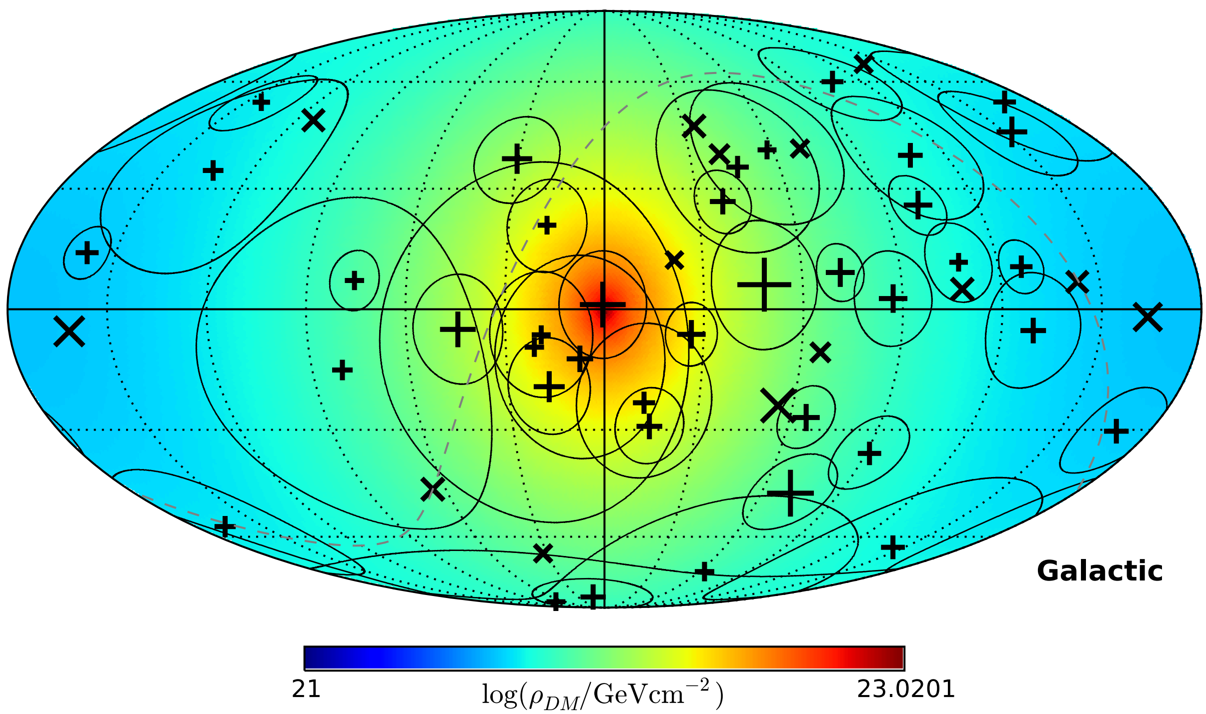


**Figure 8.2:** The arrival direction of the 54 high energy starting events observed in 4 years of IceCube data [29], in galactic coordinates. Crosses represent shower events, while x's correspond to tracks. The color scale is the column density of dark matter traversed by neutrinos arriving from each direction.

## 8.3 Data set and Likelihood test

### 8.3.1 Data

We use high-energy neutrino events from 4-year HESE analysis discussed in chapter 2 , which consists of 14 tracks and 40 cascades making a total of 54 events shown in Fig. 8.2. These events are compatible with a power law spectrum given by $E^2\phi(E) = 2.2 \pm 0.7 \times 10^{-8}(E/100\,\mathrm{TeV})^{-0.58}\,\mathrm{GeV}^{-1}\mathrm{cm}^{-2}\mathrm{s}^{-1}\mathrm{sr}^{-1}$. Details on HESE analysis and results was described in Chapter 2.

### 8.3.2 Likelihood function

If the incoming neutrino flux is indeed of extragalactic origin, then it can be reasonably assumed to be isotropic, have a flavor composition $(\nu_e : \nu_\mu : \nu_\tau) = (1 : 1 : 1)$, and have equal flux of neutrinos and antineutrinos. This is the expected composition for an origin mainly in pion decay, which is the expected dominant mechanism. Nonetheless, a different flavor composition at production will yield an oscillation-averaged flux that is very close to $(1 : 1 : 1)$, and with current statistics, would not be distinguishable within the space of flavors allowed by oscillation [184]. Furthermore, as noted in [185], if the production mechanism is pion dominated, then – even in the presence of new physics in the propagation – the expected flavor ratio is close to $(1 : 1 : 1)$. Given that the precise value of the astrophysical neutrino spectral index at the sources is not yet know, for definiteness, we set it to the expected value from Fermi acceleration mechanisms, i.e.$\gamma = 2$; this assumption does not impact our results strongly.

Based on these assumptions, we construct the following un-binned likelihood function for a given parameter set $\vartheta$ and set of observed topologies, energies, and arrival directions $\{t, E, \vec{x}\}$

$$\mathcal{L}(t, E, \vec{x}|\vartheta) = e^{-N_{ast}-N_{atm}-N_\mu} \prod_{i=1}^{N_{obs}} \Big( N_{ast}P_{ast}(t_i, E_i, \vec{x}_i|\vartheta) + N_{atm}P_{atm}(t_i, E_i, \vec{x}_i) + N_\mu P_\mu(t_i, E_i, \vec{x}_i) \Big), \tag{8.4}$$

where the probabilities are defined by

$$P_{ast}(t_i, E_i, \vec{x}_i) \sim \sum_{f=e,\mu,\tau} R_t(\vec{x}_i, \vec{x}_{true}) R_t(E_i, E) A_{eff}(f, E, t, \vec{x}_{true}) \phi_{ast}(E, \vec{x}_{true}|\vartheta) \tag{8.5}$$

$$P_{atm}(t_i, E_i, \vec{x}_i) \sim \sum_{flv=e,\mu,\tau} R_t(\vec{x}_i, \vec{x}_{true}) R_t(E_i, E) A_{eff}(f, E, t_i) P_{veto}(f, E, t, \vec{x}) \phi_{atm}(E, \vec{x}_{true}) \tag{8.6}$$

and $P_\mu(t_i, E_i, \vec{x}_i)$ is atmospheric muon distributions reported in [34]. The sum runs over the observed events ($N_{obs} = 54$). Then we integrate over the true neutrino energy and direction. We introduce the detector angular resolution $R_t(\vec{x}_i, \vec{x}_{true})$ which we take as a Gaussian center around $\vec{x}_i$ with median uncertainties reported in [28, 29]. Similarly we introduce the detector energy resolution where we again assume normal distributions. Then, we consider $P^{atm}$ is a probability that event $i$ is of atmospheric origin, while $P(f|t_i)$ is the probability that an event of energy $E$ and flavor $f$ yield the observed topology $t_i = \{\text{track, shower}\}$. This includes a nonzero likelihood of track misidentification. $A_{eff}$ is the neutrino effective area reported in [34]. Finally, $\phi(E, b, l)$ is the solution to the propagation equation (8.1), where the galactic latitude and longitude $(b, l)$ implicitly specify the column density given by (8.3). The model dependence of eq. 8.4 thus comes from the directional attenuation with respect to the isotropic hypothesis, $\mathcal{L} \propto \phi(E, b, l|\vartheta)/\phi^{iso}(E)$.

## 8.4 Constraints from the IceCube data

We produce constraints on the DM-$\nu$ scattering rate by evaluating Eq. 8.4 with the publicly available `emcee` [186] Markov Chain Monte Carlo software. We scan over uniform priors in the space of $\{\log m_\chi, \log m_\phi, \log g_\chi g_\nu\}$. The upper limits on the coupling versus dark matter and mediator mass for each simplified model is shown in Fig. 8.3

### 8.4.1 Comparison with cosmological constraints

Cosmological limits on the DM-neutrino scattering cross-section are obtained for two forms of the low-energy cross section: either constant with temperature, or proportional to $T^2$. Cosmological limits combining Planck CMB data [187] and WiggleZ [188] large scale structure data give [189]:

$$\sigma_{const.} < 3 \times 10^{-31} \left(\frac{m_\chi}{\text{GeV}}\right) \text{ cm}^2; \tag{8.7}$$

$$\sigma_{T^2} < 1 \times 10^{-40} \left(\frac{m_\chi}{\text{GeV}}\right) \left(\frac{T}{T_0}\right)^2 \text{ cm}^2, \tag{8.8}$$

where $T_0$ is the cosmological neutrino temperature today $T_0 = (4/11)^{1/3} T_{CMB} = 1.95$ K.

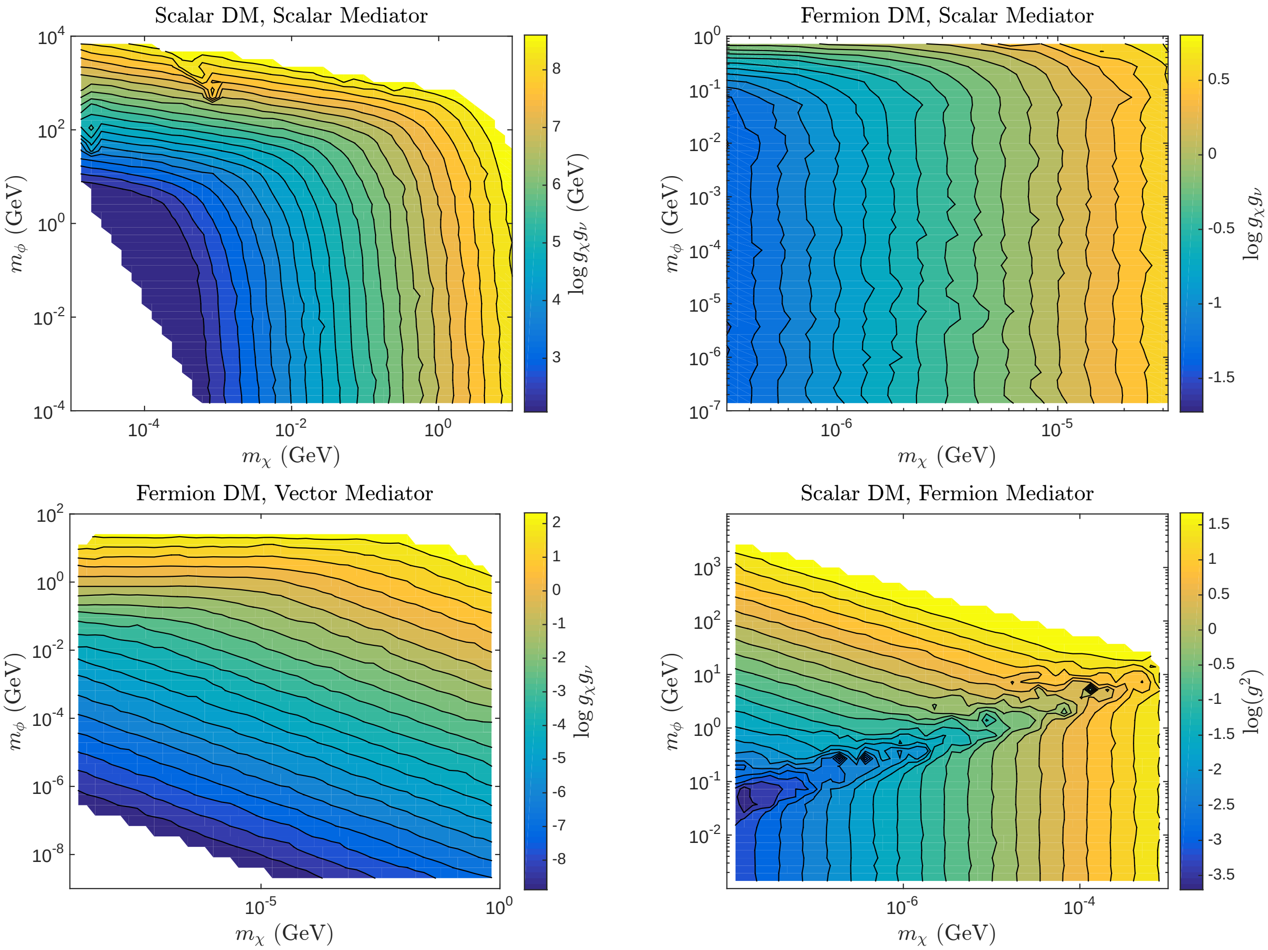


**Figure 8.3:** Upper limits on the couplings versus DM $\chi$ and mediator $\phi$ mass for each of the simplified models considered, based on the 4-year IceCube high energy contained vertex data. White regions fall outside of the scan volume.

Assuming no new physics appears at these low-energies, we can thus recast Eqs. 8.7 and 8.8 into limits in the mass-coupling parameter space. For scalar DM with a scalar mediator:

$$\sigma \simeq \frac{g^2 g'^2 E^2}{16\pi m_\phi^4 m_\chi^2} \tag{8.9}$$

For fermionic dark matter, both scalar and vector mediators yield an energy-squared ($\propto T^2$) cross section at low energies:

$$\sigma \simeq \frac{g_\chi^2 g_\nu^2 E_\nu^2}{2\pi m_\phi^4}. \tag{8.10}$$

In the case of scalar DM with a fermionic mediator, the cross section is rather:

$$\sigma \simeq \frac{g^4 m_\phi^2 E_\nu^2}{2\pi m_\chi^2 (m_\chi^2 - m_\phi^2)^2}. \tag{8.11}$$

(scalar-scalar) To compare with Eq. 8.8, the average energy per neutrino in a Fermi-Dirac distribution can be used: $\langle E_\nu^2 \rangle = 15\zeta(5)/\zeta(3)T^2 \simeq 12.9\,T^2$.

We confront our limits on parameter space with the constrains from cosmology. The results are shown in Fig. 8.4.

## 8.5 Summary

In this study, we evaluated the upper limits on the strength of the DM-neutrino interaction with high-energy cosmic neutrinos observed in IceCube. These interactions are motivated by SM-DM interactions, and we showed that IceCube cosmic neutrinos can provide constrains better than cosmology in parts of the parameter space. These constrains would improve by statistics.

It is worth mentioning that the likelihood method introduced here, in principle, is capable of tracing back other interactions of extragalactic cosmic neutrinos during their propagation provided that the interaction is powerful enough to create an anisotropy in the arrival direction of cosmic neutrinos. In the absence of any anisotropy in the arrival direction of cosmic neutrinos, the interaction strength or target density would be constrained.

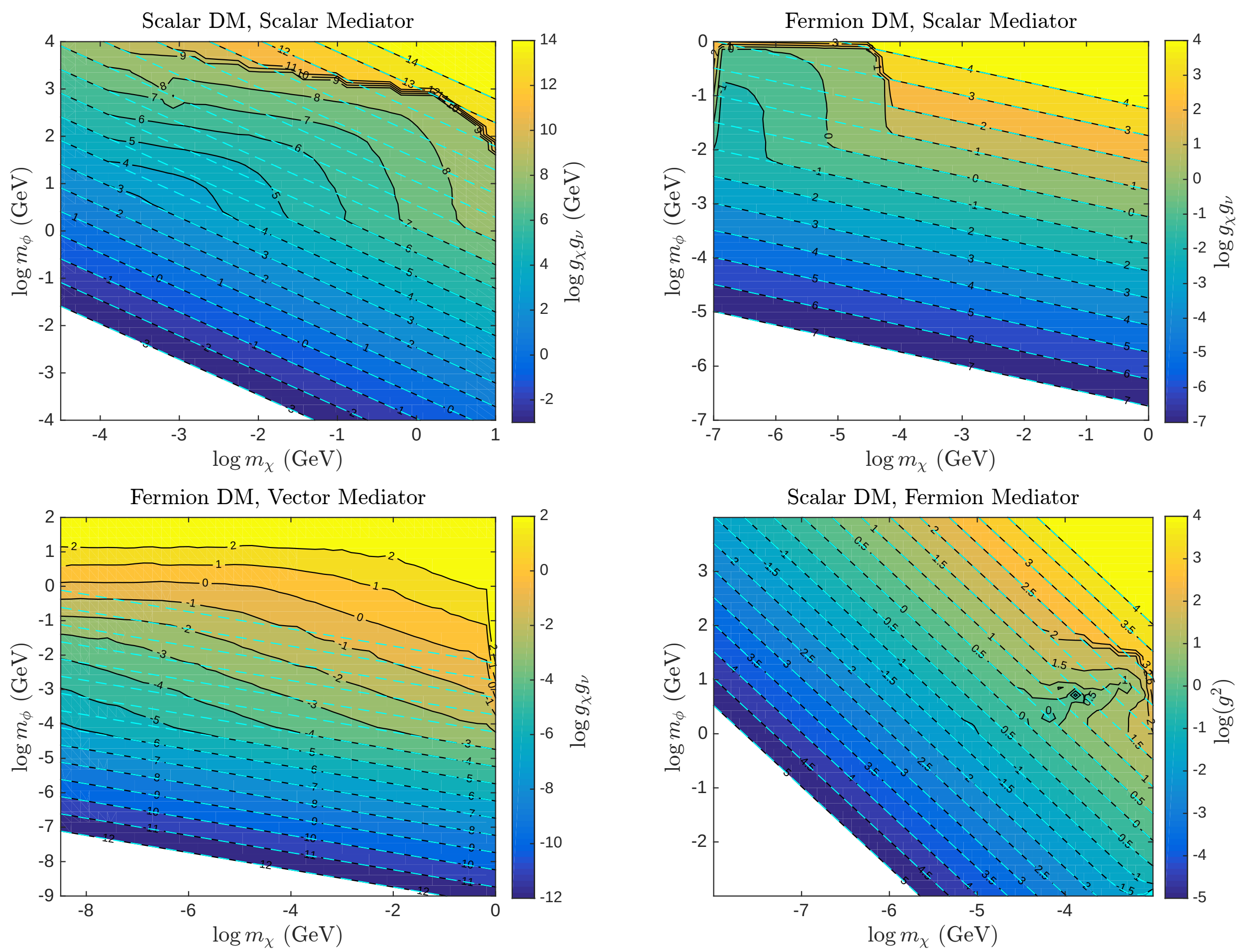


**Figure 8.4:** Combined IceCube limits from Fig. 8.3 with cosmological limits given by Eq. 8.8, for the four DM-neutrino interactions that we consider. Black contours correspond to the smallest (most constraining) of the two limits, while cyan dashed lines show the cosmological constraints alone. Contour labels are values of $\log(g_\nu g_\chi)$. Our limits are much stronger than those from cosmology at low DM mass, where kinematics favor DM-neutrino scattering

# LIST OF REFERENCES


[1] F. REINES and C. L. COWAN, "The Neutrino," *Nature*, vol. 178, pp. 446–449, 2008.

[2] F. Halzen and S. R. Klein, "Astronomy and astrophysics with neutrinos," *Phys. Today*, vol. 61N5, pp. 29–35, 2008.

[3] A. Roberts, "The Birth of high-energy neutrino astronomy: A Personal history of the DUMAND project," *Rev. Mod. Phys.*, vol. 64, pp. 259–312, 1992.

[4] T. K. Gaisser, F. Halzen, and T. Stanev, "Particle astrophysics with high-energy neutrinos," *Phys. Rept.*, vol. 258, pp. 173–236, 1995. [Erratum: Phys. Rept.271,355(1996)].

[5] J. G. Learned and K. Mannheim, "High-energy neutrino astrophysics," *Ann. Rev. Nucl. Part. Sci.*, vol. 50, pp. 679–749, 2000.

[6] F. Halzen and D. Hooper, "High-energy neutrino astronomy: The Cosmic ray connection," *Rept. Prog. Phys.*, vol. 65, pp. 1025–1078, 2002.

[7] V. F. Hess, "Observations of the Penetrating Radiation on Seven Balloon Flights," *Physik. Zeitschr*, vol. 13, p. 1084?1091, 1912.

[8] M. Ahlers, "Multi-Messenger Aspects of Cosmic Neutrinos," *PoS*, vol. ICRC2015, p. 022, 2016.

[9] A. Franceschini, G. Rodighiero, and M. Vaccari, "The extragalactic optical-infrared background radiations, their time evolution and the cosmic photon-photon opacity," *Astron. Astrophys.*, vol. 487, p. 837, 2008.

[10] "Particle Data Group,"

[11] P. Gorham, "st International Workshop on the Saltdome Shower Array (SalSA), SLAC, (2005), 1,"

[12] W. Rhode *et al.*, "Limits on the flux of very high-energetic neutrinos with the Frejus detector," *Astropart. Phys.*, vol. 4, pp. 217–225, 1996.

[13] A. Achterberg *et al.*, "Multi-year search for a diffuse flux of muon neutrinos with AMANDA-II," *Phys. Rev.*, vol. D76, p. 042008, 2007. [Erratum: Phys. Rev.D77,089904(2008)].

[14] J. K. Becker, "High-energy neutrinos in the context of multimessenger physics," *Phys. Rept.*, vol. 458, pp. 173–246, 2008.

[15] R. Engel, D. Seckel, and T. Stanev, "Neutrinos from propagation of ultrahigh-energy protons," *Phys. Rev.*, vol. D64, p. 093010, 2001.

[16] M. A. Markov

[17] J. Babson, B. Barish, R. Becker-Szendy, H. Bradner, R. Cady, J. Clem, S. T. Dye, J. Gaidos, P. Gorham, P. K. Grieder, M. Jaworski, T. Kitamura, W. Kropp, J. G. Learned, S. Matsuno, R. March, K. Mitsui, D. O'connor, Y. Ohashi, A. Okada, V. Peterson, L. Price, F. Reines, A. Roberts, C. Roos, H. Sobel, V. J. Stenger, M. Webster, and C. Wilson, "Cosmic-ray muons in the deep ocean," *Phys. Rev. D*, vol. 42, pp. 3613–3620, Dec. 1990.

[18] V. Balkanov *et al.*, "BAIKAL experiment: Status report," *Nucl. Phys. Proc. Suppl.*, vol. 110, pp. 504–506, 2002.

[19] G. Aggouras *et al.*, "A measurement of the cosmic-ray muon flux with a module of the NESTOR neutrino telescope," *Astropart. Phys.*, vol. 23, pp. 377–392, 2005.

[20] J. A. Aguilar *et al.*, "First results of the Instrumentation Line for the deep-sea ANTARES neutrino telescope," *Astropart. Phys.*, vol. 26, pp. 314–324, 2006.

[21] E. Migneco, "Progress and latest results from Baikal, Nestor, NEMO and KM3NeT," *J. Phys. Conf. Ser.*, vol. 136, p. 022048, 2008.

[22] J. Ahrens *et al.*, "Sensitivity of the IceCube detector to astrophysical sources of high energy muon neutrinos," *Astropart. Phys.*, vol. 20, pp. 507–532, 2004.

[23] P. Sommers, "Ultra-high energy cosmic rays: Observational results," *Astropart. Phys.*, vol. 39-40, pp. 88–94, 2012.

[24] F. Halzen, "Astroparticle physics with high energy neutrinos: from amanda to icecube," *Eur. Phys. J.*, vol. C46, pp. 669–687, 2006.

[25] C. Weaver, "Evidence for Astrophysical Muon Neutrinos from the Northern Sky, PhD thesis, University of Wisconsin, Madison, 2015. ," 2016.

[26] F. Halzen and D. Saltzberg, "Tau-neutrino appearance with a 1000 megaparsec baseline," *Phys. Rev. Lett.*, vol. 81, pp. 4305–4308, 1998.

[27] M. Aartsen *et al.*, "Evidence for High-Energy Extraterrestrial Neutrinos at the IceCube Detector," *Science*, vol. 342, p. 1242856, 2013.

[28] M. Aartsen *et al.*, "Observation of High-Energy Astrophysical Neutrinos in Three Years of IceCube Data," *Phys.Rev.Lett.*, vol. 113, p. 101101, 2014.

[29] M. G. Aartsen *et al.*, "The IceCube Neutrino Observatory - Contributions to ICRC 2015 Part II: Atmospheric and Astrophysical Diffuse Neutrino Searches of All Flavors," in *Proceedings, 34th International Cosmic Ray Conference (ICRC 2015)*, 2015.

[30] M. G. Aartsen *et al.*, "Observation and Characterization of a Cosmic Muon Neutrino Flux from the Northern Hemisphere using six years of IceCube data," 2016.

[31] M. G. Aartsen *et al.*, "Evidence for Astrophysical Muon Neutrinos from the Northern Sky with IceCube," *Phys. Rev. Lett.*, vol. 115, no. 8, p. 081102, 2015.

[32] R. Enberg, M. H. Reno, and I. Sarcevic, "Prompt neutrino fluxes from atmospheric charm," *Phys. Rev.*, vol. D78, p. 043005, 2008.

[33] M. Aartsen *et al.*, "Flavor Ratio of Astrophysical Neutrinos above 35 TeV in IceCube," *Phys.Rev.Lett.*, vol. 114, no. 17, p. 171102, 2015.

[34] M. G. Aartsen *et al.*, "Atmospheric and astrophysical neutrinos above 1 TeV interacting in IceCube," *Phys. Rev.*, vol. D91, no. 2, p. 022001, 2015.

[35] M. Ackermann *et al.*, "The spectrum of isotropic diffuse gamma-ray emission between 100 MeV and 820 GeV," *Astrophys. J.*, vol. 799, p. 86, 2015.

[36] K. Murase, M. Ahlers, and B. C. Lacki, "Testing the Hadronuclear Origin of PeV Neutrinos Observed with IceCube," *Phys. Rev.*, vol. D88, no. 12, p. 121301, 2013.

[37] M. G. Aartsen *et al.*, "All-sky search for time-integrated neutrino emission from astrophysical sources with 7 years of IceCube data," 2016.

[38] J. Braun, J. Dumm, F. De Palma, C. Finley, A. Karle, and T. Montaruli, "Methods for point source analysis in high energy neutrino telescopes," *Astropart. Phys.*, vol. 29, pp. 299–305, 2008.

[39] M. G. Aartsen *et al.*, "Search for Time-independent Neutrino Emission from Astrophysical Sources with 3 yr of IceCube Data," *Astrophys. J.*, vol. 779, p. 132, 2013.

[40] A. Achterberg *et al.*, "On the selection of AGN neutrino source candidates for a source stacking analysis with neutrino telescopes," *Astropart. Phys.*, vol. 26, pp. 282–300, 2006.

[41] R. Abbasi *et al.*, "Search for Point Sources of High Energy Neutrinos with Final Data from AMANDA-II," *Phys. Rev.*, vol. D79, p. 062001, 2009.

[42] P. Abreu, M. Aglietta, E. J. Ahn, D. Allard, I. Allekotte, J. Allen, J. Alvarez Castillo, J. Alvarez-Muñiz, M. Ambrosio, A. Aminaei, and et al., "Update on the correlation of the highest energy cosmic rays with nearby extragalactic matter," *Astroparticle Physics*, vol. 34, pp. 314–326, 2010.

[43] R. U. Abbasi *et al.*, "Indications of Intermediate-Scale Anisotropy of Cosmic Rays with Energy Greater Than 57 EeV in the Northern Sky Measured with the Surface Detector of the Telescope Array Experiment," *Astrophys. J.*, vol. 790, p. L21, 2014.

[44] "tevcat.uchicago.edu,"

[45] J. Abraham *et al.*, "Correlation of the highest energy cosmic rays with nearby extragalactic objects," *Science*, vol. 318, pp. 938–943, 2007.

[46] M.-P. Véron-Cetty and P. Véron, "A catalogue of quasars and active nuclei: 13th edition," *Astronomy and Astrophysics*, vol. 518, p. A10, July 2010.

[47] P. L. Biermann and P. A. Strittmatter, "Synchrotron emission from shock waves in active galactic nuclei," *Astrophys. J.*, vol. 322, pp. 643–649, 1987.

[48] G. Giacinti, M. Kachelriess, D. V. Semikoz, and G. Sigl, "Ultrahigh Energy Nuclei in the Turbulent Galactic Magnetic Field," *Astropart. Phys.*, vol. 35, pp. 192–200, 2011.

[49] P. L. Biermann and V. de Souza, "Centaurus A: the one extragalactic source of cosmic rays with energies above the knee," *Astrophys. J.*, vol. 746, p. 72, 2012.

[50] F. Aharonian *et al.*, "Discovery of very high energy gamma-ray emission from Centaurus A with H.E.S.S," *Astrophys. J.*, vol. 695, pp. L40–L44, 2009.

[51] F. M. Rieger and F. A. Aharonian, "Cen A as TeV gamma-ray and possible UHE cosmic-ray source," *Astron. Astrophys.*, vol. 506, p. L41, 2009.

[52] F. M. Rieger, "Cen A as gamma- and UHE cosmic-ray Source," *Mem. Soc. Ast. It.*, vol. 83, p. 127, 2012.

[53] I. Saba, J. Becker Tjus, and F. Halzen, "Limits on the source properties of FR-I galaxies from high-energy neutrino and gamma observations," *Astropart. Phys.*, vol. 48, pp. 30–36, 2013.

[54] F. W. Stecker, C. Done, M. H. Salamon, and P. Sommers, "High-energy neutrinos from active galactic nuclei," *Phys. Rev. Lett.*, vol. 66, pp. 2697–2700, 1991. [Erratum: Phys. Rev. Lett.69,2738(1992)].

[55] L. Nellen, K. Mannheim, and P. L. Biermann, "Neutrino production through hadronic cascades in AGN accretion disks," *Phys. Rev.*, vol. D47, pp. 5270–5274, 1993.

[56] J. K. Becker, P. L. Biermann, and W. Rhode, "The Diffuse neutrino flux from FR-II radio galaxies and blazars: A Source property based estimate," *Astropart. Phys.*, vol. 23, pp. 355–368, 2005.

[57] J. K. Becker and P. L. Biermann, "Neutrinos from active black holes, sources of ultra high energy cosmic rays," *Astropart. Phys.*, vol. 31, pp. 138–148, 2009.

[58] B. Eichmann, R. Schlickeiser, and W. Rhode, "Differences of leptonic and hadronic radiation production in flaring blazars," *Astrophys. J.*, vol. 749, p. 155, 2012.

[59] K. Mannheim and R. Schlickeiser, "Interactions of Cosmic Ray Nuclei," *Astron. Astrophys.*, vol. 286, pp. 983–996, 1994.

[60] C. D. Dermer, "Secondary production of neutral pi-mesons and the diffuse galactic gamma radiation," *Astronomy and Astrophysics*, vol. 157, pp. 223–229, Mar. 1986.

[61] C. J. Willott, S. Rawlings, K. M. Blundell, M. Lacy, and S. A. Eales, "The radio luminosity function from the low-frequency 3crr, 6ce & 7crs complete samples," *Mon. Not. Roy. Astron. Soc.*, vol. 322, pp. 536–552, 2001.

[62] E. Waxman and J. N. Bahcall, "High-energy neutrinos from astrophysical sources: An Upper bound," *Phys. Rev.*, vol. D59, p. 023002, 1999.

[63] R. schlickeiser, "Cosmic Ray Astrophysics," *Springer*, 2002.

[64] A. Crusius and R. Schlickeiser, "Synchrotron radiation in random magnetic fields," *Astronomy and Astrophysics*, vol. 164, pp. L16–L18, Aug. 1986.

[65] J. K. Becker, P. L. Biermann, J. Dreyer, and T. M. Kneiske, "Cosmic Rays VI - Starburst galaxies at multiwavelengths," 2009.

[66] S. P. O'Sullivan and D. C. Gabuzda, "Magnetic field strength and spectral distribution of six parsec-scale active galactic nuclei jets," *Mon. Not. Roy. Astron. Soc.*, vol. 400, p. 26, 2009.

[67] J. Kataoka and L. Stawarz, "X-ray emission properties of large scale jets, hotspots and lobes in active galactic nuclei," *Astrophys. J.*, vol. 622, p. 797, 2005.

[68] L. Wan and R. A. Daly, "A Detailed Investigation of Radio Power Selection Effects Relevant to the Study of Classical Double Radio Sources," *Astrophys. J.*, vol. 115, pp. 141–162, 1998.

[69] W. Winter, "Photohadronic Origin of the TeV-PeV Neutrinos Observed in IceCube," *Phys. Rev.*, vol. D88, p. 083007, 2013.

[70] J. K. Becker, W. Rhode, P. L. Biermann, and K. Muenich, "Astrophysical implications of high energy neutrino limits. 1. Overall diffuse limits," *Astropart. Phys.*, vol. 28, pp. 98–118, 2008.

[71] N. Fraija, M. M. Gonzalez, and M. Perez, "Hadronic processes as origin of TeV emission in Fanaroff-Riley Class I: Cen A, M87 and NGC1275," *PoS*, vol. GRB2012, p. 131, 2012.

[72] A. Loeb and E. Waxman, "The Cumulative background of high energy neutrinos from starburst galaxies," *JCAP*, vol. 0605, p. 003, 2006.

[73] K. Murase, Y. Inoue, and C. D. Dermer, "Diffuse Neutrino Intensity from the Inner Jets of Active Galactic Nuclei: Impacts of External Photon Fields and the Blazar Sequence," *Phys. Rev.*, vol. D90, no. 2, p. 023007, 2014.

[74] D. Hooper, "A Case for Radio Galaxies as the Sources of IceCube's Astrophysical Neutrino Flux," *JCAP*, vol. 1609, no. 09, p. 002, 2016.

[75] X. Wang and A. Loeb, "Cumulative neutrino background from quasar-driven outflows," 2016.

[76] M. Ackermann *et al.*, "Resolving the Extragalactic $\gamma$-Ray Background above 50 GeV with the Fermi Large Area Telescope," *Phys. Rev. Lett.*, vol. 116, no. 15, p. 151105, 2016.

[77] M. Ahlers, "High-Energy Neutrinos in Light of Fermi-LAT," in *5th International Fermi Symposium Nagoya, Japan, October 20-24, 2014*, 2015.

[78] P. Padovani, E. Resconi, P. Giommi, B. Arsioli, and Y. L. Chang, "Extreme blazars as counterparts of IceCube astrophysical neutrinos," *Mon. Not. Roy. Astron. Soc.*, vol. 457, p. 3582, 2016.

[79] M. Kadler *et al.*, "Coincidence of a high-fluence blazar outburst with a PeV-energy neutrino event," 2016.

[80] M. G. Aartsen *et al.*, "Searches for Time Dependent Neutrino Sources with IceCube Data from 2008 to 2012," *Astrophys. J.*, vol. 807, no. 1, p. 46, 2015.

[81] A. Mastichiadis and J. G. Kirk, "Variability in the synchrotron self-compton model of blazar emission," *Astron. Astrophys.*, vol. 320, p. 19, 1997.

[82] K. Mannheim, "The Proton blazar," *Astron. Astrophys.*, vol. 269, p. 67, 1993.

[83] M. Ahlers and F. Halzen, "Pinpointing Extragalactic Neutrino Sources in Light of Recent IceCube Observations," *Phys. Rev.*, vol. D90, no. 4, p. 043005, 2014.

[84] M. Ackermann, E. Bernardini, E. Resconi, and T. Hauschildt, "Multiwavelength comparison of selected neutrino point source candidates," in *29th International Cosmic Ray Conference (ICRC 2005) Pune, India, August 3-11, 2005*, 2005.

[85] S. Cutini, "Fermi LAT detection of renewed and strong GeV activity from blazar 3C 279," *The Astronomer's Telegram*, vol. 7633, June 2015.

[86] M. Ackermann *et al.*, "Minute-Timescale >100 MeV gamma-ray variability during the giant outburst of quasar 3C 279 observed by Fermi-LAT in 2015 June," 2016.

[87] C. Pittori, F. Verrecchia, S. Puccetti, I. Donnarumma, and M. Tavani, "Swift first follow-up observation of the GeV flaring blazar 3C 279," *The Astronomer's Telegram*, vol. 7639, June 2015.

[88] F. Halzen and D. Hooper, "High energy neutrinos from the TeV blazar 1ES 1959+650," *Astropart. Phys.*, vol. 23, pp. 537–542, 2005.

[89] R. C. Hartman, D. L. Bertsch, C. E. Fichtel, S. D. Hunter, G. Kanbach, D. A. Kniffen, P. W. Kwok, Y. C. Lin, J. R. Mattox, H. A. Mayer-Hasselwander, P. F. Michelson, C. von Montigny, H. I. Nel, P. L. Nolan, K. Pinkau, H. Rothermel, E. Schneid, M. Sommer, P. Sreekumar, and D. J. Thompson, "Detection of high-energy gamma radiation from quasar 3C 279 by the EGRET telescope on the Compton Gamma Ray Observatory," *Astrophys. J. Lett.*, vol. 385, pp. L1–L4, Jan. 1992.

[90] M. Errando *et al.*, "Discovery of very high energy gamma-rays from the flat spectrum radio quasar 3C 279 with the MAGIC telescope," *AIP Conf. Proc.*, vol. 1085, pp. 423–426, 2009.

[91] M. Aartsen *et al.*, "Searches for Extended and Point-like Neutrino Sources with Four Years of IceCube Data ," 2014.

[92] V. S. Paliya, C. Diltz, M. Bottcher, C. S. Stalin, and D. Buckley, "A hard gamma-ray flare from 3C 279 in 2013 December," *Astrophys. J.*, vol. 817, no. 1, p. 61, 2016.

[93] M. Hayashida *et al.*, "Rapid Variability of Blazar 3C 279 during Flaring States in 2013-2014 with Joint Fermi-LAT, NuSTAR, Swift, and Ground-Based Multi-wavelength Observations," *Astrophys. J.*, vol. 807, no. 1, p. 79, 2015.

[94] R. Mukherjee, "VERITAS observation of a bright very-high-energy gamma-ray flare from 1ES 1959+650," *The Astronomer's Telegram*, vol. 8148, Oct. 2015.

[95] A. M. Taylor, S. Gabici, and F. Aharonian, "Galactic halo origin of the neutrinos detected by IceCube," *Phys.Rev.*, vol. D89, no. 10, p. 103003, 2014.

[96] D. Gaggero, D. Grasso, A. Marinelli, A. Urbano, and M. Valli, "The gamma-ray and neutrino sky: A consistent picture of Fermi-LAT, Milagro, and IceCube results," *Astrophys. J.*, vol. 815, no. 2, p. L25, 2015.

[97] M. Ahlers, Y. Bai, V. Barger, and R. Lu, "Galactic neutrinos in the TeV to PeV range," *Phys. Rev.*, vol. D93, no. 1, p. 013009, 2016.

[98] A. Palladino and F. Vissani, "Extragalactic plus Galactic model for IceCube neutrino events," *Astrophys. J.*, vol. 826, no. 2, p. 185, 2016.

[99] D. Fox, K. Kashiyama, and P. MÃl'szarÃşs, "Sub-PeV Neutrinos from TeV Unidentified Sources in the Galaxy," *Astrophys.J.*, vol. 774, p. 74, 2013.

[100] C. Lunardini and S. Razzaque, "High Energy Neutrinos from the Fermi Bubbles," *Phys.Rev.Lett.*, vol. 108, p. 221102, 2012.

[101] C. Lunardini, S. Razzaque, K. T. Theodoseau, and L. Yang, "Neutrino Events at IceCube and the Fermi Bubbles," *Phys.Rev.*, vol. D90, no. 2, p. 023016, 2014.

[102] Y. Bai, A. J. Barger, V. Barger, R. Lu, A. D. Peterson, and J. Salvado, "Neutrino Lighthouse at Sagittarius A*," *Phys. Rev.*, vol. D90, no. 6, p. 063012, 2014.

[103] S. Adrian-Martinez *et al.*, "Searches for Point-like and extended neutrino sources close to the Galactic Centre using the ANTARES neutrino Telescope," *Astrophys.J.*, vol. 786, p. L5, 2014.

[104] M. Gonzalez-Garcia, F. Halzen, and V. Niro, "Reevaluation of the Prospect of Observing Neutrinos from Galactic Sources in the Light of Recent Results in Gamma Ray and Neutrino Astronomy," *Astropart.Phys.*, vol. 57-58, pp. 39–48, 2014.

[105] F. Halzen, A. Kappes, and A. O'Murchadha, "Prospects for identifying the sources of the Galactic cosmic rays with IceCube," *Phys.Rev.*, vol. D78, p. 063004, 2008.

[106] M. Gonzalez-Garcia, F. Halzen, and S. Mohapatra, "Identifying Galactic PeVatrons with Neutrinos," *Astropart.Phys.*, vol. 31, pp. 437–444, 2009.

[107] A. Abdo, U. Abeysekara, B. Allen, T. Aune, D. Berley, *et al.*, "Spectrum and Morphology of the Two Brightest Milagro Sources in the Cygnus Region: MGRO J2019+37 and MGRO J2031+41," *Astrophys.J.*, vol. 753, p. 159, 2012.

[108] A. J. Smith, "A Survey of Fermi Catalog Sources using Data from the Milagro Gamma-Ray Observatory ," 2010.

[109] A. U. Abeysekara *et al.*, "Search for TeV Gamma-Ray Emission from Point-like Sources in the Inner Galactic Plane with a Partial Configuration of the HAWC Observatory," *Astrophys. J.*, vol. 817, no. 1, p. 3, 2016.

[110] A. Sandoval, "Highlights from hawc, 6th international symposium on high-energy gamma-ray astronomy (gamma2016), heidelberg, germany, july 11-15," 2016.

[111] H. Collaboration, "HAWC Observatory second catalog of gamma rays," *to be published.*

[112] M. Lemoine, K. Kotera, and J. Pétri, "On ultra-high energy cosmic ray acceleration at the termination shock of young pulsar winds," *JCAP*, vol. 1507, p. 016, 2015.

[113] A. Abdo, B. T. Allen, D. Berley, S. Casanova, C. Chen, *et al.*, "TeV Gamma-Ray Sources from a Survey of the Galactic Plane with Milagro," *Astrophys.J.*, vol. 664, pp. L91–L94, 2007.

[114] A. Abdo, B. Allen, T. Aune, D. Berley, C. Chen, *et al.*, "Milagro Observations of TeV Emission from Galactic Sources in the Fermi Bright Source List," *Astrophys.J.*, vol. 700, pp. L127–L131, 2009.

[115] "Observation of the TeV gamma-ray source MGRO J1908+06 with ARGO-YBJ," *Astrophys.J.*, vol. 760, p. 110, 2012.

[116] F. Aharonian, "Detection of Very High Energy radiation from HESS J1908+063 confirms the Milagro unidentified source MGRO J1908+06," *Astron.Astrophys.*, vol. 499, p. 723, 2009.

[117] E. Aliu, S. Archambault, T. Aune, B. Behera, M. Beilicke, *et al.*, "Investigating the TeV Morphology of MGRO J1908+06 with VERITAS," *Astrophys.J.*, vol. 787, p. 166, 2014.

[118] A. Abdo and A. Abdo, "PSR J1907+0602: A Radio-Faint Gamma-Ray Pulsar Powering a Bright TeV Pulsar Wind Nebula," *Astrophys.J.*, vol. 711, pp. 64–74, 2010.

[119] W. Baade and F. Zwicky, "On super-novae," *Proceedings of the National Academy of Sciences*, vol. 20, no. 5, pp. 254–259, 1934.

[120] M. Ackermann *et al.*, "Detection of the Characteristic Pion-Decay Signature in Supernova Remnants," *Science*, vol. 339, p. 807, 2013.

[121] S. Gabici and F. A. Aharonian, "Searching for galactic cosmic ray pevatrons with multi-TeV gamma rays and neutrinos," *Astrophys.J.*, vol. 665, p. L131, 2007.

[122] A. A. Abdo, *Discovery of localized TeV gamma-ray sources and diffuse TeV gamma-ray emission from the Galactic Plane with Milagro using a new background rejection technique.* PhD thesis, Michigan State University, Department of Physics and Astronomy, 2007.

[123] B. Bartoli, P. Bernardini, X. Bi, C. Bleve, I. Bolognino, *et al.*, "Observation of TeV gamma rays from the Cygnus region with the ARGO-YBJ experiment," *Astrophys.J.*, vol. 745, p. L22, 2012.

[124] J. Albert *et al.*, "MAGIC observations of the unidentified TeV gamma-ray source TeV J2032+4130," *Astrophys.J.*, vol. 675, pp. L25–L28, 2008.

[125] F. Aharonian *et al.*, "The Unidentified TeV source (TeV J2032+4130) and surrounding field: Final HEGRA IACT-system results," *Astron.Astrophys.*, vol. 431, pp. 197–202, 2005.

[126] M. J. Lang, D. Carter-Lewis, D. Fegan, S. Fegan, A. Hillas, *et al.*, "Evidence for TeV gamma ray emission from TeV j2032+4130 in whipple archival data," *Astron.Astrophys.*, vol. 423, pp. 415–419, 2004.

[127] A. Weinstein, "Pulsar Wind Nebulae and Cosmic Rays: A Bedtime Story," *Nucl.Phys.Proc.Suppl.*, vol. 256-257, pp. 136–148, 2014.

[128] B. Bartoli *et al.*, "Identification of the TeV Gamma-ray Source ARGO J2031+4157 with the Cygnus Cocoon," *Astrophys. J.*, vol. 790, no. 2, p. 152, 2014.

[129] J. F. Beacom and M. D. Kistler, "Dissecting the Cygnus Region with TeV Gamma Rays and Neutrinos," *Phys.Rev.*, vol. D75, p. 083001, 2007.

[130] E. Aliu, T. Aune, B. Behera, M. Beilicke, W. Benbow, *et al.*, "Spatially resolving the very high energy emission from MGRO J2019+37 with VERITAS," *Astrophys.J.*, vol. 788, p. 78, 2014.

[131] S. Kelner, F. A. Aharonian, and V. Bugayov, "Energy spectra of gamma-rays, electrons and neutrinos produced at proton-proton interactions in the very high energy regime," *Phys.Rev.*, vol. D74, p. 034018, 2006.

[132] A. Kappes, J. Hinton, C. Stegmann, and F. A. Aharonian, "Potential Neutrino Signals from Galactic Gamma-Ray Sources," *Astrophys.J.*, vol. 656, pp. 870–896, 2007.

[133] A. Kappes, F. Halzen, and A. O. Murchadha, "Prospects of identifying the sources of the galactic cosmic rays with IceCube," *Nucl.Instrum.Meth.*, vol. A602, pp. 117–119, 2009.

[134] F. Halzen and A. O Murchadha, "Neutrinos from Cosmic Ray Accelerators in the Cygnus Region of the Galaxy," *Phys.Rev.*, vol. D76, p. 123003, 2007.

[135] F. Vissani and F. Aharonian, "Galactic Sources of High-Energy Neutrinos: Highlights," *Nucl.Instrum.Meth.*, vol. A692, pp. 5–12, 2012.

[136] F. Vissani, F. Aharonian, and N. Sahakyan, "On the Detectability of High-Energy Galactic Neutrino Sources," *Astropart.Phys.*, vol. 34, pp. 778–783, 2011.

[137] C. Tchernin, J. Aguilar, A. Neronov, and T. Montaruli, "Neutrino signal from extended Galactic sources in IceCube," *Astron.Astrophys.*, vol. 560, p. A67, 2013.

[138] M. Honda, T. Kajita, K. Kasahara, and S. Midorikawa, "Improvement of low energy atmospheric neutrino flux calculation using the JAM nuclear interaction model," *Phys.Rev.*, vol. D83, p. 123001, 2011.

[139] D. Alexandreas, D. Berley, S. Biller, G. Dion, J. Goodman, *et al.*, "Point source search techniques in ultrahigh-energy gamma-ray astronomy," *Nucl.Instrum.Meth.*, vol. A328, pp. 570–577, 1993.

[140] "Procedure for the LHC Higgs boson search combination in summer 2011," 2011.

[141] T. Junk, "Confidence level computation for combining searches with small statistics," *Nucl.Instrum.Meth.*, vol. A434, pp. 435–443, 1999.

[142] A. L. Read, "Modified frequentist analysis of search results (The CL(s) method)," 2000.

[143] J. Beringer *et al.*, "Review of Particle Physics (RPP)," *Phys.Rev.*, vol. D86, p. 010001, 2012.

[144] D. R. Lorimer *et al.*, "A bright millisecond radio burst of extragalactic origin," *Science*, vol. 318, no. 5851, pp. 777–780, 2007.

[145] L. G. Spitler *et al.*, "A repeating fast radio burst," *Nature*, vol. 531, pp. 202–205, 03 2016.

[146] P. Scholz, L. G. Spitler, J. W. T. Hessels, S. Chatterjee, J. M. Cordes, V. M. Kaspi, R. S. Wharton, C. G. Bassa, S. Bogdanov, F. Camilo, F. Crawford, J. Deneva, J. van Leeuwen, R. Lynch, E. C. Madsen, M. A. McLaughlin, M. Mickaliger, E. Parent, C. Patel, S. M. Ransom, A. Seymour, I. H. Stairs, B. W. Stappers, and S. P. Tendulkar, "The repeating Fast Radio Burst FRB 121102: Multi-wavelength observations and additional bursts," *ArXiv e-prints*, Mar. 2016.

[147] D. J. Champion *et al.*, "Five new fast radio bursts from the HTRU high-latitude survey at Parkes: first evidence for two-component bursts," *Monthly Notices of the Royal Astronomical Society: Letters*, vol. 460, no. 1, pp. L30–L34, 2016.

[148] Falcke, H. and Rezzolla, L., "Fast radio bursts: the last sign of supramassive neutron stars," *Astronomy and Astrophysics*, vol. 562, p. A137, 2014.

[149] U.-L. Pen and L. Connor, "Local circumnuclear magnetar solution to extragalactic fast radio bursts," *The Astrophysical Journal*, vol. 807, no. 2, p. 179, 2015.

[150] A. Loeb, Y. Shvartzvald, and D. Maoz, "Fast radio bursts may originate from nearby flaring stars," *MNRAS*, vol. 439, pp. L46–L50, Mar. 2014.

[151] X. Li *et al.*, "Model-dependent estimate on the connection between fast radio bursts and ultra high energy cosmic rays," *The Astrophysical Journal*, vol. 797, no. 1, p. 33, 2014.

[152] E. F. Keane *et al.*, "The host galaxy of a fast radio burst," *Nature*, vol. 530, pp. 453–456, 02 2016.

[153] P. K. G. Williams and E. Berger, "No precise localization for FRB 150418: Claimed radio transient is AGN variability," *The Astrophysical Journal Letters*, vol. 821, no. 2, p. L22, 2016.

[154] IceCube Collaboration, "Search for point sources with the first year of IC86 data. IceCube Neutrino Observatory. Dataset," 2016.

[155] S. Tilav *et al.*, "Atmospheric variations as observed by IceCube," Jan. 2010.

[156] K. Masui *et al.*, "Dense magnetized plasma associated with a fast radio burst," *Nature*, vol. 528, pp. 523–525, 12 2015.

[157] D. Thornton *et al.*, "A population of fast radio bursts at cosmological distances," *Science*, vol. 341, no. 6141, pp. 53–56, 2013.

[158] R. Abbasi *et al.*, "An absence of neutrinos associated with cosmic-ray acceleration in gamma-ray bursts," *Nature*, vol. 484, pp. 351–354, Apr. 2012.

[159] M. G. Aartsen *et al.*, "Search for prompt neutrino emission from gamma-ray bursts with IceCube," *The Astrophysical Journal Letters*, vol. 805, no. 1, p. L5, 2015.

[160] R. Abbasi *et al.*, "IceCube Sensitivity for Low-Energy Neutrinos from Nearby Supernovae," *Astron. Astrophys.*, vol. 535, p. A109, 2011. [Erratum: Astron. Astrophys.563,C1(2014)].

[161] G. Jungman, M. Kamionkowski, and K. Griest, "Supersymmetric dark matter," *Phys. Rept.*, vol. 267, pp. 195–373, 1996.

[162] R. Adhikari *et al.*, "A White Paper on keV Sterile Neutrino Dark Matter," *Submitted to: White paper*, 2016.

[163] C. Boehm, P. Fayet, and R. Schaeffer, "Constraining dark matter candidates from structure formation," *Phys.Lett.*, vol. B518, pp. 8–14, 2001.

[164] C. Boehm, A. Riazuelo, S. H. Hansen, and R. Schaeffer, "Interacting dark matter disguised as warm dark matter," *Phys.Rev.*, vol. D66, p. 083505, 2002.

[165] C. Boehm and R. Schaeffer, "Constraints on dark matter interactions from structure formation: Damping lengths," *Astron.Astrophys.*, vol. 438, pp. 419–442, 2005.

[166] E. Bertschinger, "The Effects of Cold Dark Matter Decoupling and Pair Annihilation on Cosmological Perturbations," *Phys.Rev.*, vol. D74, p. 063509, 2006.

[167] G. Mangano, A. Melchiorri, P. Serra, A. Cooray, and M. Kamionkowski, "Cosmological bounds on dark matter-neutrino interactions," *Phys.Rev.*, vol. D74, p. 043517, 2006.

[168] P. Serra, F. Zalamea, A. Cooray, G. Mangano, and A. Melchiorri, "Constraints on neutrino – dark matter interactions from cosmic microwave background and large scale structure data," *Phys.Rev.*, vol. D81, p. 043507, 2010.

[169] R. J. Wilkinson, C. Boehm, and J. Lesgourgues, "Constraining Dark Matter-Neutrino Interactions using the CMB and Large-Scale Structure," *JCAP*, vol. 1405, p. 011, 2014.

[170] L. G. van den Aarssen, T. Bringmann, and C. Pfrommer, "Is dark matter with long-range interactions a solution to all small-scale problems of $\Lambda$CDM cosmology?," *Phys.Rev.Lett.*, vol. 109, p. 231301, 2012.

[171] Y. Farzan and S. Palomares-Ruiz, "Dips in the Diffuse Supernova Neutrino Background," *JCAP*, vol. 1406, p. 014, 2014.

[172] C. Boehm, J. Schewtschenko, R. Wilkinson, C. Baugh, and S. Pascoli, "Using the Milky Way satellites to study interactions between cold dark matter and radiation," *Mon.Not.Roy.Astron.Soc.*, vol. 445, pp. L31–L35, 2014.

[173] J. F. Cherry, A. Friedland, and I. M. Shoemaker, "Neutrino Portal Dark Matter: From Dwarf Galaxies to IceCube," 2014.

[174] B. Bertoni, S. Ipek, D. McKeen, and A. E. Nelson, "Constraints and consequences of reducing small scale structure via large dark matter-neutrino interactions," *JHEP*, vol. 1504, p. 170, 2015.

[175] J. Schewtschenko, R. Wilkinson, C. Baugh, C. Boehm, and S. Pascoli, "Dark matter-radiation interactions: the impact on dark matter haloes," *Mon.Not.Roy.Astron.Soc.*, vol. 449, pp. 3587–3596, 2015.

[176] J. H. Davis and J. Silk, "Spectral and Spatial Distortions of PeV Neutrinos from Scattering with Dark Matter," 2015.

[177] Y. Bai, R. Lu, and J. Salvado, "Geometric Compatibility of IceCube TeV-PeV Neutrino Excess and its Galactic Dark Matter Origin," 2013.

[178] C. Boehm and P. Fayet, "Scalar dark matter candidates," *Nucl. Phys.*, vol. B683, pp. 219–263, 2004.

[179] D. G. Cerdeno, C. Munoz, and O. Seto, "Right-handed sneutrino as thermal dark matter," *Phys. Rev.*, vol. D79, p. 023510, 2009.

[180] D. G. Cerdeno and O. Seto, "Right-handed sneutrino dark matter in the NMSSM," *JCAP*, vol. 0908, p. 032, 2009.

[181] C. Boehm, Y. Farzan, T. Hambye, S. Palomares-Ruiz, and S. Pascoli, "Is it possible to explain neutrino masses with scalar dark matter?," *Phys. Rev.*, vol. D77, p. 043516, 2008.

[182] J. Alwall, P. Schuster, and N. Toro, "Simplified Models for a First Characterization of New Physics at the LHC," *Phys. Rev.*, vol. D79, p. 075020, 2009.

[183] D. Alves, "Simplified Models for LHC New Physics Searches," *J. Phys.*, vol. G39, p. 105005, 2012.

[184] A. C. Vincent, S. Palomares-Ruiz, and O. Mena, "Analysis of the 4-year IceCube HESE data," 2016.

[185] C. A. Arguelles, T. Katori, and J. Salvado, "New Physics in Astrophysical Neutrino Flavor," *Phys. Rev. Lett.*, vol. 115, p. 161303, 2015.

[186] D. Foreman-Mackey, D. W. Hogg, D. Lang, and J. Goodman, "emcee: The MCMC Hammer," *Publications of the Astronomical Society of Pacific*, vol. 125, pp. 306–312, Mar. 2013.

[187] P. A. R. Ade *et al.*, "Planck 2013 results. XVI. Cosmological parameters," *Astron. Astrophys.*, vol. 571, p. A16, 2014.

[188] D. Parkinson, S. Riemer-Sørensen, C. Blake, G. B. Poole, T. M. Davis, S. Brough, M. Colless, C. Contreras, W. Couch, S. Croom, D. Croton, M. J. Drinkwater, K. Forster, D. Gilbank, M. Gladders, K. Glazebrook, B. Jelliffe, R. J. Jurek, I.-h. Li, B. Madore, D. C. Martin, K. Pimbblet, M. Pracy, R. Sharp, E. Wisnioski, D. Woods, T. K. Wyder, and H. K. C. Yee, "The WiggleZ Dark Energy Survey: Final data release and cosmological results," *Phys. Rev. D*, vol. 86, p. 103518, Nov. 2012.

[189] M. Escudero, O. Mena, A. C. Vincent, R. J. Wilkinson, and C. Boehm, "Exploring dark matter microphysics with galaxy surveys," *JCAP*, vol. 1509, no. 09, p. 034, 2015.

# APPENDIX

## A.1 Cross sections for simplified model of dark matter-neutrino interactions

DM-neutrino cross sections must be evaluated in the dark matter rest frame. We provide these here. Both the neutrino energy $E_\nu$ and the scattering angle $x \equiv \cos(\theta)$ are therefore lab frame quantities.

1) Scalar dark matter with a scalar mediator.

$$\frac{d\sigma}{d\cos\theta} = \frac{g^2 g'^2 (1-x) E_\nu^2 m_\chi}{16\pi \left((1-x)E_\nu + m_\chi\right)\left((1-x)E_\nu m_\phi^2 + m_\chi \left(m_\phi^2 - 2(x-1)E_\nu^2\right)\right)^2} \tag{A.1}$$

$$\sigma_{lab} = -g^2 g'^2 \frac{4E_\nu^2 m_\chi + (2E_\nu m_\phi^2 + 4E_\nu^2 m_\chi + m_\phi^2 m_\chi)\log\left(\frac{m_\phi^2(2E_\nu + m_\chi)}{2E_\nu m_\phi^2 + 4E_\nu^2 m_\chi + m_\phi^2 m_\chi}\right)}{128\pi E_\nu^2 m_\chi^2 (2E_\nu m_\phi^2 + 4E_\nu^2 m_\chi + m_\phi^2 m_\chi)} \tag{A.2}$$

2) Fermion DM with a scalar mediator

$$\frac{d\sigma}{d\cos\theta} = \frac{g^2 (x-1)\left(g'\right)^2 E_\nu^2 m_\chi^2 \left(2(x-1)E_\nu m_\chi + (x-1)E_\nu^2 - 2m_\chi^2\right)}{8\pi \left(m_\chi - (x-1)E_\nu\right)^2 \left((x-1)E_\nu m_\phi^2 - m_\chi\left(m_\phi^2 - 2(x-1)E_\nu^2\right)\right)^2} \tag{A.3}$$

and

$$\sigma = \frac{g^2\left(g'\right)^2}{32\pi E_\nu^2 m_\chi^2}\left[E_\nu m_\chi - \frac{E_\nu m_\chi^2}{2E_\nu + m_\chi} - \frac{E_\nu m_\chi^2 m_\phi^2 \left(m_\phi^2 - 4m_\chi^2\right)}{\left(2E_\nu m_\chi + m_\phi^2\right)\left(4E_\nu^2 m_\chi + 2E_\nu m_\phi^2 + m_\chi m_\phi^2\right)} + \frac{E_\nu m_\chi \left(m_\phi^2 - 4m_\chi^2\right)}{2E_\nu m_\chi + m_\phi^2}\right. \tag{A.4}$$

$$\left. + \left(m_\phi^2 - 2m_\chi^2\right)\log\left(\frac{m_\phi^2(2E_\nu + m_\chi)}{4E_\nu^2 m_\chi + 2E_\nu m_\phi^2 + m_\chi m_\phi^2}\right)\right]. \tag{A.5}$$

3) Fermion DM, vector mediator

$$\frac{d\sigma}{d\cos\theta} = \frac{g^2\left(g'\right)^2 E_\nu^2 m_\chi^2 \left(2(1-x)E_\nu + (1+x)m_\chi\right)}{4\pi\left((1-x)E_\nu + m_\chi\right)\left((1-x)E_\nu m_\phi^2 + m_\chi\left(m_\phi^2 - 2(x-1)E_\nu^2\right)\right)^2} \tag{A.6}$$

$$\sigma = \frac{g^2 g'^2}{16\pi E_\nu^2 m_\phi^2} \left( m_\phi^2 \log\left( \frac{m_\phi^2 (2E_\nu + m_\chi)}{m_\chi (4E_\nu^2 + m_\chi^2) + 2E_\nu m_\phi^2} \right) + \frac{4 m_\chi E_\nu^2}{m_\chi + \frac{2E_\nu m_\phi^2}{4E_\nu^2 + m_\phi^2}} \right) \tag{A.7}$$

4) Scalar DM with a Fermion mediator:

$$\frac{d\sigma}{d\cos\theta} = \frac{g^4 E_\nu^2 m_\chi ((x-1)m_\phi^6 - 2(x-1)m_\phi^4 m_\chi^2 + 8E_\nu^2((x-1)E_\nu - m_\chi)m_\chi^3 + (x-1)m_\phi^2 m_\chi^4)}{4\pi((x-1)E_\nu - m_\chi)^3((m_\phi^2 - m_\chi^2)^2 - 4E_\nu^2 m_\chi^2)^2} \tag{A.8}$$

$$\sigma = \frac{g^4 E_\nu^2 (m_\phi^6 - 2m_\phi^4 m_\chi^2 + m_\phi^2 m_\chi^4 + 8E_\nu^2 m_\chi^3 (2E_\nu + m_\chi))}{2\pi(2E_\nu + m_\chi)^2((m_\chi^2 - m_\phi^2)^2 - 4E_\nu^2 m_\chi^2)^2} \tag{A.9}$$